Analysis of Hadron-Photon and Di-Hadron Correlations in pp Collisions at $\sqrt{s} = 13\,\text{TeV}$ with ALICE

Master Thesis

Alexander Terbeck

Universität Münster
Institut für Kernphysik
AG Andronic

First Referee: Prof. Dr. Christian Klein-Bösing
Second Referee: Prof. Dr. Anton Andronic

Münster, October 2024

Contents

1 Introduction

The human desire to explore new phenomena in nature remains strong, and particle physics provides unique insights into the smallest constituents of the universe. To investigate these fundamental properties of matter, particle accelerators and detectors have been constructed. The currently largest and most powerful one is the Large Hadron Collider (LHC) at CERN in Switzerland and France. With its 27 km circumference, it can accelerate and collide charged particles, such as protons or lead nuclei, at unprecedented energies. One major success of the LHC was the discovery of the last missing particle of the Standard Model of Particle Physics, the Higgs boson in 2012. Many more important properties of particle physics can be explored with the LHC, one of which is the quark-gluon plasma (QGP). This is a state of matter created under extreme energy density conditions where quarks and gluon, the fundamental components of particles, become unbound and behave as quasi-free particles, no longer confined within hadrons.

To analyze this QGP, heavy-ions collisions are necessary, which are the primary focus of the ALICE detector at the LHC. Currently, collisions with heavy-ions are the only way of generating the required energy densities to create the QGP. Photons are among the many particles that arise from the heavy-ion collision and the formation of the QGP. And while photons can be created at various stages of the interaction, high-energy prompt photons are of special interest. This subset of direct photons is created at the initial state of the collision and transverses the QGP without interaction. This provides a valuable probe into the early stages of the formation of the QGP. In contrast to photons, hadrons, due to their color charge, are affected by the QGP and thus only provide information about the later stages of its development. To measure the QGP, reference data is needed. Therefore, experiments with lighter particles like protons are done to gather data for comparison.

In this thesis, proton-proton collisions are analyzed at a center-of-mass energy of $\sqrt{s} = 13\,\text{TeV}$ measured by ALICE. Software frameworks such as AliPhysics, Pythia8 and GEANT3 are utilized for data processing and simulation. After the selection of the data, further corrections are implemented to ensure data quality. Using the refined dataset, hadron-hadron and hadron-gamma correlations are made as alternatives to traditional jet-finding algorithms. Additionally, the particle yields and full-width at half-maximum (FWHM) of the correlation peaks are studied. Finally, the software framework is employed to analyze the origins of the detected particles.

In Chapter 2, a theoretical background to particle physics is provided, with a focus on the strong interaction and the quark-gluon plasma. Chapter 3 describes the experimental setup, including the particle accelerator, detector, and the software framework used in this work. The data selection process, along with the methods used for particle reconstruction, are explained in Chapter 4. The results of this analysis are then presented in Chapter 5, followed by the conclusion in Chapter 6.

2 Theoretical Background

This chapter gives a short introduction to particle physics. It presents different elementary particles and the four fundamental interaction forces, of which three can be described by the Standard Model (SM).

2.1 The Standard Model

The Standard Model of particle physics is a quantum field theory that describes the fundamental particles (Figure 2.1) and three of the four interaction forces. The particles are divided into two main groups: the fermions (subdivided into 6 leptons and 6 quarks) and bosons. The former can be seen as the building blocks of matter, while the latter mediates the fundamental forces between the fermions.

The fermions, which all have a spin of 1/2, are grouped into three generations. Each generation consists of two leptons and two quarks. In general, with each generation, the masses of the particles increases[1]. However, the masses of the neutrinos are not precisely known, making them a topic of ongoing research. Additionally, each particle has its own *antiparticle* that has the same mass and spin but opposite electric charge.

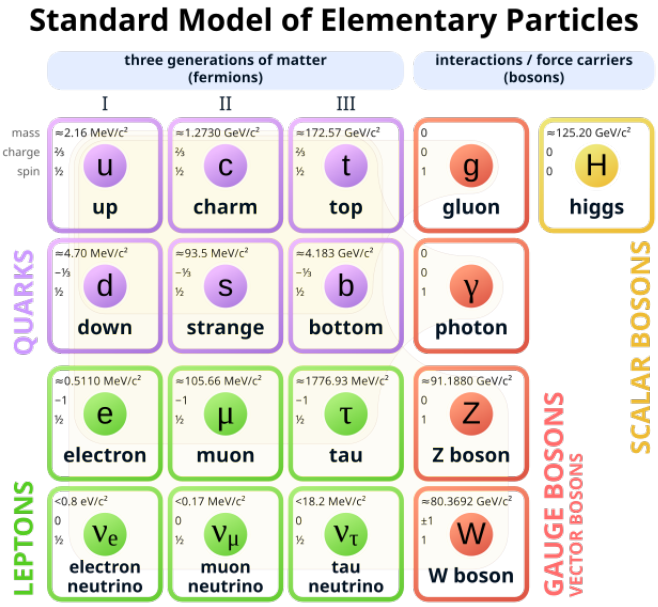

Figure 2.1: The elementary particles of the standard model [1].

[1] It is important to note that all atoms in the periodic table are composed of particles from the first generation.

The quarks can be either counted as up-type quarks, with an electric charge of $Q = +\frac{2}{3}$ and weak isopin $T_3 = +\frac{1}{2}$, or down-type quarks with $Q = -\frac{1}{3}$ and $T_3 = -\frac{1}{3}$. Their masses range from 2.3 MeV/c of the up quark to 174 GeV/c of the top quark.

The leptons can be subdivided into a group with an electric charge of $Q = -1$ with the electron (e^-), muon (μ^-), and tauon (τ^-), and the electrically neutral $Q = 0$ group of the neutrinos. The masses of the former increase with each generation, while the latter are massless in the Standard Model. Despite that, the discovery of neutrino oscillation provided experimental evidence that neutrinos have mass. This cannot be explained with the Standard Model, thus leading to further unknown physics.

The interactions consist of the four fundamental forces: electromagnetism, the weak force, the strong force, and gravity. While the first three are well explained by the Standard Model, gravity is not adequately described by it, and general relativity is used instead. The forces interact through the exchange of gauge bosons with spin 1. Each force has one or more bosons, with each having different particle properties.

For a particle to interact via one of three forces, except gravity, it must possess a specific type of charge related to that force. To interact with the strong force, a particle must have a color charge, which applies only to quarks and gluons (g). Therefore, not only quarks interact with the strong force via the gluons, the gluons themselves also interact with each other. The quantum field theory that describes these phenomena is called *Quantum Choromodynamics (QCD)* and will be discussed in more detail further below.

The electromagnetic force is mediated via an electric charge. The six quarks and three leptons, electron (e^-), muon (μ^-) and tau (τ^-), carry this electric charge and thus are able to interact via this force, through the massless photon (γ). It is important to note that photons themselves are electric neutral, so they do not interact with other photons. The corresponding theory is called *Quantum Electrodynamics (QED)*.

The weak force affects all leptons, meaning that all possess a particle property known as the weak isospin. This force is the only one with the ability to change the flavor[2] of quarks and leptons and is mediated by the W^+-, W^-- and Z-boson. Together with the electromagnetic force, the weak force is described by the electroweak theory, which unifies these two forces into a single electroweak force [2].

2.2 Quantum Chromodynamics

As mentioned earlier, the interaction of quarks and gluons is described by the theory of quantum chromodynamics, which is based on the gauge group SU(3). Quarks and gluons do not appear isolated, instead they only exist in bound states, which is called *confinement*. Quarks combine to form hadrons, which are specific bound states. Hadrons can be further subdivided into baryons and mesons. Baryons consist of three quarks (qqq) or antiquarks ($\bar{q}\bar{q}\bar{q}$), while mesons are made up of a quark-antiquark pair ($q\bar{q}$). This restriction into baryons and mesons can be explained through the *color charge*, or color quantum number. The color

[2]The term flavor is used, instead of type, in particle physics.

charge acts similar to the charge in the electromagnetic force, but it can take three values (red, blue and green) due to the degree of freedom in SU(3). This is in contrast to the electromagnetic force with its two possible values (positive, negative), which arises from the U(1) symmetry. With the three color charges, any bound state of quarks must be invariant under color transformation, which is synonymous with being in a color singlet state (color neutral). In baryons, this can be achieved by mixing a red, a blue and a green quark, or in the case of mesons with a quark-antiquark pair, with their corresponding color and anticolor (e.g., red and antired). Therefore, an anticolor exists for the corresponding antiparticle. Gluons themselves carry a color (in stark contrast to the charge-free photon in the electromagnetic case) and anticolor, which leads to strong self-interactions. With the six possible values of the color charge, group theory can be used to create an octet of ground states, which correspond to eight different possible gluons. These gluons act as the mediator (gauge boson) of the strong force between hadrons and themselves. In Figure 2.2, possible interactions of the gluons can be observed.

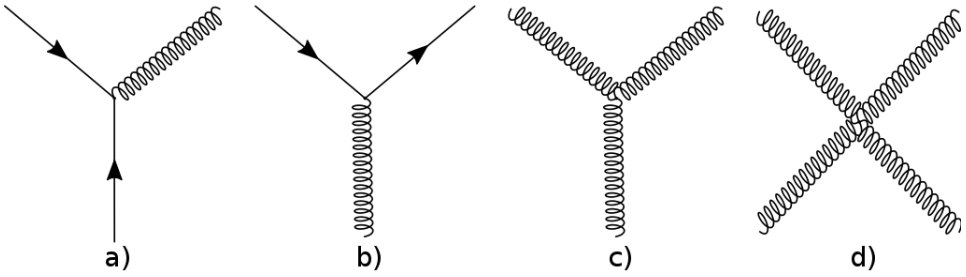

Figure 2.2: Possible couplings of the gluon in the strong interaction: a) emission of a gluon from a quark, b) splitting of a gluon into a quark-antiquark pair, c) and d) self coupling of gluons [3]. Time runs from bottom to top.

Coupling constant The interaction of particles in the strong force is characterized by a running[3] coupling constant $\alpha_s(Q^2)$:

$$\alpha_s(Q^2) = \frac{g_s^2(Q^2)}{4\pi} \tag{2.1}$$

with g_s as the strong coupling parameter [2]. The self-interaction of the gluons is significant for the behavior of the strong coupling constant, in addition to the high dependence of Q. At larger energies (large Q) or equivalently at smaller distances, fluctuation increases the chance of creating additional gluons, which should increase the strong coupling [4]. This is a screening effect, analogous to the screening in the electromagnetic force. But the self-interaction of the gluons leads to an anti-screening, which is larger than the screening, thus reducing the overall strength of the strong force. This is called the *asymptotic freedom* and allows quarks to behave as if they are nearly free particles at very high energies. In contrast, at low values of Q (larger distances between the particles), the coupling constant increases exponentially, making a separation of the quarks impossible, resulting in the aforementioned confinement. The required energy to pull quarks apart increases to the point where new quark-antiquark pairs are created, leading to the formation of new hadrons, called *hadronization*. Figure 2.3 shows results from different experiments that measure the strong coupling constant.

[3] Due to its dependence on the transferred momentum Q

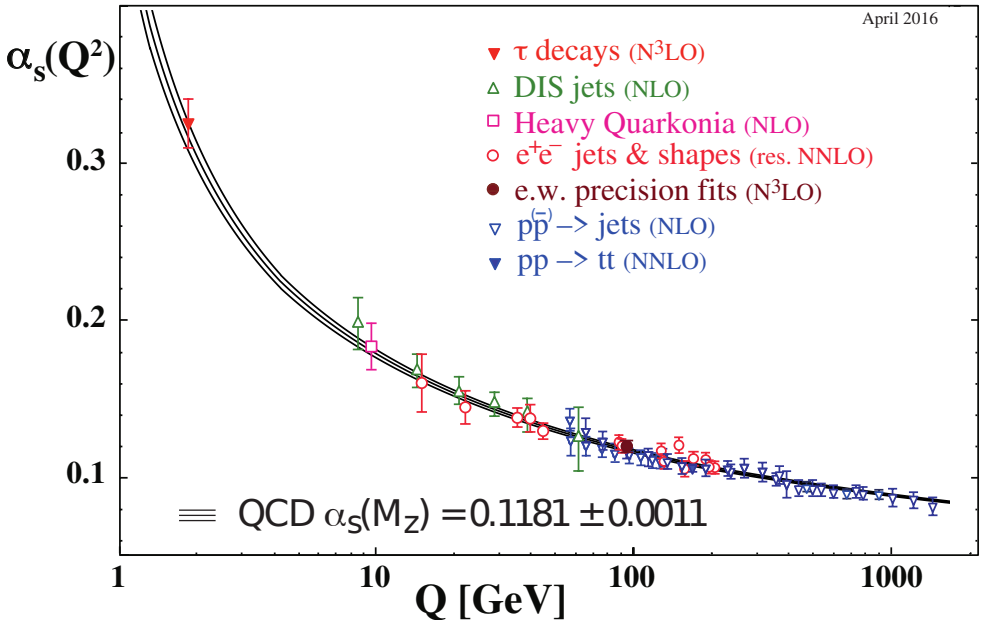

Figure 2.3: Measurements of the strong coupling constant α_s as a function of the energy scale Q [5].

Calculating α_s for the full range leads to unsolvable problems at small Q. While at high energy regions (large Q), perturbation theory (*pQCD*) can be used, but it fails at the low energy region, due to effects like confinement and the strong self-interaction of the gluons. Therefore, a numerical approach called *lattice QCD* can be used, in which space-time is discretized into a finite lattice [6].

In first-order perturbation theory, the dependence of the running constant $\alpha_s(Q^2)$ for large transferred momentum can be written as:

$$\alpha_s(Q^2) \approx \frac{12\pi}{(33 - 2 \cdot N_f) \cdot \ln \frac{Q^2}{\Lambda^2}}, \tag{2.2}$$

with N_f as the number of available quark flavors and the QCD scaling parameter Λ, which is experimentally found to be $\approx 200\,\text{MeV}$. This calculation is only valid for $Q^2 \gg \Lambda$. The Cornell potential describes the interaction between quarks and can be written as:

$$V_s = -\frac{4}{3}\frac{\alpha_s}{r} + \sigma r + \text{const.}, \tag{2.3}$$

with r as the distance between the two particles and σ as the string tension. The first term, proportional to $1/r$, dominates at short distances, and behaves similarly to the Coulomb potential. This term is responsible for the interactions of quarks and gluons, where the strong force is weaker due to asymptotic freedom. At larger distances, the linear term σr becomes more significant. This term is interpreted as the energy in the "strings" that connect the quarks. If quarks move apart, the energy increases linearly until sufficient energy exists for the creation of new quark-antiquark pairs. This will lead to the aforementioned hadronization [7].

Jets In high-energy collisions, collimated one-directional showers of hadrons, known as jets, can occur. In particle collisions, (e.g., proton-proton collisions), the energy exchange of the particles happens at the level of the partons[4]. These color-charged partons scatter in various directions and move further apart from each other. Due to confinement, new quark-antiquark pairs are produced, called *fragmentation*. These new pairs will form new particles, the aforementioned hadronization. The color-neutral hadrons can exist freely and thus be measured in high-energy experiments. Jets are often produced back-to-back, but three-jet events can also occur. By detecting and correctly associating jets, correlation measurements become possible.

2.3 Quark-Gluon Plasma

The asymptotic freedom leads to a weakening of the confinement at high energies. At a sufficiently high range, hadronic matter may dissolve into its constituents of quarks and gluons. These quasi-free quarks and gluons are in a state of deconfined matter, the *Quark-Gluon Plasma* (QGP). The transition from confined to deconfined matter depends on the temperature and baryon chemical potential, as shown in the phase diagram in Figure 2.4. It is highly likely that the Quark-Gluon Plasma exits shortly after the Big Bang, and it is assumed that the core of neutron stars also consists of it. These stars are the only known objects with sufficient density and temperature to create a QGP naturally. Other than that, it is possible to create the QGP for a very short time ($\approx 10^{-23}$ seconds [8]) with heavy-ion collisions, like Lead-Lead (Pb-Pb) in particle colliders.

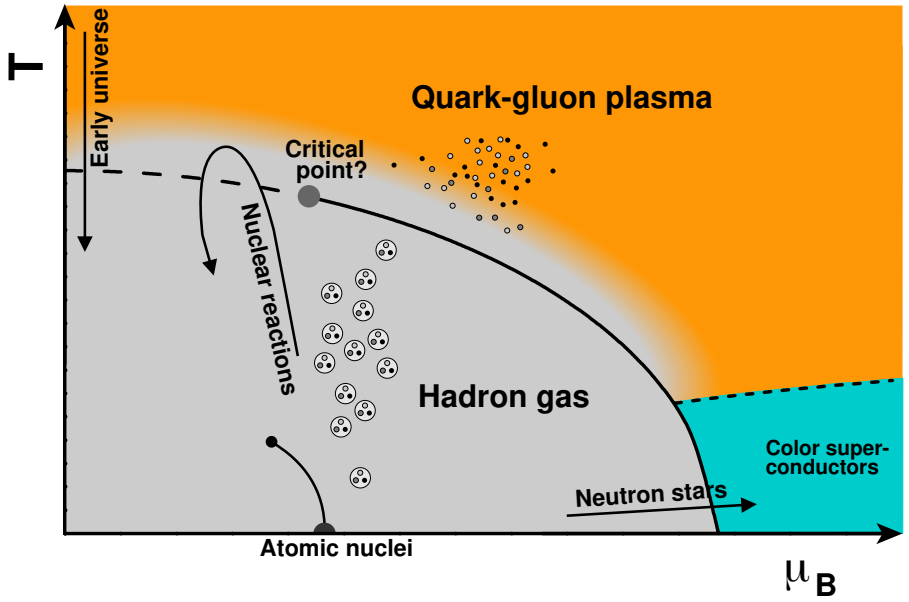

Figure 2.4: Phase diagram of QCD depending on temperature and baryon density. The line indicates the transition of confined (hadron gas) to unconfined matter [9].

Multiple characteristics of the QGP can be derived from the phase diagram in Figure 2.4. First, at low temperature and low baryon density, the normal hadron gas exists. If the

[4]Quarks and/or gluons can collectively be referred to as "partons".

temperature is increased, the matter starts to dissolve into the deconfined QGP. This step is recreated at the LHC. At this low baryon density of $\mu = 0$, lattice QCD predicts a critical transition temperature of $T_C = (154 \pm 9)\,\mathrm{MeV}$[5] [10]. With lower temperatures but higher baryon density, the Quark-Gluon Plasma resembles the matter inside neutron stars [11].

Heavy-ion collisions are essential for studying the Quark-Gluon Plasma, because they produce a high multiplicity of particles. This leads to a high rate of interactions, which significantly eases reaching thermal equilibrium. The QGP expands as a fireball, which can be described with hydrodynamics, and therefore has a behavior similar to that of a liquid. The evolution of the QGP in heavy-ion collision, shown in Figure 2.5, can generally be divided into two phases based on its short lifetime in particle experiments.

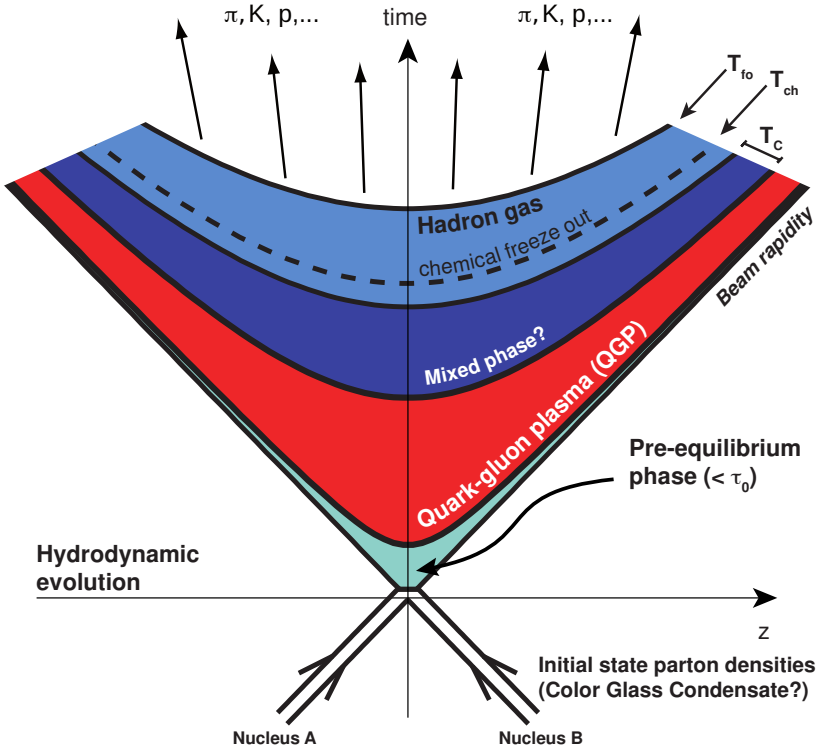

Figure 2.5: Evolution of QGP in heavy-ion collisions in the space-time plane [9].

The first phase is the initial particle collision, in which the Lorentz contracted heavy-ions collide and hard scattering occurs. Parton jets and photons will emerge out of these collisions, and the regions where the two ions overlap will heat up.

In this pre-equilibrium phase, soft scattering starts to be dominant. With the reaching of the critical temperature T_C, the second stage begins with the establishment of the Quark-Gluon plasma. Here, the usage of hydrodynamics is necessary. The quarks and gluons begin to deconfine, but due to the large temperatures, the pressure increases and therefore the medium expands and cools rapidly. This leads to a reconfinement of the partons and the formation of a gas of hadrons due to hadronization. The medium continues to cool out until the *chemical freeze-out* at $T_{CF} = 156.5 \pm 1.5$ [10] at which hadronization stops and the remaining particles do not undergo further decay. Finally, at an even cooler temperature, the

[5] Which is about 2 billion degree Celsius.

kinematic freeze-out is reached, at which the particles stop interacting with each other. This hadron configuration can then be observed in particle detectors.

To measure the properties of the Quark-Gluon plasma, a phenomenon called *jet quenching* can be studied [12]. The parton jets, which emerge before the existence of the QGP at the initial collision, will travel through the QGP and experience a significant energy loss. This energy loss only occurs in heavy-ion collisions like Pb-Pb. Data from p-Pb and pp collisions are taken as a comparison and do not show any similar energy loss. This effect is calculated with the *nuclear modification factor*. The idea behind this is that the spectra from heavy-ion collisions could be understood as a superposition of multiple proton-proton collisions. A pp spectrum with a scaling factor can now be used to compare the two spectra:

$$R_{AA} = \frac{N_{AA}^{\text{particles}}}{\langle T_{AA} \rangle N_{pp}^{\text{particles}}}, \tag{2.4}$$

with $\langle T_{AA} \rangle$ as the average number of collisions per AA collision, $N_{AA}^{\text{particles}}$ and $N_{pp}^{\text{particles}}$ as the particle spectra of AA and pp, respectively. If there is a suppression of energy and particle production within the QGP, R_{AA} will deviate from unity. As can be seen from the formula, pp spectra are needed as a reference to analyze the behavior of Pb-Pb spectra. In contrast to that, photons, which can be produced at the initial collisions, are not affected by any energy loss. In fact, all electromagnetic and weak gauge bosons do not show any significant deviation in the QGP from what is expected. This provides a useful tool to study the initial conditions and properties of the Quark-Gluon plasma. Photons can be significantly easier detected than weak gauge bosons due to their infinite lifetime, which makes them the prime candidate for studying the early phases of the Quark-Gluon plasma [13].

2.4 Particle and Photon Production

The production of photons can have a wide range of possible origins, as seen in sketch Figure 2.6. In general, the photons are divided into two categories, the *direct* and *decay* photons. Decay photons are all photons, that originate from particle decay, with the neutral pion decay as the most prominent example, $\pi_0 \to 2\gamma$. Direct photons are all non-decay photons and are also divided into multiple subgroups based on their production mechanisms. These usually include the *prompt* photons, the *fragmentation* photons, which form from hard processes, and the *thermal* photons, which form from soft processes.

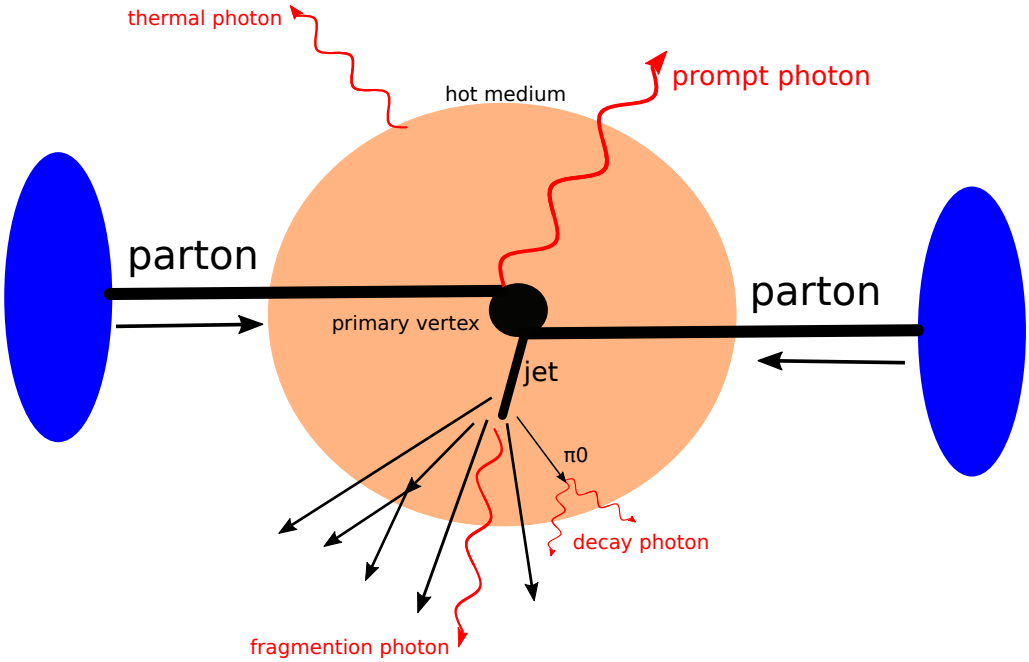

Figure 2.6: Production of the different kinds of photons. A parton will create a jet through hadronisation, which travels through the hot medium. The prompt photon and jet will be created back-to-back.

The prompt photons are produced directly from the initial collision (the hard scattering process) and consist of $2 \rightarrow 2$ processes, like *Compton scattering* ($q + g \rightarrow q + \gamma$) or quark-antiquark annihilation ($q + \bar{q} \rightarrow g + \gamma$), as shown in Figure 2.7. They are mostly produced back-to-back with a gluon or quark jet, which is extremely useful for the analysis of the QGP because it leads to a hadron-gamma correlation. The jet will travel through the QGP and lose energy, while the photons bypass it unchanged. Prompt photons are usually expected at high transverse momentum regions of $p_{\mathrm{T}} \gtrsim 5\,\mathrm{GeV/c}$ [14].

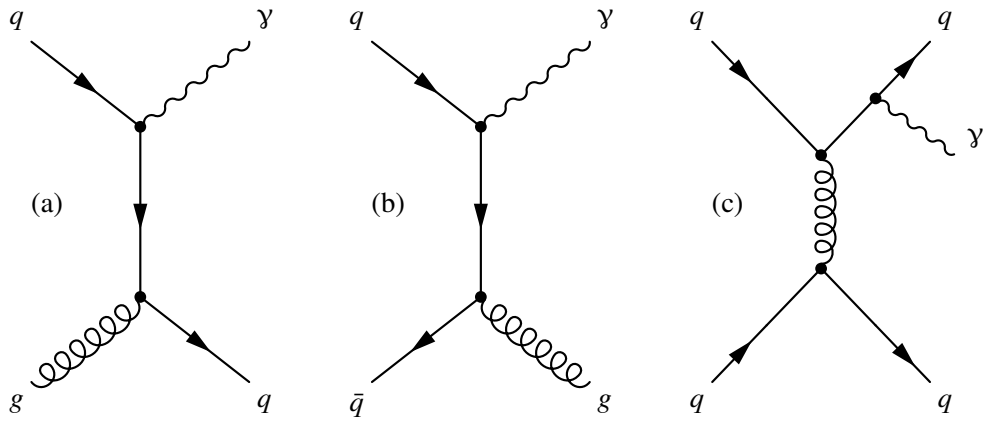

Figure 2.7: Feynman diagram of the possible prompt photon productions [15]. (a) quark gluon Compton scattering, (b) quark-antiquark annihilation and (c) Bremsstrahlung.

Fragmentation photons are created during the fragmentation and parton showering of jets, as partons can emit photons during hadronization.

Thermal photons are another group of photons, and they appear only in soft processes in heavy-ion collisions. They are the radiation of the hot medium and are therefore an important evidence of the QGP. As they are emitted at the thermal equilibrium and at the hadron gas stages, the thermal photons provide a method of temperature measurement for the QGP. Among all the produced direct photons, thermal photons are the most common, and it is experimentally not possible to differentiate between thermal and prompt photons. It is assumed, that thermal photons predominate the low transverse momenta regions at $p_T < 1.5 - 4\,\mathrm{GeV/c}$ [14].

A common problem with direct photon analysis is the abundance of decay photons. The hadronization and the subsequent decay of these particles creates the majority of photons, making the identification of direct photons challenging [15].

Pair Production If a photon γ has at least twice the rest mass energy of an electron ($2 \cdot 511\,\mathrm{keV} = 1022\,\mathrm{keV}$), it can create an electron-positron pair in the presence of a nucleus Z, $\gamma \rightarrow e^- + e^+$. The nucleus is required for the conservation of momentum, thus inducing a recoil. An increase in photon energy and in the density of nuclei increases the probability of pair production [16].

V^0 V^0 are neutral particles that decay into two charged particles. The name derives from the characteristic "V" shape of the decay track when visualized in a detector. The "0" indicates the neutral charge of the particle. Examples of V^0s are the K^0_S and the Λ. The former decays predominantly into a $\pi^+\pi^-$ pair, while the latter into a proton and π^-. In general, the V^0 particle itself is unknown and has to be reconstructed using the measured decay products at the secondary vertex, discussed in Section 4.4.

2.4.1 Kinematic Variables

Particle collisions have to be treated in a relativistic framework, where particles can be characterized with the *four-momentum* of

$$P^\mu = (E, \vec{p}) = (E, p_x, p_y, p_z), \tag{2.5}$$

with the energy E and the three-momentum $\vec{p} = (p_x, p_y, p_z)$ of the particle. The square root of the sum of the four-momenta of two colliding particles

$$\sqrt{s} = (P_1 + P_2) \tag{2.6}$$

corresponds to the center-of-mass energy of the collision. This energy is important because it determines the maximum reservoir of energy that can be converted into newly created particles.

For particle accelerators, usually a right-handed Cartesian coordinate system is used, with the beam pointing in the z-direction. The origin of the coordinate system (x,y,z)=(0,0,0) is at the beam interaction point (where the particles collide). The momentum can be divided into its longitudinal p_{L} and transverse p_{T} components:

$$p_{\mathrm{L}} = p \cdot \sin(\vartheta), \tag{2.7}$$

$$p_{\mathrm{T}} = p \cdot \cos(\vartheta), \tag{2.8}$$

with p as the magnitude of $\vec{p}$ and ϑ as the angle with respect to the beam axis. The transverse momentum p_{T} is preferred because the momenta of the colliding particles do not influence it. Additionally, the coordinate system can be written in spherical coordinates, as presented in Figure 2.8.

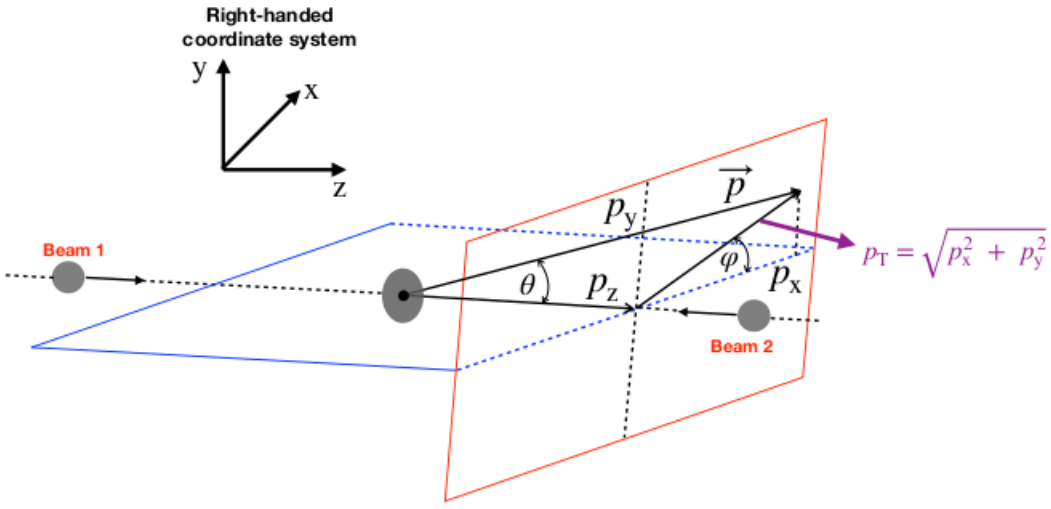

Figure 2.8: Schematic view of the coordinate system, with the interaction point as (0,0,0). While the angle φ surrounds the beam axis, ϑ and therefore η lay on the beam plane [17].

While the transverse momentum p_{T} is Lorentz-invariant under a boost in the z-direction, the longitudinal momentum p_{L} is not. To solve this problem, the *rapidity* y is used

$$y = \frac{1}{2} \ln\left(\frac{E + p_L}{E - p_L}\right), \tag{2.9}$$

which is additive under Lorentz transformation. If the energy E is far greater than the rest mass m_0 of the particle, which is the case in this analysis, the rapidity can be approximated with the *pseudo-rapidity* η:

$$\eta = -\ln\left[\tan\left(\frac{\vartheta}{2}\right)\right], \tag{2.10}$$

with the polar angle ϑ. With this, it is not required to know the energy or rest mass, but only the angle of the studied particles, and therefore the *pseudo-rapidity* η is widely used in experiments.

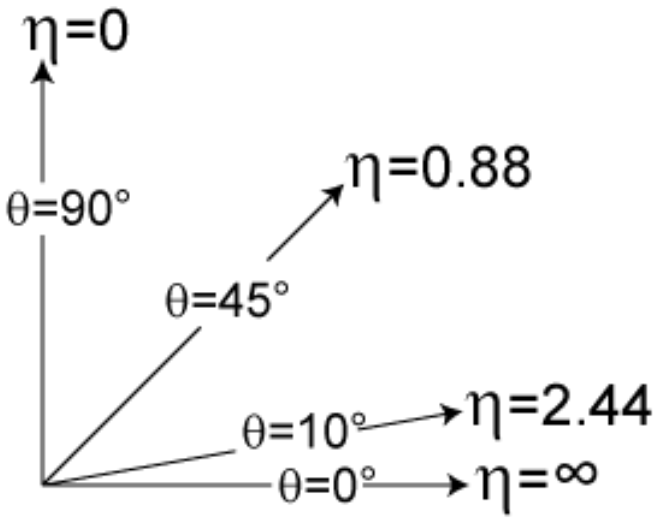

Figure 2.9: Different values for the pseudorapidity η [18].

In Figure 2.9, the pseudorapidity is depicted with the corresponding degree values.

3 The Experimental Set-Up and Software Framework

In this chapter, the particle accelerator *Large Hadron Collider (LHC)* and its detectors, along with the subsystems of one of the detectors, are explained. Moreover, the analysis software used for this analysis is presented.

3.1 Large Hadron Collider (LHC)

With a circumference 27 km, the LHC is currently the largest operating synchrotron particle accelerator. It is located at the *European Organization for Nuclear Research (CERN)* (Figure 3.1), in Geneva, Switzerland, up to 100 m below the ground.

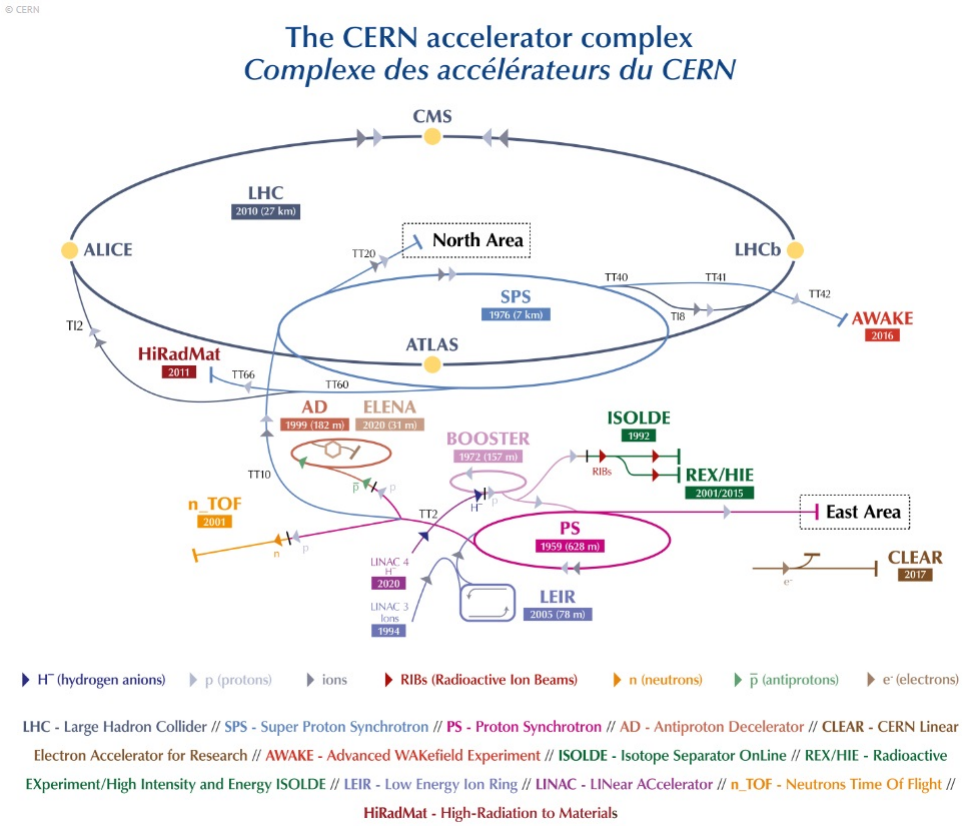

Figure 3.1: An overview of the CERN accelerators with the LHC and its experiments ALICE, ATLAS, CMS and LHCb [19].

The LHC consists of two beam pipes and eight interaction points, of which only half are in use for the experiments. In these pipes, protons can be accelerated to an energy of 6.5 GeV/c [20], resulting in a collision energy of 13 TeV/c (in Run 2). Additionally, heavy-ions such as the nuclei of lead, can be accelerated. For Pb-Pb, energies of $\sqrt{s} = 5.02$ TeV/c per nucleon-nucleon pair can be reached. The particles in the beam are collectively accelerated in *bunches* and the collisions occur at one of the four interaction points at the experiments.

To accelerate these protons or ions in the synchrotron, strong magnetic fields are necessary. For this purpose, 1232 superconducting dipole magnets are used to keep them in the LHC beams. The magnets, which have to be cooled down with liquid helium to 1.9 K for superconductivity, create a magnetic field of 8.36 T. Furthermore, 392 quadrupole magnets are additionally installed to focus the beam [21].

To create a proton beam, electrons are first stripped from hydrogen atoms. Afterwards, the protons are injected into the *Linear Accelerator LINAC 2*, providing a energy of 50 MeV/c. This proton beam now runs through an LHC pre-accelerator chain, called boosters. First, it enters the *Proton Synchrotron Booster (PSB*), then the *Proton Synchrotron (PS)* and afterward the *Super Proton Synchrotron (SPS)*. With each booster, the proton beam gets more energy, resulting in a final injection energy of 450 MeV/c. With this energy, it is injected into the LHC, where it is further accelerated to the maximum of 6.5 TeV/c [22]. As described earlier, only four of the interaction points at the LHC are equipped with experiments. These include *A Large Ion Collider Experiment (ALICE)*, *A Toroidal LHC ApparatuS (ATLAS)*, *Compact Muon Solenoid (CMS)* and *Large Hadron Collider beauty (LHCb)*. Each of these experiments is specialized on different properties of a particle collision and therefore provides different insights into potential new physics.

The ATLAS [23] and CMS [24] are general purpose detectors designed to confirm the existing Standard Model and study potential new physics, such as candidates for dark matter particles or supersymmetric particles. One of their goals was the discovery of the Higgs boson, which was achieved in 2012. The two detectors differ from each other through different technical setups, which is crucial for cross-checking the measured data and confirming each other's discoveries. The LHCb [25] is specialized on investigating the beauty (or bottom) quark. This research is aimed at finding new insights into the matter-antimatter asymmetry and the CP violation. The ALICE detector is the only experiment focused on heavy-ion collisions. Therefore, it will be described in more detail in this work.

3.2 A Large Ion Collider Experiment (ALICE)

The ALICE detector is 26 m long, 16 m wide and 16 m tall, and is specialized in the measurement of heavy-ion collisions to study the Quark-Gluon-Plasma and its transition phase. Due to the high multiplicity[1], ALICE is designed to handle this complexity while still providing accurate particle identification and maintaining a high momentum resolution at low transverse momentum. The detector can be seen in Figure 3.2.

[1] Number of detected charged particles.

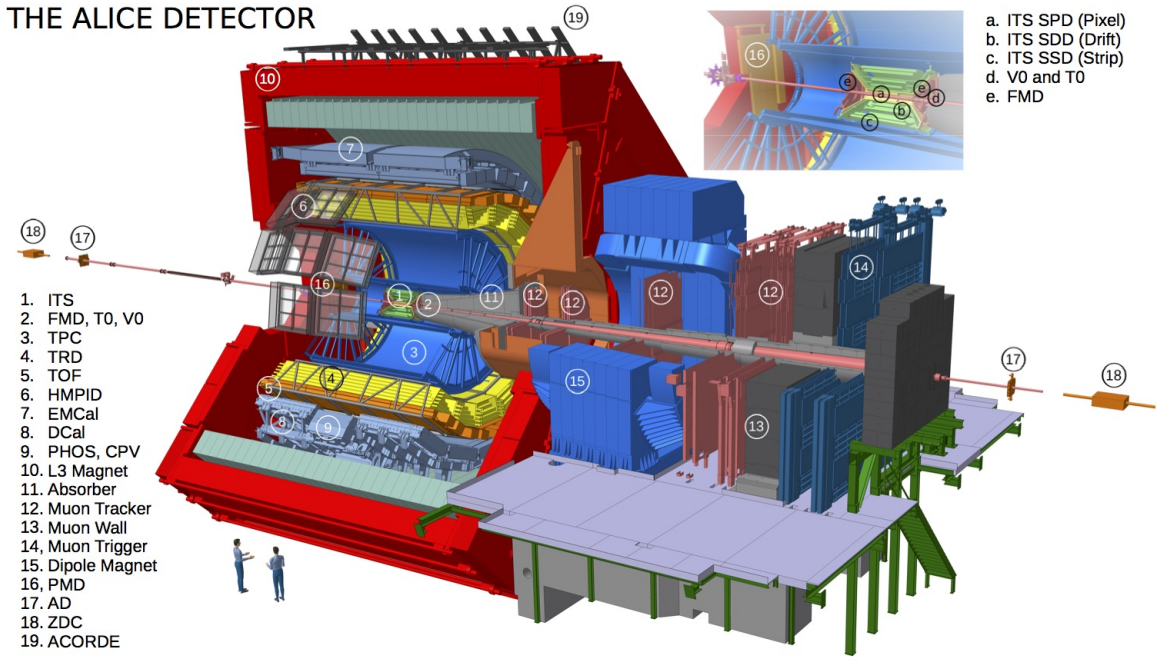

Figure 3.2: The ALICE Detector [26]. The subdetectors are installed cylindrically around the beam.

Closest to the beam are the subdetectors responsible for tracking, vertex finding and particle identification. The detectable particles first enter the *Inner Tracking System (ITS)*, then the *Time Projection Chamber (TPC)*, the *Transition Radiation Detector (TRD)*, the *Time-Of-Flight (TOF)*, the *High Momentum Particle Identification Detector (HMPID)* and finally the two calorimeters: the *Photon Spectrometer (PHOS)* and the *Electromagnetic Calorimeter (EMCAL)*. Forward detectors, such as the *V0 Detector (V0)*, are also present and located outside the central barrel [27]. The following Section will present in more detail the subdetectors that are particularly important for this work.

3.2.1 Inner Tracking System (ITS)

The Inner Tracking System (ITS) is the closest subdetector to the beam pipe, seen in Figure 3.3, and is used for the reconstruction of vertices[2]. Additionally, it can identify short-lived charged particles with a momentum of $p_{\mathrm{T}} < 200\,\mathrm{MeV/c}$, which would otherwise not reach the detectors further out. Lastly, it improves the momentum and angle resolution of other detectors, like the TPC.

The ITS has a maximum radial extension of $4 - 43.6\,\mathrm{cm}$ and covers a pseudorapidity range of $|\eta| < 0.9$, equal to $\pm 45°$. Therefore, vertices within $z = \pm 53\,\mathrm{mm}$ from the interaction point[3] can be detected and measured with a precision of more than $100\,\mu\mathrm{m}$. The detector consist of six layers of silicon detectors, which are placed radially around the pipe beam.

[2]Point of particle interaction or decay.
[3]The geometric center of the detector, where the beam pipe crosses.

The two layers closest to the pipe are the *Silicon Pixel Detectors (SPD)*. They contain 256×32 hybrid silicon pixel cells, which provides excellent spatial resolution. The next two layers are the *Silicon Drift Detectors (SDD)*, which measure the trajectory of charged particles through the drift of the electrons of the silicon and therefore provide two samples of dE/dx. The outer two layers are the *Silicon Strip Detectors (SSD)*. The silicon strips of this detector further enhance the track reconstruction of charged particles and give another two dE/dx samples. Moreover, the information from the SSD is essential for the track matching of the ITS and TPC [27].

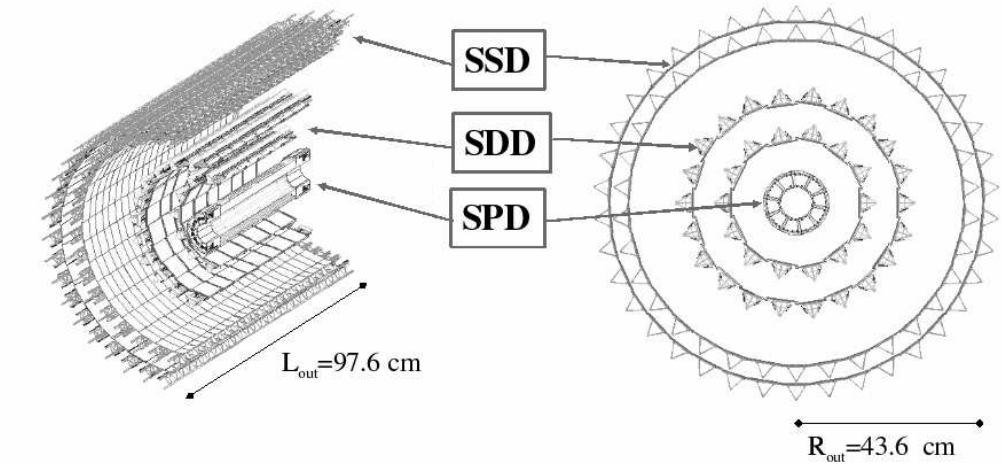

Figure 3.3: The Inner Tracking System, the closest detector to the beam pipe [27].

3.2.1.1 VZERO Detector (V0)

The V0 detector is used for event triggering[4] and centrality determination (in Pb-Pb collisions) and consists of two rings of scintillating arrays that surround the beam pipe. It is made up of the *V0-A*, with a pseudorapidity range of $2.8 \leq \eta \leq 5.1$ and the *V0-C*, with $-3.7 \leq \eta \leq -1.7$. It is a crucial component in the *ALICE minimum bias trigger system (V0AND)*, which distinguishes between various particle interactions and background noise. To trigger an event, a coincidental signal in both V0-A and V0-C must be detected. Additionally, in pp collisions, the event multiplicity is determined using the V0 detector[28].

3.2.2 Time Projection Chamber (TPC)

The Time Projection Chamber (TPC) is the main tracking device in the ALICE detector. It provides tracking with momentum of $p_{\mathrm{T}} < 0.7\,\mathrm{GeV/c}$ [29] and spatial resolution[5] and it is also used for particle identification (PID) via a dE/dx measurement. As shown in Figure 3.4, the TPC has a cylindrical shape with a radius of $85-250\,\mathrm{cm}$ and a length of $500\,\mathrm{cm}$. It covers the full azimuthal range, as well as the pseudorapidity range of $|\eta < 0.9|$, matching the dimensions of the ITS. The field cage is filled with $90\,\mathrm{m}^2$ of a gas mixture of $\mathrm{Ne/CO_2/N_2}$ (90/10/5 in

[4] An Event is defined as a single particle collision, including all produced particles and their decays. Triggering refers to the initiation of the data measurement.

[5] Position of a particle along its path.

2017), which has to be cooled to below 0.1 K due to the strong temperature dependency of the drift velocity of the gas mixture. The chamber is divided into two sections by a central high-voltage electrode, which acts as the anode. At both ends of the chamber, cathodes are placed, creating a homogeneous electric field with a strength of 400 V/cm. Additionally, a large solenoidal magnet is placed around the TPC, which creates a magnetic field of 0.5 T parallel to the beam pipe axis.

If a charged particle from an event now passes through the TPC, it ionizes the gas and creates free electrons. These electrons move towards the cathodes at the ends of the cage, due to the electric field, where the spatial resolution and energy loss[6] is measured with the read-out chambers. These chambers are equipped with rows of read-out pads, which are arranged in a grid. If an ionized electron reaches the end of the chamber, multiple pads detect this signal. These signals will be bundled into a single *cluster*. The spatial resolution is reconstructed using the drift time for the z-axis and the pads for the x-y-plane. The magnetic field induces a momentum-dependent helical curvature of the particle's trajectory. Combining this information with the results from the electric field, the particle mass and trajectories can be reconstructed [29].

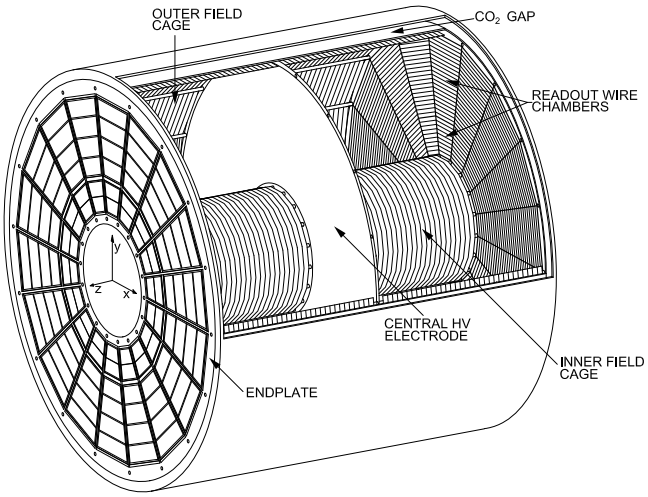

Figure 3.4: The TPC field cage, with its high voltage electrodes in the center and at the endplates [29].

Together with the ITS, the TPC can be used to detect conversion electrons (electron-positron pairs from photons interacting with the detector material), allowing the reconstruction of photons with the Photon Conversion Method (PCM). To achieve this, the tracks of the these e^+ and e^- have to be measured, and their secondary vertices, from which they originated, have to be located. These e^+ and e^- originate from neutral V^0 particles, which cannot be detected directly. The photons are selected based on their vertex properties, such as their topology. And while the TPC allows a large area of reconstruction due to its wide range in pseudorapidity and azimuthal angle, the probability for photons to convert in the ALICE material is limited to approximately 9 % [30].

As mentioned above, the TPC is also capable of measuring the energy loss of the particle per path length (dE/dx) using the drift gas. This is described by the Bethe-Bloch formula for

[6]The amount of free electrons (the ionization) is proportional to the energy loss of the particle in the gas.

elastic scattering, which is used to calibrate the energy loss of the TPC. Since this formula is dependent on the particle's energy, mass, and the traversing material, each particle has a characteristic energy loss. These phenomena are utilized in the ALICE for particle identification (PID). With its 160 clusters, the TPC can detect the dE/dx signals from tracks with a resolution of around 5 % [29]. Different cuts on this energy loss signal will be implemented in Section 4.4.

3.3 Analysis Software

To handle the large amount of data acquired from the ALICE detector and its subcomponents, special software analysis frameworks are required. During Run 2[7], the C++-based *ROOT* framework, along with the frameworks *AliRoot* [31] and *AliPhysics* [32], is used. For this analysis, ROOT 6.28/02 is used. ROOT provides a multitude of mathematical statistical tools, plotting and visualizations, that can be applied to the data. The package AliRoot is responsible for processing the raw data for reconstruction. It can additionally generate Monte Carlo (MC) simulations with generators like *PYTHIA8*. These simulate the real data, including kinematics and particle decays. With *GEANT3* it is possible to simulate the passages of the particle through the entire detector. AliPhysics is used to analyse the detector data and Monte Carlo simulations, and it can be used to correct for unwanted detector effects. To access the ALICE data, the framework *MonALISA* is used, which provides access to *ALIMONITOR*, the monitoring system for the ALICE detector.

[7]The second phase of data taking at the LHC, from 2015 to 2018.

4 Methods

This analysis studies proton-proton collisions at 13 TeV from Run 2, which were collected between 2015 and 2018 at ALICE. For the correlation functions, unidentified charged primary hadrons are used for trigger particles at $5 < p_{\mathrm{T}} \leq 10\,\mathrm{GeV/c}$. Depending on the specific analysis, either charged particles with $0.2 \leq p_{\mathrm{T}} \leq 5\,\mathrm{GeV/c}$ are used for the associated particles, or photons[1] are taken.

4.1 ALICE Data Sets

The data used in this analysis is obtained from of proton-proton collisions with a center-of-mass energy of $\sqrt{s} = 13\,\mathrm{TeV}$ collected by ALICE in 2017 during Run 2. These raw data are processed by the ALICE Data Processing Group, which manages and labels the data, e.g. pass1, pass2. The "pass" number indicates the latest processing set. This reflects an improved measurement for higher numbers, like more sophisticated calibrations, fixing of signal issues, etc. For this analysis, both pass1 and pass2 are utilized, which are part of the *Physics Working Group Gamma Analysis (PWGGA)*.

Each period of active detector data collection is stored in run lists. The Detector Performance Group (DPG) is the general form of storage, while *PCMgoodkINT7* has a specific selection criteria for the Photon Conversion Method with minimum Bias trigger (kINT7).

ALICE utilizes two data formats for analysis: *Event Summary Data (ESD)* and *Analysis Object Data (AOD)*. ESD consists of raw output data, representing the pure detector signals. The objects are reconstructed so that data, such as charged particle tracks, can be retrieved or the decay position can be obtained. AOD are pre-filtered ESD. It reduces the CPU consumption and storage space significantly, but still contains all essential information about the tracks and events. The filter of the AOD are chosen with filter-bits, which are sets of cuts. For this analysis, only AOD are taken with filter-bits AOD234 and AOD235.

With the data from GEANT3 and PYTHIA Monte Carlo, events and tracks can be reconstructed the same way as real data. This allows for a direct comparison of simulated and real data, which helps to estimate the detector efficiency. Also, the possible origins of the detected particles can be obtained. Within ALICE, specific PYTHIA simulations are anchored to the real dataset, meaning they are generated with the same conditions and properties as the real data.

[1] High-energy photons are called gamma particles. From here on, both will be used synonymously.

4.1.1 Hadron-Hadron and Hadron-Gamma from Real Data

For this analysis, the LHC17i dataset from GA_pp_AOD are chosen for the hadron-hadron correlation. Due to the lower statistics of hadron-gamma, additional datasets from LHC17 are taken. The datasets are shown in Table 4.1. Later, for the Monte Carlo analysis, the anchored dataset linked to the LHC17 data are taken. At last, LHC15h data with the setting PCMgoodkINT7 is used for comparison in the investigation of the particle origins.

Table 4.1: Datasets from real data.

System	$\sqrt{s}$	Year	Period	Pass	Run list	Use	Events
Dataset name: LHC17_13TeV_pass1_AOD234							
pp	13 TeV	2017	LHC17i	pass1	DPG	hadron-hadron	1.859e+08
pp	13 TeV	2017	LHC17c	pass1	DPG	hadron-gamma	6.608e+06
pp	13 TeV	2017	LHC17e	pass1	DPG	hadron-gamma	1.167e+07
pp	13 TeV	2017	LHC17f	pass1	DPG	hadron-gamma	1.165e+07
pp	13 TeV	2017	LHC17h	pass1	DPG	hadron-gamma	2.695e+08
pp	13 TeV	2017	LHC17i	pass1	DPG	hadron-gamma	1.700e+08
pp	13 TeV	2017	LHC17j	pass1	DPG	hadron-gamma	1.969e+07
pp	13 TeV	2017	LHC17k	pass1	DPG	hadron-gamma	4.454e+08
pp	13 TeV	2017	LHC17l	pass1	DPG	hadron-gamma	3.878e+08
pp	13 TeV	2017	LHC17m	pass1	DPG	hadron-gamma	4.769e+08
pp	13 TeV	2017	LHC17r	pass1	DPG	hadron-gamma	1.700e+08

4.1.2 Hadron-Hadron and Hadron-Gamma from Monte Carlo

For the Monte Carlo simulations, data from the *Analysis train* GA_pp_AOD_MC are used. A total of 17 datasets are analyzed, with 10 datasets directly linked (or anchored) to the data above, ensuring they share the same properties and conditions, as seen in Table 4.2. The additional datasets from run list listPCMgoodkINT7 are utilized for cross-checking purposes.

Monte Carlo data stores both Monte Carlo truth particles and Monte Carlo reconstructed tracks. In the former, all information is saved. They emulate a perfect particle collision, where everything could be measured ideally. The latter are particles, which undergo a simulated detector passage with GEANT3, aiming to closely mimic real particle detection [33]. The truth data are used to study the mother particles involved in the correlation functions, presented in Section 5.5. Together with the reconstructed data, the detector efficiency is determined, and additional Monte Carlo simulations are created.

Table 4.2: Datasets from Monte Carlo.

System	$\sqrt{s}$	Year	Period	Pass	Run list	Use	Anchored to	Events
Dataset name: PYT8_13TeV_anchLHC17_AOD235								
pp	13 TeV	2017	LHC17h1	pass2	DPG	Monte Carlo	LHC17e	2.060e+06
pp	13 TeV	2018	LHC18d3	pass2	DPG	Monte Carlo	LHC17c&f	4.524e+06
pp	13 TeV	2018	LHC18c12	pass2	DPG	Monte Carlo	LHC17h	1.680e+04
pp	13 TeV	2017	LHC17k4	pass2	DPG	Monte Carlo	LHC17i	1.461e+07
pp	13 TeV	2017	LHC17h11	pass2	DPG	Monte Carlo	LHC17j	8.976e+06
pp	13 TeV	2018	LHC18c13	pass2	DPG	Monte Carlo	LHC17k	2.484e+07
pp	13 TeV	2018	LHC18a8	pass2	DPG	Monte Carlo	LHC17l	1.381e+07
pp	13 TeV	2017	LHC17l5	pass2	DPG	Monte Carlo	LHC17m	1.280e+04
pp	13 TeV	2017	LHC18a9	pass2	DPG	Monte Carlo	LHC17o[2]	4.396e+05
pp	13 TeV	2018	LHC18a1	pass2	DPG	Monte Carlo	LHC17r	5.487e+06
Dataset name: PYT8_8TeV_anchLHC12_p2								
pp	8 TeV	2015	LHC15h1a1	pass2	PCMgoodkINT7	Monte Carlo	LHC12x	3.819e+07
pp	8 TeV	2015	LHC15h1b	pass2	PCMgoodkINT7	Monte Carlo	LHC12x	3.527e+07
pp	8 TeV	2015	LHC15h1c	pass2	PCMgoodkINT7	Monte Carlo	LHC12x	3.476e+07
pp	8 TeV	2015	LHC15h1d	pass2	PCMgoodkINT7	Monte Carlo	LHC12x	5.486e+07
pp	8 TeV	2015	LHC15h1f	pass2	PCMgoodkINT7	Monte Carlo	LHC12x	2.228e+07
pp	8 TeV	2015	LHC15h1h	pass2	PCMgoodkINT7	Monte Carlo	LHC12x	6.817e+07
pp	8 TeV	2015	LHC15h11i	pass2	PCMgoodkINT7	Monte Carlo	LHC12x	4.963e+06

Practical Implementation For the hadron-gamma data from the Monte Carlo simulation, reconstructed tracks are matched with their corresponding truth tracks. This process ensures that the complete information of the reconstructed tracks is accurately obtained, allowing the *Photon Conversion Method* to be employed correctly. Using this data, correlation functions are created. Multiple conditions are applied to the decay chain of the particles that are used here. First, the grandmother particle (1st generation) is selected with the *Particle Data Group (PDG)* codes. Independent of the chosen particle, the mother particle (2nd generation) should always be a γ-particle, and its transverse momentum is used for the correlation function. The final condition is that the daughter track (3rd generation) should always be an electron (e^-) or positron (e^+). For instance, if the grandmother is a π^0 meson, it decays into two γ-particles, whose momenta are measured, and these γ-particles will subsequently convert into an electron-positron pair.

4.2 Event Selection

To ensure the accuracy of the data used in this analysis, specific selection criteria are applied to both events and tracks. These criteria refine the dataset to only include meaningful collision events.

Minimum Bias *Minimum Bias (MB)* events are those with a minimal selection criteria, resulting in a dataset with as little bias as possible. This allows for a large sample of collision events to be collected, which opens a broad spectrum of possible options to analyze these events. MB does not take the multiplicity into account; all events indicating an interaction are included.

For the events in this analysis, the *kINT7* minimum Bias trigger is used. This trigger relies on coincident signals from the V0A (forward rapidity ranges) and V0C (backward ranges) detectors. Thus, for an event to be selected, its corresponding particles must be detected in forward and backward rapidity ranges. The timing information from these two detectors is crucial for distinguishing true collision events from background noise.

Underlying Event The *underlying event (UE)* encompasses all particles and interactions in an event that are not directly associated with a hard scattering event. This can include the remnants of beam particles or soft scattering. Therefore, it represents the "background" activity of the hard scattering event.

Primary Vertex Position The primary vertex position is selected to be $\pm 10\,\mathrm{cm}$ along the z-axis from the interaction point. This ensures that the majority of the tracks are within the detector's acceptance range.

4.3 Track Reconstruction

To ensure that tracks have a sufficient quality and that only particles originating from the primary vertex are analyzed, several selection criteria have to be applied to the tracks, listed in Table 4.3.

These selection criteria are stored in AliRoot and can be selected with the appropriate *filter-bit*, depending on the analysis. For this analysis, "*Standard track with tight DCA cuts*" is used. This is the AOD corresponding filter-bit of 96, which is a combination of 64 and 32. The individual selection options can be checked in the AliPhysics class **AliESDtrackCuts.cxx**.

Table 4.3: Applied track cuts.

Used function name	Value
TPC	
SetMinNCrossedRowsTPC	70
SetMinRatioCrossedRowsOverFindableClustersTPC	0.8
SetMaxChi2PerClusterTPC	4
SetMaxChi2TPCConstrainedGlobal	36
SetRequireTPCRefit	kTRUE
SetAcceptKinkDaughters	kFALSE
ITS	
SetMaxDCAToVertexXYPtDep	$0.0105 + 0.0350/\mathrm{p}_T^{1.1}$
SetMaxDCAToVertexZ	2
SetDCAToVertex2D	kFALSE
SetRequireSigmaToVertex	kFALSE
SetMaxChi2PerClusterITS	36
SetRequireITSRefit	kTRUE
SetClusterRequirementITS	kSPD, kAny
SetClusterRequirementITS	kSPD, kNone
SetClusterRequirementITS	kSDD, kFirst

With this setting, tracks have to cross at least 70 TPC pad rows. Furthermore, it can happen that an ionized electron triggers multiple pads while the expected number of received clusters is lower. Therefore, the ratio of cross-pad rows over findable clusters must be 80 %. The maximal fitting χ^2 value of the tracks per cluster in the TPC is 4, while for the constrained global tracks, it is 36. Also, the tracks for the TPC are refitted and Kink daughters[3] will not be accepted.

In the ITS, the tracks have to obey the same maximal fitting χ^2 value for clusters and are also refitted. The *Distance of Closest Approach (DCA)*, which is the shortest distance between the particle track and the primary vertex, has two restrictions in its location. The maximum allowed transverse (x-y-plane) DCA length depends on the transverse momentum, with the formula $0.0105 + 0.0350/p_{\mathrm{T}}^{1.1}$. This means, that higher momentum allows for more deviation. In the longitudinal direction (z-direction) 2 cm deviation is allowed. For the tracks in the ITS, neither a 2D nor a sigma cut on the vertex DCA is required. The 2D cut is unnecessary because a p_{T} cut is applied and no expected value for sigma is specified. Additionally, tracks must have a cluster in the SPD and in at least one of the other two scintillators.

[3] Kink daughters occur when a charged particle decays into a neutral and charged particle. Since the neutral particle cannot be detected, it appears as a kink in the trajectory of the charged particle.

Lastly, a more precise cut is implemented. This will take effect after the previous one, so no hit in the SPD is required, as it would be redundant. However, the track must have a cluster in the first layer of the SDD to be accepted. All the cuts ensure that the resolution of the DCA is very large (meaning that the DCA itself is small), and therefore a good differentiating of particles originating from secondary and primary vertices is ensured. This is important for the correlation function to ensure that the correlated particles are indeed from the same vertex. Consequently, a constant distribution in the φ-plane is also provided, resulting in a clear back-to-back distribution.

Primary Particles Within ALICE, *primary particles* are defined as particles with a mean proper lifetime $\tau > 1\,\mathrm{cm/c}$. These particles are either directly produced in the initial collision or are decay products from particles with τ smaller than $1\,\mathrm{cm/c}$. For example, a π^0 has a lifetime τ smaller than $1\,\mathrm{cm/c}$ and will most likely decay into two photons. These photons are considered primary particles, but not the π^0. This ensures that double counting of, for example, momentum does not happen when summing over primary particles [33]. This is implemented in the code using the boolean function **track->IsPhysicalPrimary()**[34].

4.4 Photon Reconstruction and Selection Criteria

The *Photon Conservation Method (PCM)* is employed in this analysis to reconstruct γ-particles. This chapter provides an explanation of the method, followed by the necessary cuts. PCM identifies and measures photons indirectly by detecting electron-positron (e^-e^+) pairs that are produced when photons interact with the active and inactive detector material. Since other particles, such as the neutral meson Λ, can also decay into e^-e^+, a specific set of cuts is needed to remove these unwanted decays[4]. The TPC and ITS are the primary detectors for the PCM [35].

[4]The subtraction of the combinatorial background.

Track Selection Table 4.4 shows the track cuts and the V^0 selection cuts.

Table 4.4: Criteria for PCM analysis.

	pp, $\sqrt{s}$=13 TeV
Track selection	
V0-finder algorithm	On-the-fly
track p_T	$> 0.05\,\mathrm{GeV/c}$
$\frac{N_{clusterTPC}}{N_{finableclusters}}$	$> 60\,\%$
	$\lvert\eta\rvert < 0.9$
Particle identification cuts	
Electron selection	$-4 < n\sigma_e < 5$
Pion rejection	$n\sigma_\pi < 1$ for $p > 0.4\,\mathrm{GeV/c}$
V0 Cuts	
Conversion point	$\lvert\eta_{V^0}\rvert < 0.9$
	$5\,\mathrm{cm} < R_{\mathrm{conv}} < 180\,\mathrm{cm}$
	$\lvert Z_{conv}\rvert < 240\,\mathrm{cm}$
	$0 \leq \lvert\varphi_{\mathrm{conv}}\rvert \leq 2\pi$
	$\cos(\theta_{\mathrm{point}}) > 0.85$
Photon selection criteria	
Armenteros-Podolanski	$q_T < q_{T,\max}\sqrt{1-\frac{\alpha^2}{\alpha^2_{\max}}}$, with $q_{T,\max} = 0.05\,\mathrm{GeV/c}$ and $\alpha_{\max} = 0.95$
Photon quality	$\lvert\psi_{\mathrm{pair}}\rvert < \psi_{\mathrm{pair,\,max}} - \frac{\psi_{\mathrm{pair,\,max}}}{\chi^2_{\mathrm{red,\,max}}}\chi^2_{\mathrm{red}}$, with $\psi_{\mathrm{pair,\,max}} = 0.1$ and $\chi^2_{\mathrm{red,\,max}} = 30$

In this analysis, the on-the-fly V^0 finder algorithm is used, because it offers a large efficiency at low transverse momentum. Additionally, no assumption for the mass of the daughter particle is needed, therefore no geometrical consideration is made. The tracks considered for reconstruction must have a minimum momentum of $0.05\,\mathrm{GeV/c}$ and at least $60\,\%$ of them must activate all possible reconstructable clusters. This requirement is due to the fact that the number of reconstructable clusters in the TPC depends on the conversion point.

Additional cuts are applied to the electrons and pions to improve the selection of photons from the remaining V^0 particles. These cuts are based on the theoretical energy loss line dE/dx in the TPC. The allowed standard expectation range for electrons is $-4 < n\sigma_e < 5$ and for pions, it is $n\sigma_\pi < 1$ for $p > 0.4\,\mathrm{GeV/c}$, everything outside these ranges is cut off.

$$n\sigma_x = \left(\frac{dE}{dx} - \langle\frac{dE}{dx_x}\rangle\right)/\sigma_x \tag{4.1}$$

with $\langle \frac{dE}{dx_x} \rangle$ as the average energy loss and σ_x as the resolution for a particle x. These are tight cuts to minimize contamination from pions. The effects of these cuts are illustrated in Figure 4.1.

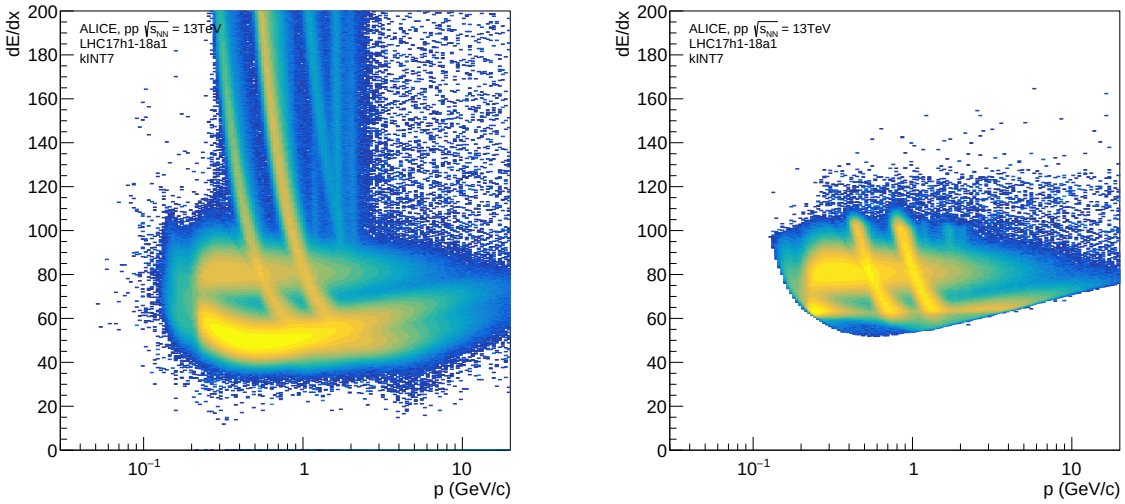

Figure 4.1: The TPC dE/dx distribution of the secondary tracks before (left) and after (right) the selection cuts.

To further remove contamination, additional *Particle Identification (PID)* methods from other ALICE subdetectors could be employed. For example, electrons can be identified using their energy loss dE/dx in the ITS, with the time-of-flight measurement in TOF, with the transition radiation or dE/dx in TRD or with the energy deposits in the calorimeter. However, all of these would decrease the reconstruction efficiency significantly, so they will not be applied.

V0 Selection Since the η cut in the Z-R-plane does not take into account the starting point of the track, an additional cut has to be applied to ensure that the particles fall within the geometrical acceptance of the detector. In this line-cut in the geometrical η distribution of the conversion point, the center of the detector acts as the origin. The latter can be described with

$$S_{Z-R_{\text{slope}}} = \tan(2 \cdot \arctan(\exp^{(-\eta_{cut})})). \tag{4.2}$$

With that, the cut is defined as

$$R_{\text{conv}} > |Z_{conv}| \cdot S_{Z-R_{\text{slope}}} - Z_0, \tag{4.3}$$

with $Z_0 = 7\,\text{cm}$. R_{conv} and Z_{conv} are the radial and longitudinal coordinates of the secondary vertices, measured with respect to the nominal center of the detector. Z_0 accounts for the spread of the primary vertex position, and no other smearing cut is considered. By setting $R_{\text{conv}} < 180\,\text{cm}$ and $|Z_{conv}| < 240\,\text{cm}$, it is ensured that the secondary track reconstruction remains within the TPC barrel. With the minimum cut of $5 < R_{\text{conv}}$, contamination of neutral meson Dalitz decay can be avoided.

Secondary Vertex Finder To reconstruct the conversion photons from the e^-e^+ pair, a secondary vertex finder is used. This tool utilizes secondary tracks to reconstruct the V^0. These tracks originate from secondary vertices, which result from the decay of particles rather than from the primary vertex (the initial collision). The reconstruction begins with the selection of two oppositely charged tracks. Their impact parameters $(b, b+)$ with regard to the primary vertex are calculated, and a minimum length cut is implemented. This cut is necessary because very small impact parameters indicate that the tracks originate directly from the primary vertex. Subsequently, the DCA is calculated. For this, the tracks have to exceed the minimum threshold for the impact parameters. The DCA needs to be small, at most 1 cm, depending on the distance R to the primary vertex and its resolution; otherwise, the tracks are rejected. For the accepted track pairs, the V^0 candidates are created by setting the secondary vertex to the point-of-closest-approach of the two tracks, as indicated by the red dot in Figure 4.2. Additionally, the fiducial zone can be seen in this sketch, spanning from 5 cm to 180 cm radially from the primary vertex (dotted red circles). Secondary vertices are reconstructed only within this zone. The V^0 momentum vector P is also required. This vector is obtained by extrapolating the momenta of both tracks to the DCA and summing them at that point. It is essential that this vector point, towards the primary vertex, otherwise it is rejected. To ensure this, the cosine of the angle θ_{point} between the P and the vector R (which connects the secondary vertex to the primary vertex) must be greater than 0.85. If the cosine is less than 0.85, the V^0 vector is rejected [35]. Figure 4.2 illustrates the two vectors P and R, which are shown pointing in the travel direction of the particles.

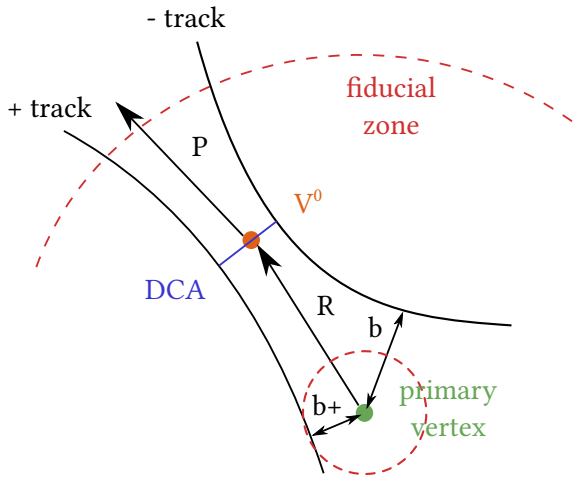

Figure 4.2: Sketch of the primary and V0 vertices from charged tracks [36].

Photon Selection Additional cuts are necessary to obtain the photon sample due to the presence of the combinatorial background. While the sample predominantly consists of electron-positron conversion pairs, these pairs can originate from various particles, like K^0_S, Λ or $\bar{\Lambda}$, and not exclusively from the desired photons. Therefore, two additional cuts are applied to further enhance the photon purity.

First, a 2D elliptic cut is applied using the Armenteros-Podolanski [37] variables:

$$q_T = p_{\text{daughter}} \cdot \sin\theta_{(\text{mother-daughter})} \tag{4.4}$$

$$\alpha = \frac{(p_L^+ - p_L^-)}{(p_L^+ + p_L^-)} \tag{4.5}$$

Here, q_T represents the transverse momentum of the daughter particle relative to the mother particle. Therefore, a low q_T indicates a close alignment of the daughter particle with the direction of the mother particle, which is typical for photons due to their zero mass. In contrast, heavier particles like K^0_S or Λ have a larger q_T and a larger opening angle relative to the mother particle's direction.

The longitudinal momentum asymmetry, α, indicates the mass difference between the daughter particles. If daughter particles have similar or equal mass, such as in $\gamma \rightarrow e^- e^+$ or $K^0_S \rightarrow \pi^+ \pi^-$ decays, the symmetry is high, resulting in an α close to 0. Decays involving daughter particles with significantly different masses, like $\Lambda \rightarrow p + \pi^-$, large asymmetries with $\alpha = \pm 1$ emerge. The lighter particle, in this case the pion, will diverge more from the direction of the mother particle due to the larger momentum it received.

Both of these variables are shown together in an Armenteros-Podolanksi-Plot, as shown in Figure 4.3. Here, the symmetric distribution of the γ is visible. Photons having a q_T close to 0, while the asymmetry of Λ and $\bar{\Lambda}$ can be seen at around $\alpha = \pm 0.7$

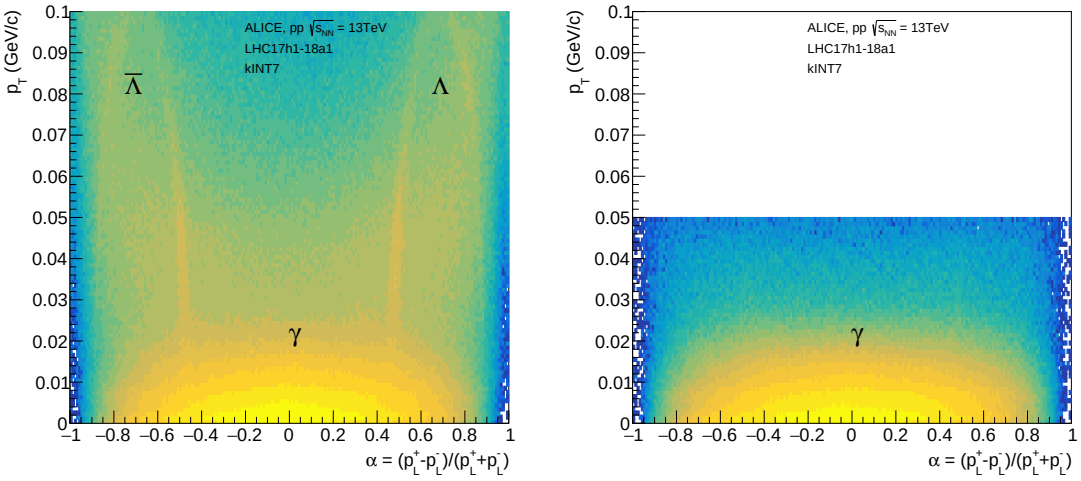

Figure 4.3: Armenteros-Podolanski-Plot of all V^0 candidates before (left) and after (right) the photon selection cuts for the $\sqrt{s} = 13\,\text{TeV}$ data set.

In this figure, the impact of the 2D elliptic cut with $q_T < 0.05\,\text{GeV/c}$ and $\alpha = 0.95$ is clearly visible. The unwanted contamination from Λ or $\bar{\Lambda}$ is removed from the V^0 sample. Note that the y-axis in the left plot of Figure 4.3 only extends to 0.1, despite being set to 0.25. However, this is not a significant issue since this region is removed due to the filter setting.

An additional triangular 2D cut in χ^2 and Ψ_{Pair} is employed to further reduce the amount of unwanted electron-positron pairs. The chi-square value from a photon conversion fit is used. The fit is based on a generic particle decay model utilizing the Kalman filter method to reconstruct V^0 particles. This method requires the particle to be massless and to originate from the primary vertex. After the tracks have traveled 50 cm from the conversion point, the angle Ψ_{Pair} is calculated (see Equation 4.6). This angle is based on the opening angle of the electron-positron pair from the photon conversion. Since the bending of the tracks in the magnetic field is relatively small, the cut is defined as follows:

$$\Psi_{\text{Pair}} = \arcsin\left(\frac{\Delta\theta}{\xi_{\text{pair}}}\right), \tag{4.6}$$

with the angle between the two daughter tracks in polar direction, $\Delta\theta = \theta_{e^-} - \theta_{e^+}$ and

$$\xi_{\text{pair}} = \arccos\left(\frac{\vec{p_{e^-}} \cdot \vec{p_{e^+}}}{|\vec{p_{e^-}}| \cdot |\vec{p_{e^+}}|}\right), \tag{4.7}$$

with ξ as the angle between the propagating daughter tracks, as displayed left in Figure 4.4. Therefore, Ψ_{Pair} is the arcsin of the ratio of these two angles. While $\Delta\theta$ remains constant, the opening angle of two tracks changes due to the magnetic field.

Applying a cut on Ψ_{Pair} helps to reduce unwanted track combinations by limiting the ratio of the initial opening angle of the electron-positron pair (right after creation) to the opening angle measured 50 cm away from the conversion point [38]. For this analysis, Ψ_{Pair} chosen with a maximum value of 0.1, and the χ^2 per degree of freedom cut is set at 30 [35] [39] [40].

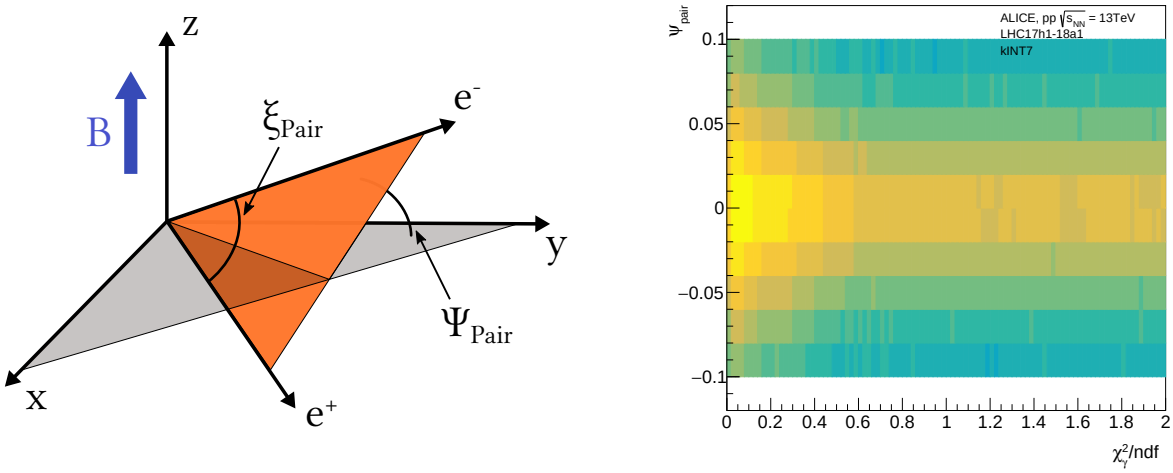

Figure 4.4: Sketch Ψ_{Pair} (left) [41], with the grey area as the magnetic field. On the right is Ψ_{Pair} with χ^2 after the cuts are applied.

Note: Similar to the Armenteros-Podolanski-Plot, the plot in Figure 4.4 only extends to 2, while being set to 30. This should also not be of concern because the low χ^2 indicates a good fit of the data.

4.5 Corrections

Due to the non-perfect environment of experiments, a variety of corrections have to be applied.

4.5.1 Event Mixing

The TPC and ITS have a physical limitation of $\eta = \pm 0.9$ ($\approx \pm 50°$), which results in a characteristic triangular shape in the correlation function, as depicted left in Figure 4.5.

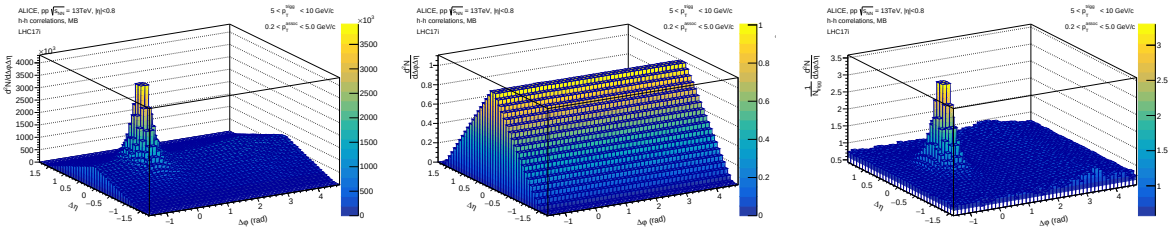

Figure 4.5: An example of the *event mixing method* correction with hadron correlation. Left: an unwanted triangular artifact at the bottom can be observed. Middle: the triangular mixed correlation function for correction. Right: the corrected correlation function.

To correct this, the *event mixing method* is employed. Correlated events are compared with similar non-correlating events. First, multiple tracks from multiple events with similar centrality and primary vertex position are saved in a pool. The primary vertex has to be within $\pm 10\,\text{cm}$ of the interaction point and the multiplicity within the same percentile binwidth of $10\,\%$. After the pool is filled with sufficient data, a triangular shaped correlation function can be obtained, as presented in the central figure in 4.5. It is normalized to unity to ensure that it does not change the multiplicity of the correlation function in the correction process. Afterward, it is divided with the uncorrected correlation function to obtain the corrected correlation function, which is depicted in the right figure in 4.5.

The true correlation function is:

$$\frac{d^2N_{pair}}{d\Delta\varphi d\Delta\eta}(\Delta\varphi\Delta\eta) = \sum_i \frac{S_i(\Delta\varphi\Delta\eta)}{\frac{1}{\alpha_i}M_i(\Delta\varphi\Delta\eta)}. \tag{4.8}$$

The sum goes over the different primary vertex position bins α_i. $S_i(\Delta\varphi\Delta\eta)$ is the correlation function from tracks of the same events and $M_i(\Delta\varphi\Delta\eta)$ the correlation function from the mixed events. Therefore, the insufficient detector range gets corrected.

4.5.2 Corrections for the p_T Spectra

For the p_T spectra, multiple corrections are applied on the raw data. In raw data, the y-axis is labeled with N_{ch} the number of charged particles (multiplicity) in units of counts.

Bin Width First, the histogram of the momentum spectra must be scaled by the bin width. This is accomplished using the function **h->Scale(1.,"width")**. This ensures that the height of each bin is proportional to the event count, regardless of the binning used. Without this scaling, the histogram with narrower bins would appear visually smaller. This scaling for bin width is essential for any meaningful comparison with other data. The y-axis changes from N_{ch} to $\frac{dN_{\mathrm{ch}}}{dp_T}$. This correction is needed for all histograms created in ROOT, including the histograms of the correlation functions.

Normalization The spectra are also normalized. The full momentum spectrum is normalized to the number of events. This number is taken from the analysis, where it is counted and used in the function **h->Scale(1./NumberOfEvents)**, to implement the normalization. The associated momentum spectrum is normalized by the number of trigger particles, since the associated particles depend on them, **h->Scale(1./NumberOfTriggerParticles)**. The number of trigger particles is acquired through integration of the trigger momentum spectra **NumberOfTriggerParticles = h->Integral("width")**. The per event normalization leads to an additional $\frac{1}{N_{\mathrm{event}}}$ term to the y-axis, while the per trigger normalization results in a $\frac{1}{N_{\mathrm{trigg}}}$ factor. This normalization is an important part of comparability with other experiments because it is impossible to get the same amount of events in different experiments. With this correction, the spectra show the number of trigger particles per events, or the number of associated particles per trigger particle.

Invariant Yield The invariant yield Y [42] is the Lorentz-invariant production rate of particles, thus it is independent of the reference frame. This is needed for comparison with other data and experiments. It is derived from the Lorentz-invariant cross-section σ_{inv}, and is given by,

$$Y = \frac{1}{N_{\mathrm{events}}} \frac{1}{2\pi p_{\mathrm{T}}} \frac{d^2N}{dp_T d\eta}. \tag{4.9}$$

The invariant yield is implemented in multiple steps.

First, multiplying the histogram with $\frac{1}{2\pi}$, through **h->Scale(1./(TMath::TwoPi()))** and with $\frac{1}{1.6}$, which represents the length of the η acceptance given by $\frac{dN}{d\eta}$, because the pseudo-rapidity is 0.8 in positive and negative direction. Lastly, each bin is divided by its p_{T} value. This results in the $\frac{1}{p_{\mathrm{T}}}$ term. The code for the latter is:

```
for(int i=1; i<h->GetNbinsX()+1; ++i) {
    h->SetBinContent(i, h->GetBinContent(i)/h->GetXaxis()->GetBinCenter(i));
}
```

Background For correlation functions, the presence of uncorrelated particle pairs from underlying events means that the minimum value of the function can never reach zero. This background must be subtracted to accurately describe the true correlation. To achieve this, the value of the minimum bin, which represents the background level, is subtracted from all bins in the correlation function.

4.5.3 Single Particle Efficiency with Monte Carlo

The detector cannot reconstruct all particles with an efficiency of 100%. Therefore, a single particle efficiency correction must be applied to account for the imperfection of the detector. This correction is performed using Monte Carlo simulations that are processed with the same selection criteria as the real data. Additionally, it is verified whether a selected track is associated with a primary particle. The single particle efficiency ε is determined using a Monte Carlo simulation and is defined as:

$$\varepsilon = \frac{N^{\text{primary}}_{\text{reconstructed}}}{N^{\text{primary}}_{\text{generated}}}$$

$N^{\text{primary}}_{\text{generated}}$ is the number of generated primary hadrons. It comes from the Monte Carlo truth simulations, which emulate an ideal particle collision where all information could be retrieved. $N^{\text{primary}}_{\text{reconstructed}}$ is the number of reconstructed primary particles that are reconstructed from Monte Carlo using GEANT3. This spectrum is lower than the truth simulation because of effects such as reconstruction loss of the detector or the detector resolution.

The Monte Carlo truth simulation is retrieved with

```
1    AliMCEvent* fMCEvent_true = dynamic_cast<AliMCEvent*>(MCEvent());
```

while Monte Carlo reconstructed simulations are obtained with:

```
1    AliVEvent* fMCEvent_reco = InputEvent();
```

4.5.3.1 Charged Particles

The single particle efficiency for charged particles ε_{ch} is presented in Figure 4.6.

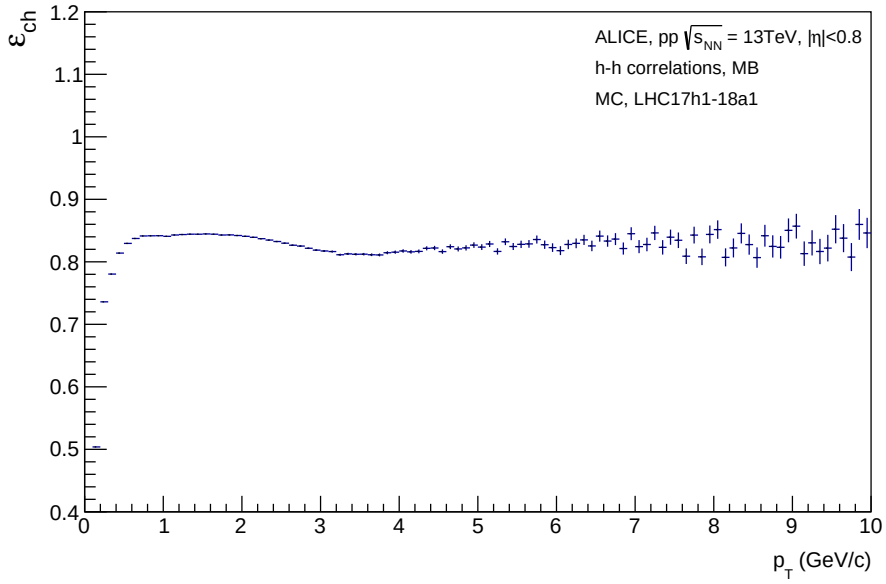

Figure 4.6: Single particle efficiency for charged particles.

There is a steep increase in efficiency in the low p_{T} region, rising from around 50% at 200 MeV/c up to 85% at 500 MeV/c. This initial increase can be attributed to the low resolution of the detector at low transverse momentum. This can be explained by the behavior of the particle in the magnetic field of the detector. At low momenta, particles have greater curvatures in their trajectories, preventing them from reaching enough detector layers to get detected. Additionally, low-momentum particles lose more energy, through interactions with the detector material, decreasing detection even further. The curvature of a particle's trajectory can be calculated following the relation $R = p_{\mathrm{T}}/(qxB)$, with the electric charge $q = \pm 1$ and the magnetic field strength $B = 0.5\,\mathrm{T}$. For example, a particle with a transverse momentum of 0.2 GeV/c has a curvature radius of $R = 40\,\mathrm{cm}$. Given that the ITS has a tracking range of 3.9 cm to 43 cm, and the TPC of 85 cm to 200 cm, such low p_{T} particles may not reach the TPC. In this case, it cannot provide enough hits for a valid track, resulting in lower efficiency. As the transverse momentum increases, more particles can traverse both the ITS and TPC, leading to improved tracking efficiency. At around 3 GeV/c, the efficiency decreases slightly and stays afterward at around 80%. This could be due to the straighter trajectory of high p_{T} particles. If the trajectory is very straight, the particles can travel between the detector segments, and thus they cannot be detected. Therefore, 80–85% of all charged particles are successfully reconstructed in the real data.

4.5.3.2 Photons

The single particle efficiency for photons ε_γ, see Figure 4.7, possesses a similar shape to that of charged particles, but it is significantly lower. It reaches a maximum of approximately 8.6% at around 2 GeV/c.

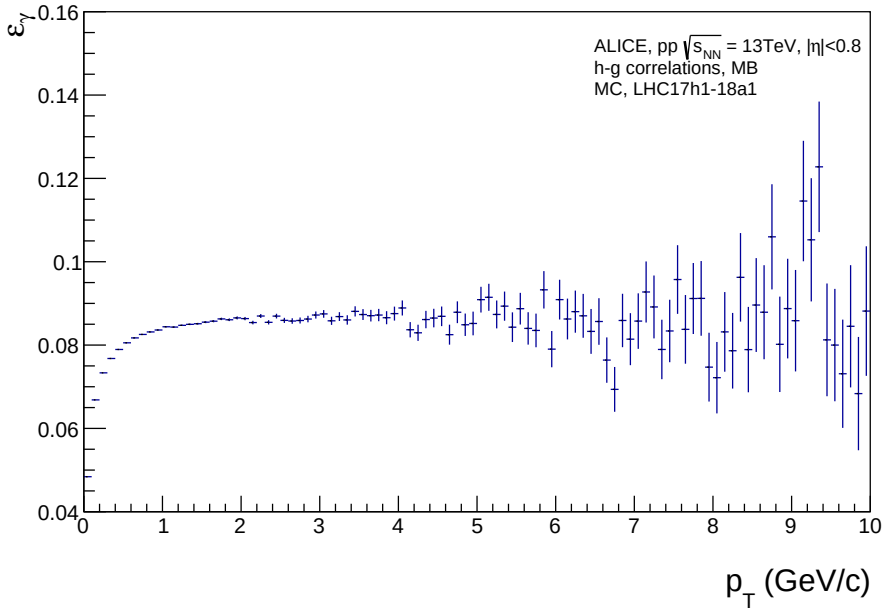

Figure 4.7: Single particle efficiency for γ particles.

This low efficiency indicates that only a small fraction of primary photons can be successfully reconstructed by the detector. The limited amount of detector material that can be used for photon conversion is a factor. Especially the gas mixture in the TPC, which contributes to the largest amount of the volume of the detector, has a low density. Therefore, the chance for a photon to convert into an electron-positron pair is fairly low. Additionally, the track and event cuts in this analysis are tight, which also lowers the amount of accepted photons. The small efficiency at low p_T can be explained analogously to the one above for the charged particles.

4.6 p_T Spectra

The full momentum spectra for the hadron-hadron dataset with range from $0.2 \leq p_{\mathrm{T}} \leq 10\,\mathrm{GeV/c}$, $|\eta| < 0.8$ and all corrections can be seen in Figure 4.8.

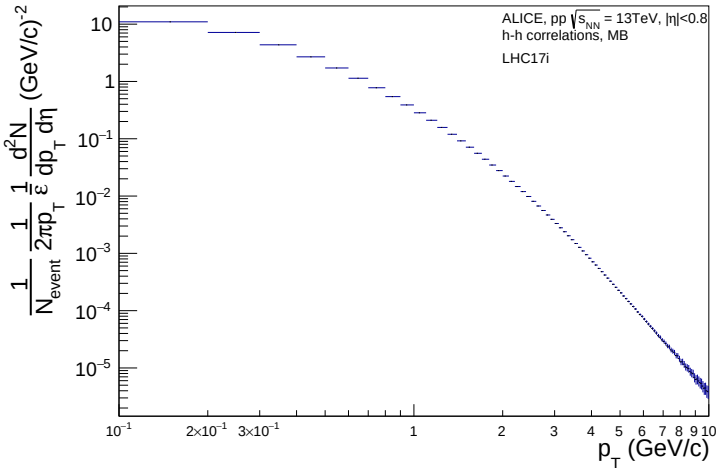

Figure 4.8: Full momentum spectra with all corrections.

In this spectrum, the majority of produced particles are found at the lowest transverse momentum values. As the momentum increases, the number of particles decreases. This can be explained by the energy required to produce these particles. Light particles like π^+ with a rest mass of $139.57\,\mathrm{MeV/c^2}$ have a significantly higher probability of being produced compared to heavier particles. Thus, the overall particle production is dominated by these light particles. For the di-hadron correlation functions, the associated particles (Figure 4.10) have transverse momenta in the range of $0.2 \leq p_{\mathrm{T}}^{\mathrm{assoc}} \leq 5\,\mathrm{GeV/c}$ and the trigger particles (Figure 4.9) of $5 < p_{\mathrm{T}}^{\mathrm{trigg}} < 10\,\mathrm{GeV/c}$. The trigger particles should be above $5\,\mathrm{GeV/c}$ in pp collisions to ensure that at least one track is detected per event. The p_{T} limit for associated particles is chosen to increase the probability of detecting charged particles, given the relatively low number of high p_{T} particles.

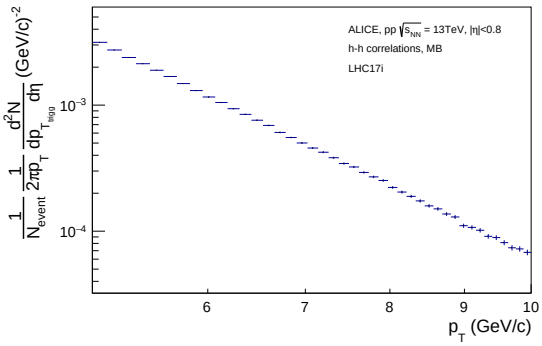

Figure 4.9: p_{T} spectrum of the trigger particles normalized on the number of events.

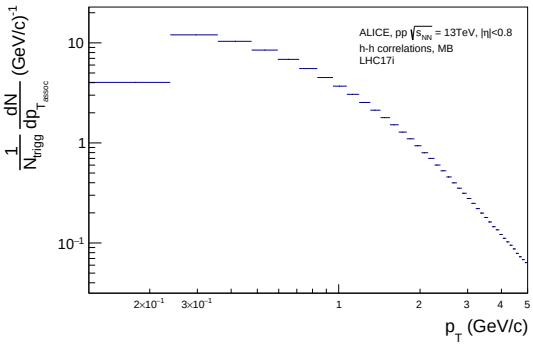

Figure 4.10: p_{T} spectrum of the associated particles normalized on the number of trigger particles.

4.6.0.1 Comparison with Simulations

The simulated Monte Carlo truth spectra can be compared with the real data. Figure 4.11 shows the Monte Carlo truth p_{T} spectra, simulated with Pythia8, alongside the corrected p_{T} spectra from real data.

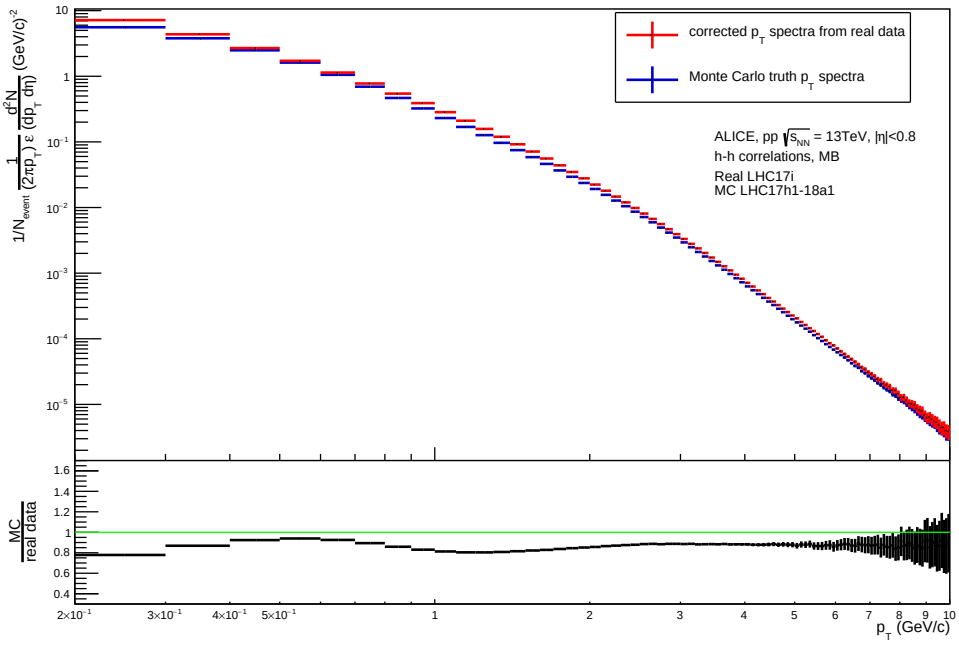

Figure 4.11: Real Data with corrections vs. MC truth.

As seen, the deviation is approximately 20% at low p_{T} and around 1 GeV/c. This dip at the latter is due to the "geometric length cut". This cut requires that the track travel a minimum length within the TPC to be accepted. At higher transverse momenta, tracks can become nearly straight and may travel through the edges of two detectors. This effect is schematically illustrated in Figure 4.12.

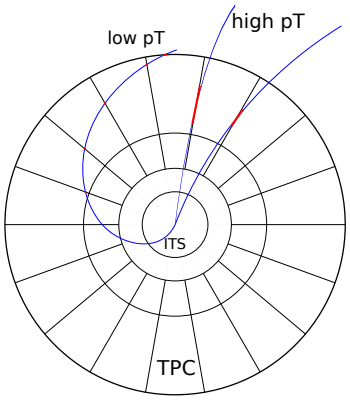

Figure 4.12: The red marks the areas, where the track cuts the edges of the detectors. It will not be detected.

4.6.0.2 Comparison of Pythia8 Simulations

Lastly, the p_{T} spectra of charged particles from Pythia8 are compared with Pythia8 data provided from the ALICE collaboration, as portrayed in Figure 4.13. These two data sets have the same settings, so a comparison could be made.

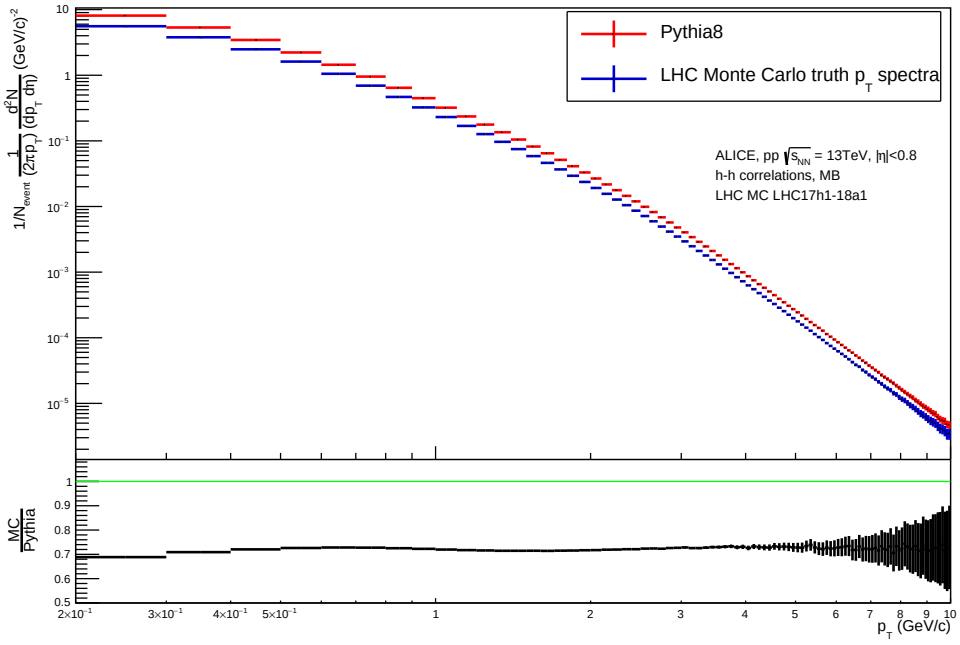

Figure 4.13: Charged particles: MC ALICE data vs MC Pythia data

The ratio of the spectra differs by 30%, consistently over the whole p_{T} range, meaning the data given from ALICE is lower at all momentum ranges.

4.7 Di-Hadron and Hadron-Gamma Correlation Method

For hadron experiments, jets are useful phenomena for detecting particles. Typically, predefined jet-finding algorithms are employed to reconstruct these jets. However, in collisions of larger nuclei like Au-Au or Pb-Pb, challenges arise due to the high particle multiplicity and the effects of the QGP, such as jet quenching.
Therefore, an alternative method known as the di-hadron correlation method is used. Instead of analyzing jets, the complete collision is taken into account. First, a particle from the collision is taken and used as a trigger. With this *trigger particle*, multiple other particles from the same collision are taken and associated with the trigger particle. These particles are called *associated particles*. The trigger particle has a higher transverse momentum, thus increasing the change originating from the initial colliding parton. It serves as the jet-inducing particle. The associated particle, with a lower transversal momentum, is then correlated to the trigger particle. A sketch illustrating this is shown in Figure 4.14.

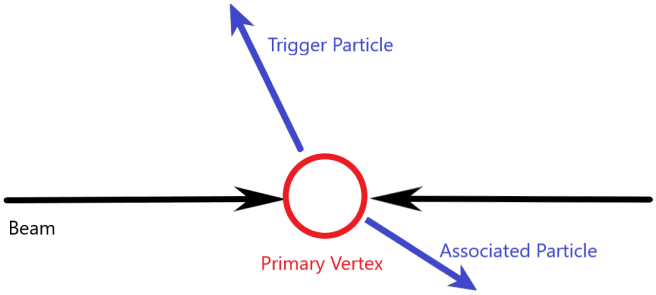

Figure 4.14: Idea behind correlation functions. Example with a large $\Delta\varphi$.

To obtain a correlation, the differences in the azimuthal angle φ and pseudorapidity η between the trigger and associated particle are calculated with:

$$\Delta\varphi = \varphi^{trigg} - \varphi^{assoc}, \tag{4.10}$$

$$\Delta\eta = \eta^{trigg} - \eta^{assoc}. \tag{4.11}$$

In one-dimensional histograms, the pseudorapidity differences can be seen in Figure 4.15 and the azimuthal angle in Figure 4.16:

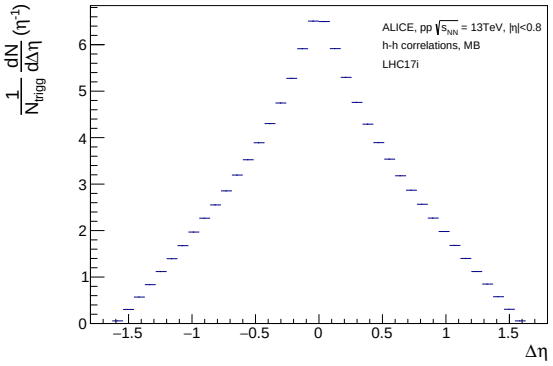

Figure 4.15: Difference between the pseudorapidity $\Delta\eta$ of the trigger and the associated particles.

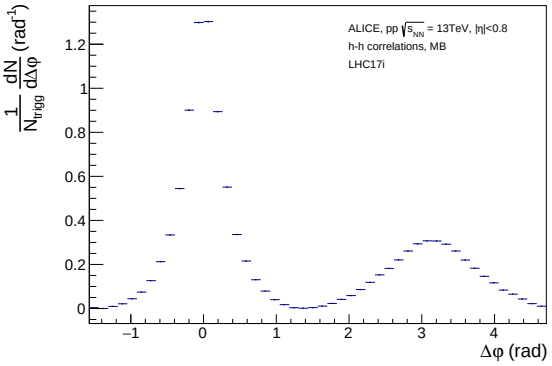

Figure 4.16: Difference between the azimuthal angle $\Delta\varphi$ of the trigger and the associated particles.

The characteristic triangular shape of the $\Delta\eta$ histogram results from the limitations of the TPC and ITS detectors in the η range. It is physically impossible to build a detector within the beam pipe, leading to the loss of a significant portion of the decay products. Figure 4.17 provides a sketch illustrating this problem.

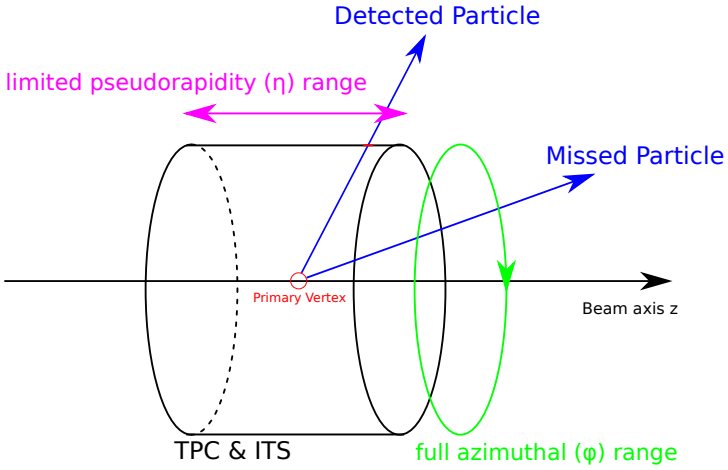

Figure 4.17: Limitations of the detectors in the pseudorapidity range.

For the $\Delta\varphi$ measurement, this problem exits to a lesser degree because the detectors cover the full φ range. Consequently, associated particles with η values outside the detector's coverage are not detected. While neutral associated particles cannot be directly detected, they are still indirectly covered in the hadron-gamma correlation.

A two-dimensional correlation function, Equation 4.12, can now be constructed with these two differences as:

$$C(\Delta\varphi, \Delta\eta) = \frac{1}{N_{trigg}} \frac{d^2N}{(d\Delta\varphi d\Delta\eta)} \tag{4.12}$$

with N_{trigg} as the number of trigger particles used for normalization.

In Figure 4.18 an example plot is shown. A peak at (0,0) is visible, known as the near-side peak. Here, the associated particle is closely aligned with the trigger particle, which can be interpreted as a pair of particles from the same jet. Another peak around π in the $\Delta\varphi$-plane exits and is called an away-side peak. This peak arises due to the conservation of momentum in the jets, resulting in the appearance of two jets back-to-back. It is smeared in the $\Delta\eta$-plane because the associated particle can travel in any longitudinal direction, including longitudinal ranges outside of the detector's coverage. This does not occur with the trigger particle, by definition.

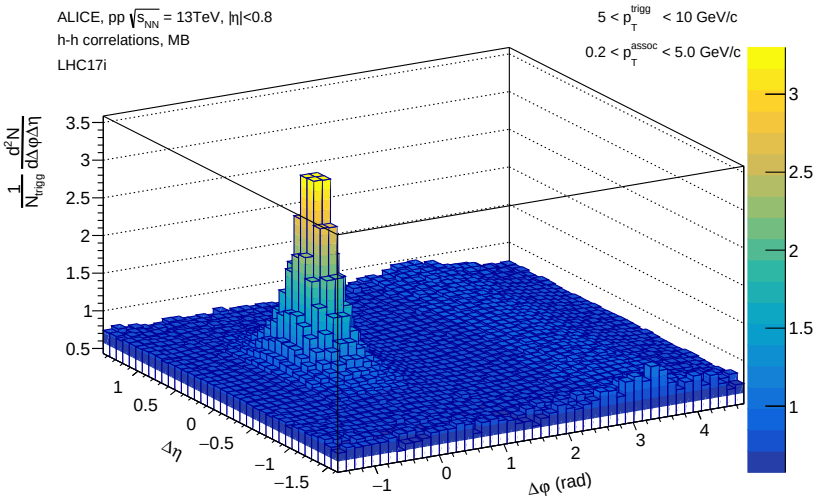

Figure 4.18: An example of a correlation function of two hadrons.

Yields $\Delta\varphi$ projection can be extracted from this correlation function. With these, the *per-trigger associated particle yields* are calculated for the near-side and away-side peak. These are defined as:

$$Y_J^{\Delta\varphi} = \int_{\Delta\varphi 1}^{\Delta\varphi 2} \frac{dN}{d\Delta\varphi} d\Delta\varphi. \tag{4.13}$$

$\Delta\varphi_1$ marks the starting point of a peak, while $\Delta\varphi_2$ the end point. An integral is calculated within this region with the function **IntegralAndError(BinOf$\Delta\varphi_1$, BinOf$\Delta\varphi_2$, err, "width")**. The per-trigger associated particle yields are chosen to gain a detailed view of the angular correlations of the trigger and associated particles. It should be noted that the integral is taken after the subtraction of the background and after the normalization on the number of trigger particles.

5 Results

This chapter presents the correlation functions for hadron-hadron, hadron-gamma and MC hadron-gamma, projections in $\Delta\varphi$ and $\Delta\eta$, the yields, and origins of the particles.

5.1 Two-Dimensional Correlation Functions

The two-particle correlation functions are presented in this section, analyzed across different trigger-p_{T} and associated-p_{T} intervals. In the following figures, the two columns represent different trigger p_{T} intervals; the left column covers 5 GeV/c to 7.5 GeV/c, while the right column covers 7.5 GeV/c to 10 GeV/c. Only two trigger p_{T} intervals are chosen due to the rarity of high-p_{T} events to increase the statistics.

Different intervals are chosen instead of the whole range because it enables a detailed view of how particles are produced at different transverse momenta. For the associated p_{T}, five intervals are chosen, represented by the five rows. Since associated particles have a lower p_{T} than trigger particles by definition, a greater number of associated particles are produced.

Hadron-Hadron in Data For the charged hadron-hadron correlation function, the intervals are shown in Figure 5.1. A general observation is that the near-side peaks become narrower and smaller with, both with increasing $p_{\mathrm{T}}^{\mathrm{trigg}}$ and $p_{\mathrm{T}}^{\mathrm{assoc}}$. This phenomenon has multiple reasons.

Firstly, an increase in the transverse momentum of the trigger particle causes a larger relativistic Lorentz boost for the associated particles in the direction of the jet (in the reference frame of the laboratory), causing them to be emitted at smaller angles relative to the trigger. Thus, it leads to a more collimated jet and thus narrower peaks in the correlation function.

Secondly, the strong coupling constant α_S decreases (approaching asymptotic freedom) for larger p_{T} of the trigger particle. This leads to less wide-angle gluon radiation and fewer instances of parton splitting, as described by the fragmentation function. As a result, the probability of producing new particles, particularly soft radiation (low-p_{T} particles), is reduced due to the limited phase space for such emissions. Most of these low-p_{T} particles contribute to the background. Therefore, the relative amount of associated particles with large p_{T} increases, and they are also more collimated around the trigger particle. Thus, the peaks are getting smaller in height because fewer particles are produced overall in that energy range. But this phenomenon is not consistent across all ranges. When the transverse momentum of the associated particle increases, the decrease of the near-side peak becomes smaller.

As an example, at the range of $5 \leq p_{\mathrm{T}}^{\mathrm{trigg}} \leq 7.5\,\mathrm{GeV/c}$, the near-side peak at the range of $0.2 \leq p_{\mathrm{T}}^{\mathrm{assoc}} \leq 1.0\,\mathrm{GeV/c}$ is approximately 30 % larger than the near-side peak at the range of $7.5 \leq p_{\mathrm{T}}^{\mathrm{trigg}} \leq 10\,\mathrm{GeV/c}$.
At high $p_{\mathrm{T}}^{\mathrm{assoc}}$ ranges, this effect reverses. For the range of $4 \leq p_{\mathrm{T}}^{\mathrm{assoc}} \leq 5\,\mathrm{GeV/c}$, the near-side peak of the range of $5 \leq p_{\mathrm{T}}^{\mathrm{trigg}} \leq 7.5\,\mathrm{GeV/c}$ is now approximately 30 % lower than at the range of $7.5 \leq p_{\mathrm{T}}^{\mathrm{trigg}} \leq 10\,\mathrm{GeV/c}$.

If the transverse momentum of the trigger particle is large, which indicates an origin from a high-p_{T} parton and therefore a high-p_{T} jet, more associated particles with high-p_{T} can be produced. These high p_{T} associated particles have therefore a greater chance of originating from the jet.

The away-side peaks become smaller and narrower, with an increasing in both p_{T}. The difference in the p_{T} interval of the associated particle has a greater impact on this effect than the difference in the p_{T} interval of the trigger particle. Due to the small visible effects, the per-trigger yields are of higher interest. The reduced height of the away-side can be explained by the fact that the particle needs to balance the p_{T} of the near-side peak in azimuthal direction. Therefore, it can radiate in all longitudinal directions, (i.e., with any η), resulting in a broad η-distribution. Additionally, due to the limitations of the detector in the pseudorapidity range, not all associated particles can be detected. These two factors lead to a lower height of the away-side peak.

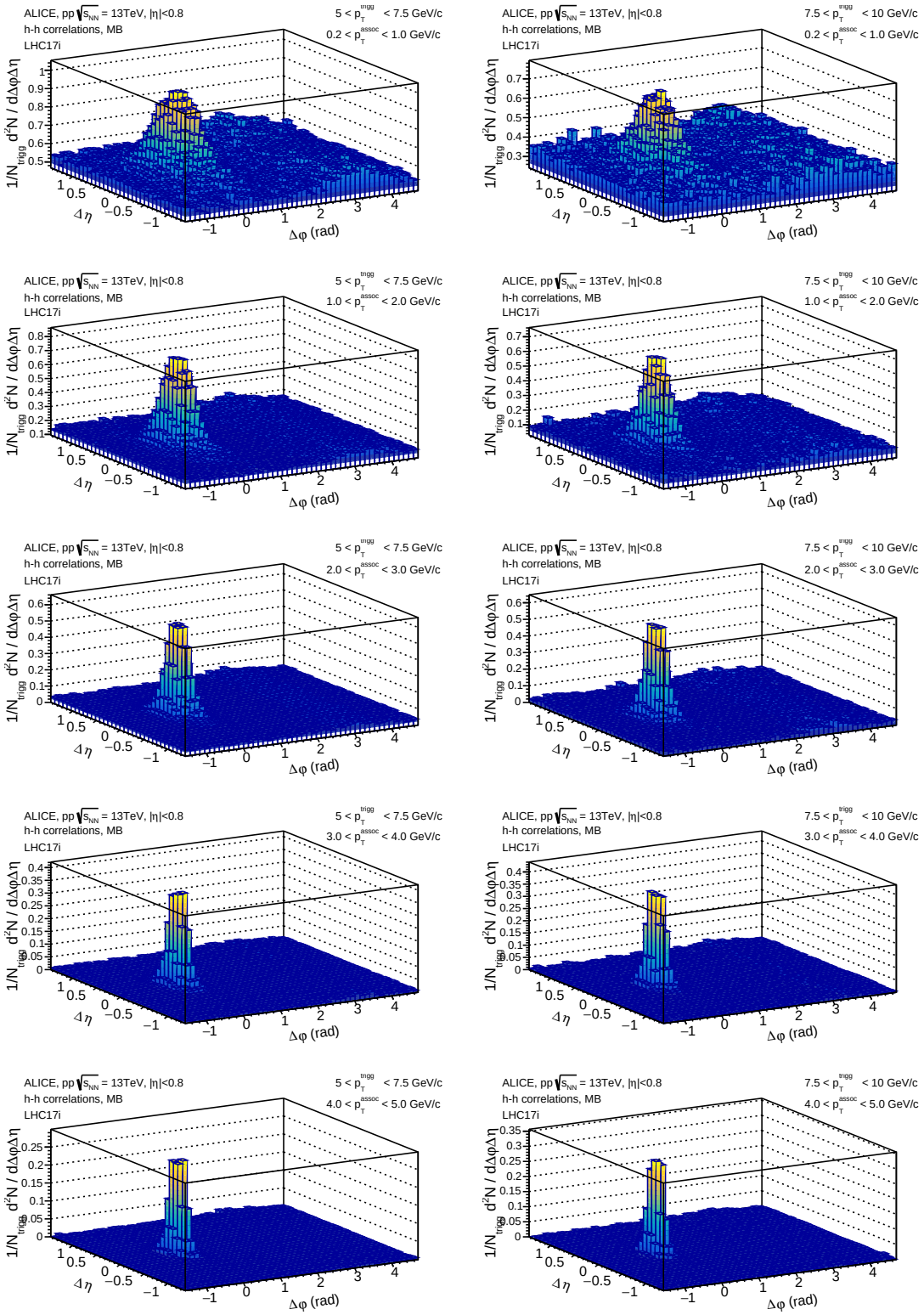

Figure 5.1: Two-dimensional hadron-hadron correlation functions for two different $p_{\mathrm{T}}^{\mathrm{trigg}}$ intervals in the columns and five different $p_{\mathrm{T}}^{\mathrm{assoc}}$ intervals in the rows.

Hadron-Gamma in Data Correlations between hadrons and photons (Figure 5.2) show results that are similar to those of hadron-hadron correlations. However, the away-side peak is notably smaller, while the near-side peak is narrower. Additionally, at lower momenta, the near-side peak does not narrow as much as in the hadron-hadron case. The peaks are also consistently taller at the larger $p_{\mathrm{T}}^{\mathrm{trigg}}$ interval. This indicates the fact that the number of either produced or detected associated particles decreases in proportion to the number of trigger particles.
These effects arise from the fact that photons do not fragment and, therefore, do not hadronize. This leads to fewer associated particles being produced, resulting in a smaller peak. The particles that are produced tend to be more collimated around the jet-inducing trigger particle, creating a narrower near-side peak. Consequently, each photon carries a large part of the initial transverse momentum.

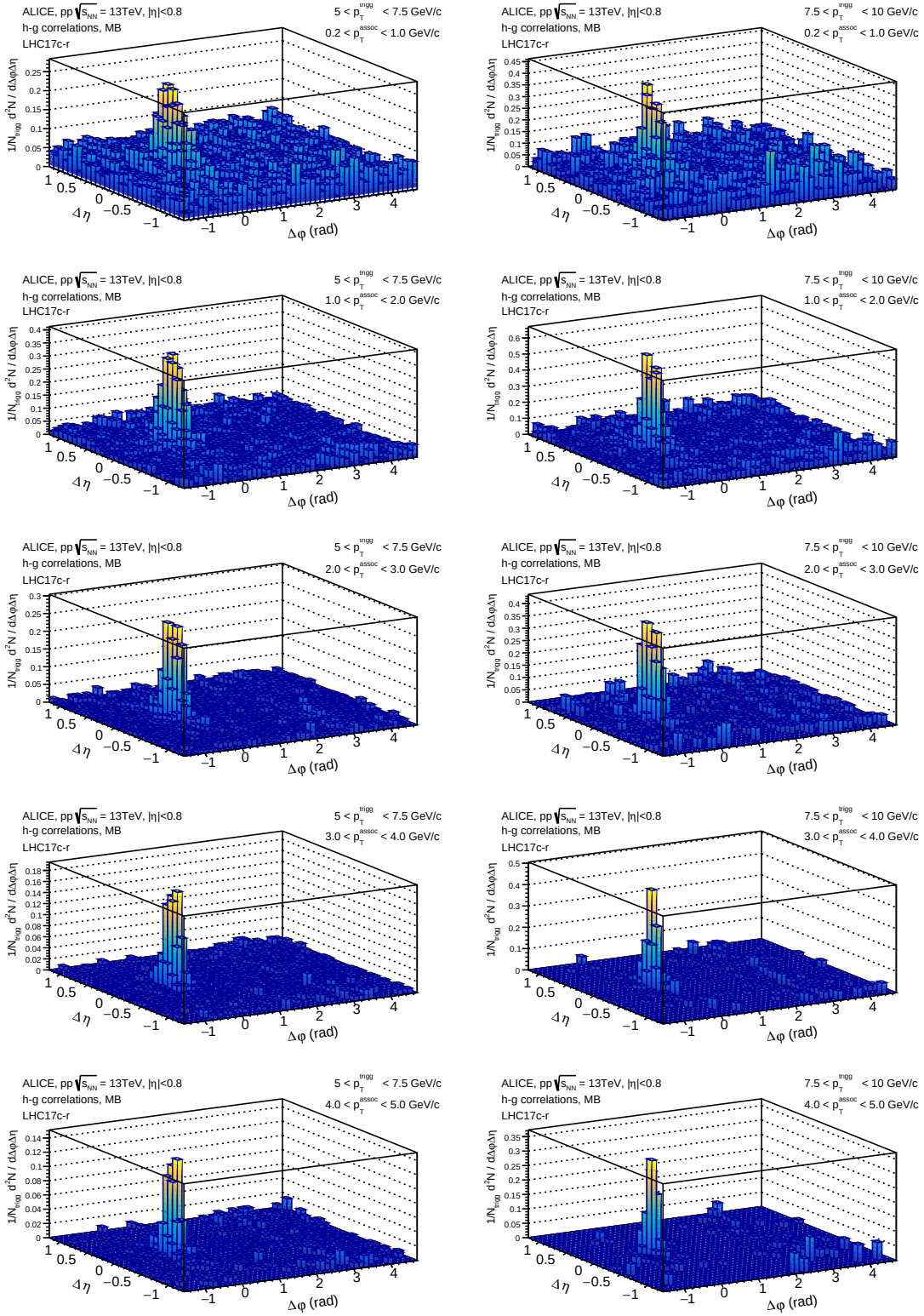

Figure 5.2: Two-dimensional hadron-gamma correlation functions for two different $p_{\mathrm{T}}^{\mathrm{trigg}}$ intervals in the columns and five different $p_{\mathrm{T}}^{\mathrm{assoc}}$ intervals in the rows.

Hadron-Gamma in Monte Carlo Multiple correlation functions for simulated data are also obtained, as seen in Figure 5.3. Here, the associated particle is again a photon, but these photons originate only from the chosen types of mother particles. Also, no intervals for the transverse momenta are taken, instead the whole available momentum range is taken for each particle. With this, hadron-gamma correlations are made, where the mother particle of the photons can be chosen. Initially, all charged particles are taken into account for the mother particle of the photon, resulting in a similar shape to the correlation functions from the real data. By further differentiating the mother particles into π^0 and η, similar shapes can be observed. For other mother particles of the photons, like e^-e^+, Σ^0 and γ, the statistics are too low to see a pronounced near-side peak. The potential peaks will be discussed in the following projections for $\Delta\varphi$ and $\Delta\eta$. The measured data for photon mother particles will be discussed in Section 5.5. It is important to note that these photons are not necessarily mother particles in the sense of decaying into photons. In Pythia8, when momentum is transferred between particles, it may classify a particle involved in the interaction as a mother particle. For example, if a photon scatters, the photon may be labeled as the mother particle in the subsequent part of the interaction chain.

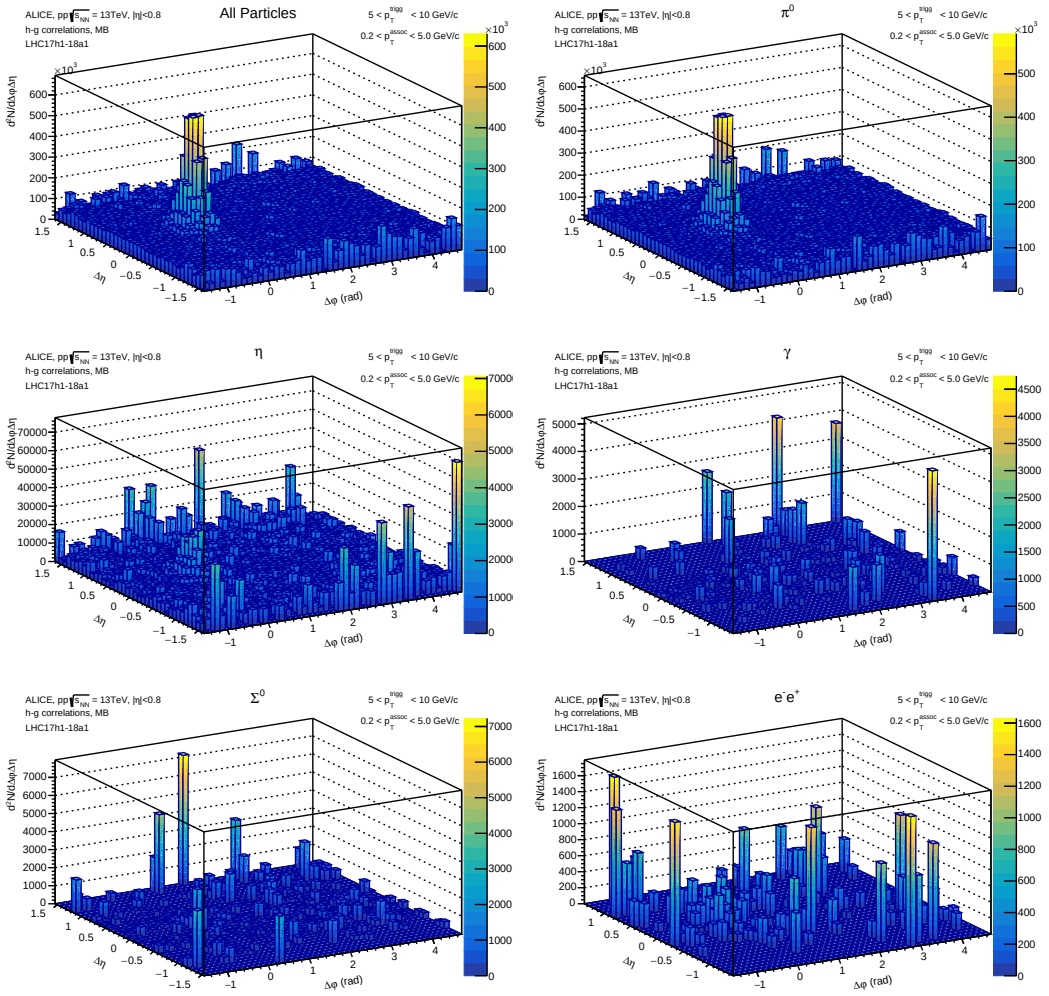

Figure 5.3: Two-dimensional hadron-gamma correlation functions for different trigger particle. In contrast to the previously two correlation, here the full p_T are taken.

5.2 $\Delta\eta$ Projections

Hadron-Hadron in Data In these projections in $\Delta\eta$ (Figure 5.4), the observed effects from above are visible again. The larger the p_{T} of the trigger and associated particles are, the narrower and smaller the peaks get.

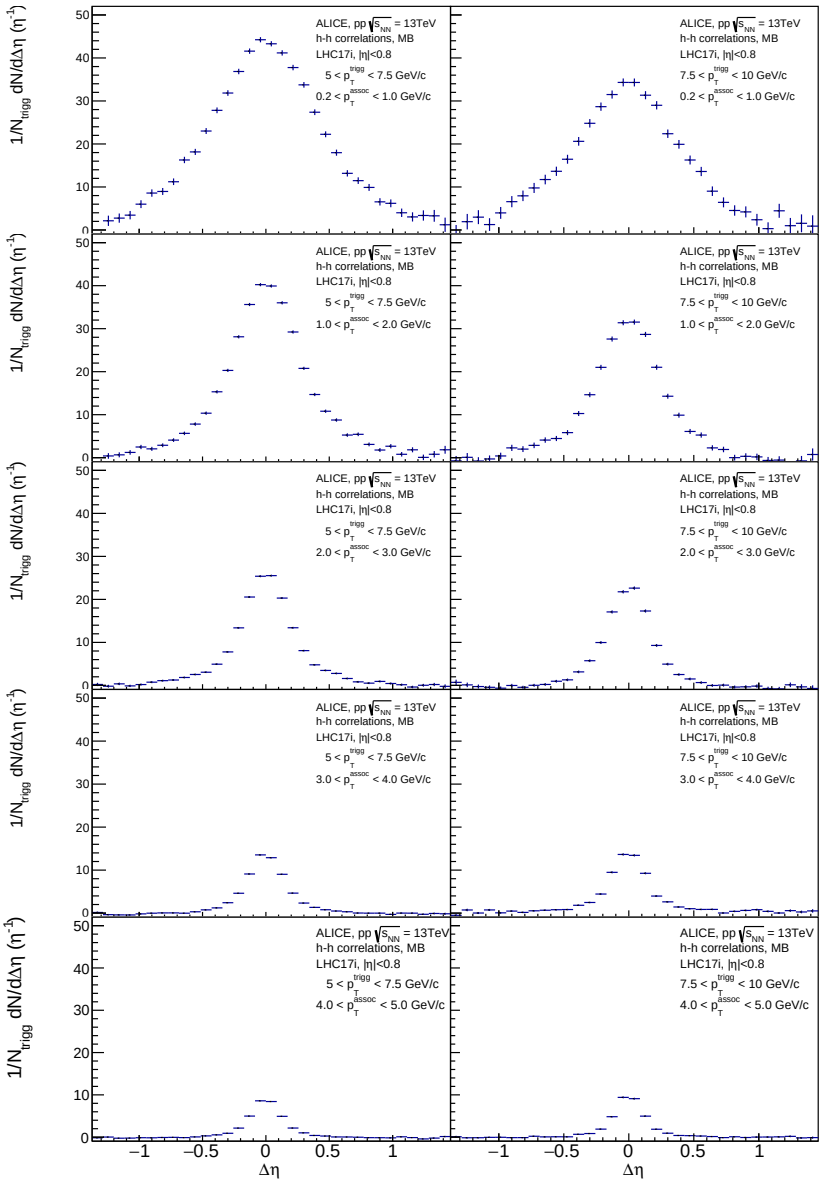

Figure 5.4: $\Delta\eta$ projections of hadron-hadron correlation functions at different intervals for $p_{\mathrm{T}}^{\mathrm{trigg}}$ and $p_{\mathrm{T}}^{\mathrm{assoc}}$.

A reduction in multiplicity can be seen, primarily affected by the different $p_{\mathrm{T}}^{\mathrm{assoc}}$ values. There is an approximate factor of five in the difference between the peak of the highest momentum interval and the lowest.

Hadron-Gamma in Data While a high transverse momentum for the associated particles still leads to a lower peak with hadron-gamma (Figure 5.5) that does not appear to be the case for the higher transverse momentum of the trigger particle. Here, the larger momentum leads to a consistently larger peak, as explained above.

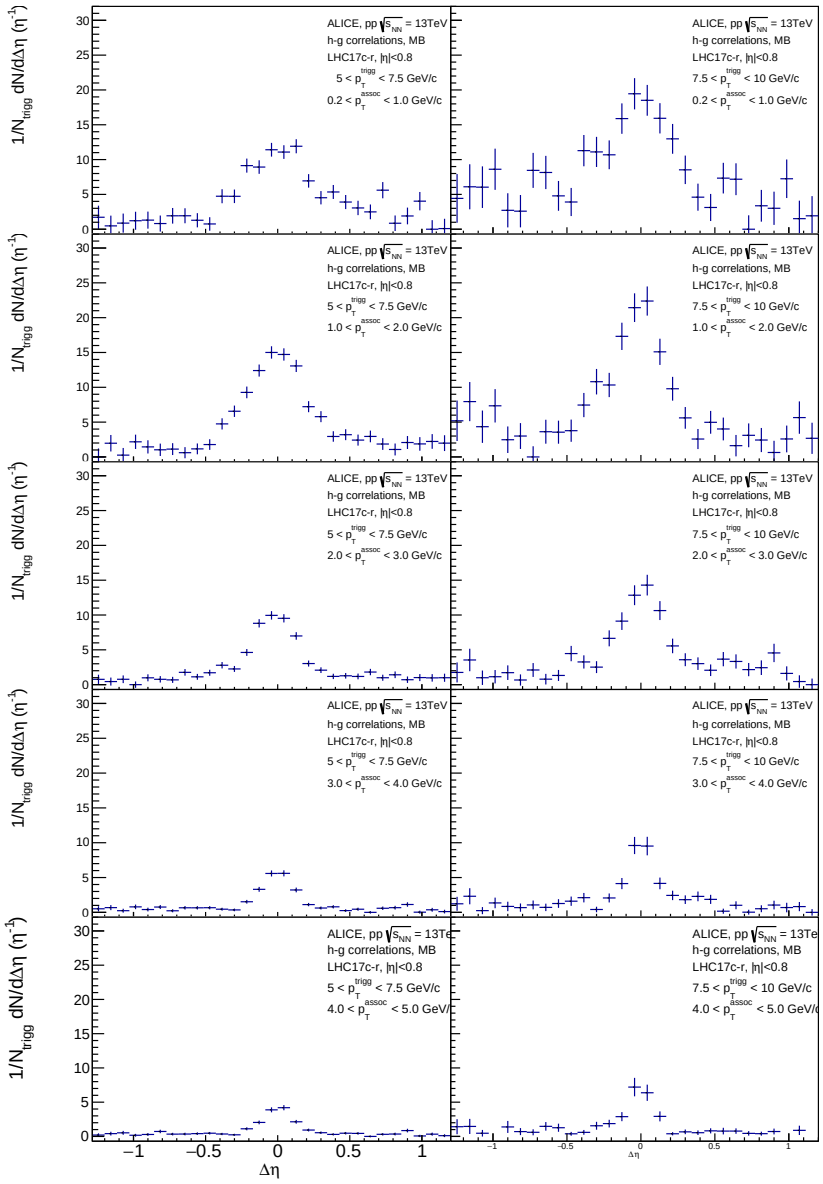

Figure 5.5: $\Delta\eta$ projections of hadron-gamma correlation functions at different intervals for $p_{\mathrm{T}}^{\mathrm{trigg}}$ and $p_{\mathrm{T}}^{\mathrm{assoc}}$.

Hadron-Gamma in Monte Carlo At the $\Delta\eta$ projections for the Monte Carlo data, seen in Figure 5.6, the peaks are clearly visible for all charged particles, π^0, and η as mothers for the photons. While the Σ^0 and the e^-e^+ pairs have low statistics, a peak around 0 is still recognizable. Interestingly, the photons do not have a peak around 0, it appears as if they have a rather flat distribution with increasing statistical fluctuation at the outer regions at ± 1.5, due to the low statistics.

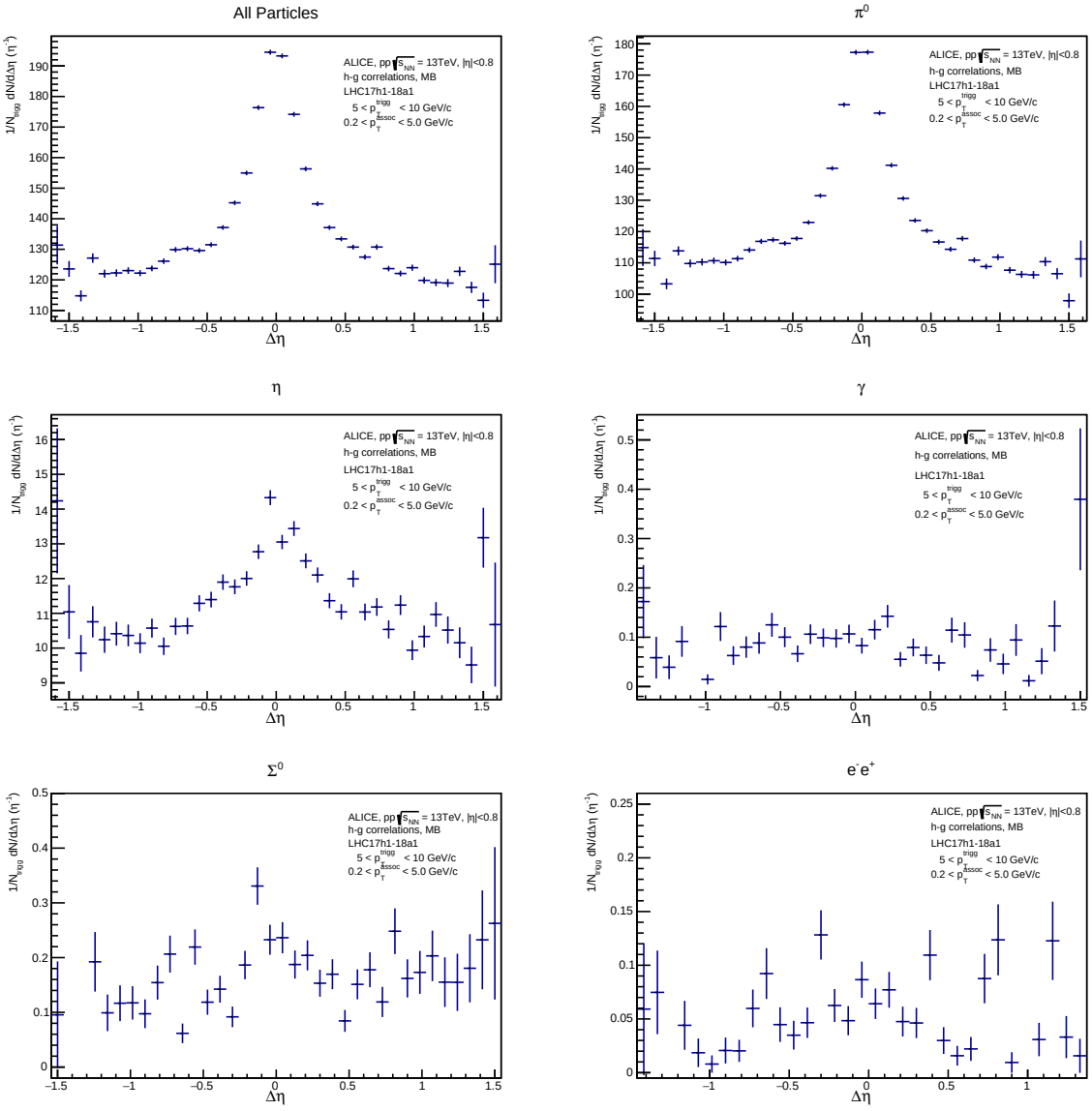

Figure 5.6: $\Delta\eta$ projections of hadron-gamma correlation functions for different parent particles of the photons.

5.3 $\Delta\varphi$ Projections

The $\Delta\varphi$ projections are fitted with a Gaussian function, from which a *full width at half maximum (FWHM)* is determined. This provides an additional comparable measure. The underlying event is subtracted before the fitting, as soft processes are not of interest in this analysis. Following this, the peaks are integrated to determine the Yields.

The double Gauss fit

$$G(x) = A_1 \cdot \exp\left[-\frac{1}{2}\left(\frac{x-\mu_1}{\sigma_1}\right)^2\right] + A_2 \cdot \exp\left[-\frac{1}{2}\left(\frac{x-\mu_2}{\sigma_2}\right)^2\right], \tag{5.1}$$

is used. Here, the first term with the exponent stands for the near-side peak, and the other term stands for the away-side peak. Therefore, A_1 is the parameter for the height of the near-side peak, μ_1 is the mean (or peak position), which is ideally at 0 and σ_1 is the standard deviation, or width, of the Gaussian distribution. Analogously for the away-side peak, A_2 is the amplitude, μ_2 is the peak position, which is expected to be around π and σ_2 the standard deviation.

Hadron-Hadron in Data For the $\Delta\varphi$ projections of hadron-hadron correlations (Figure 5.7), the away-side peak is noticeably distinct. Additionally, in higher p_{T} intervals, the away-side peak decreases in size while maintaining the same width. In contrast, the near-side peak becomes both smaller and narrower. For smaller transverse momenta of the associated particles, both peaks become smaller, but it appears that only the near-side peaks decrease in width, while the width of the peak on the away-side remains unchanged. This phenomenon will be further investigated using the yield and the FWHM analyzes.

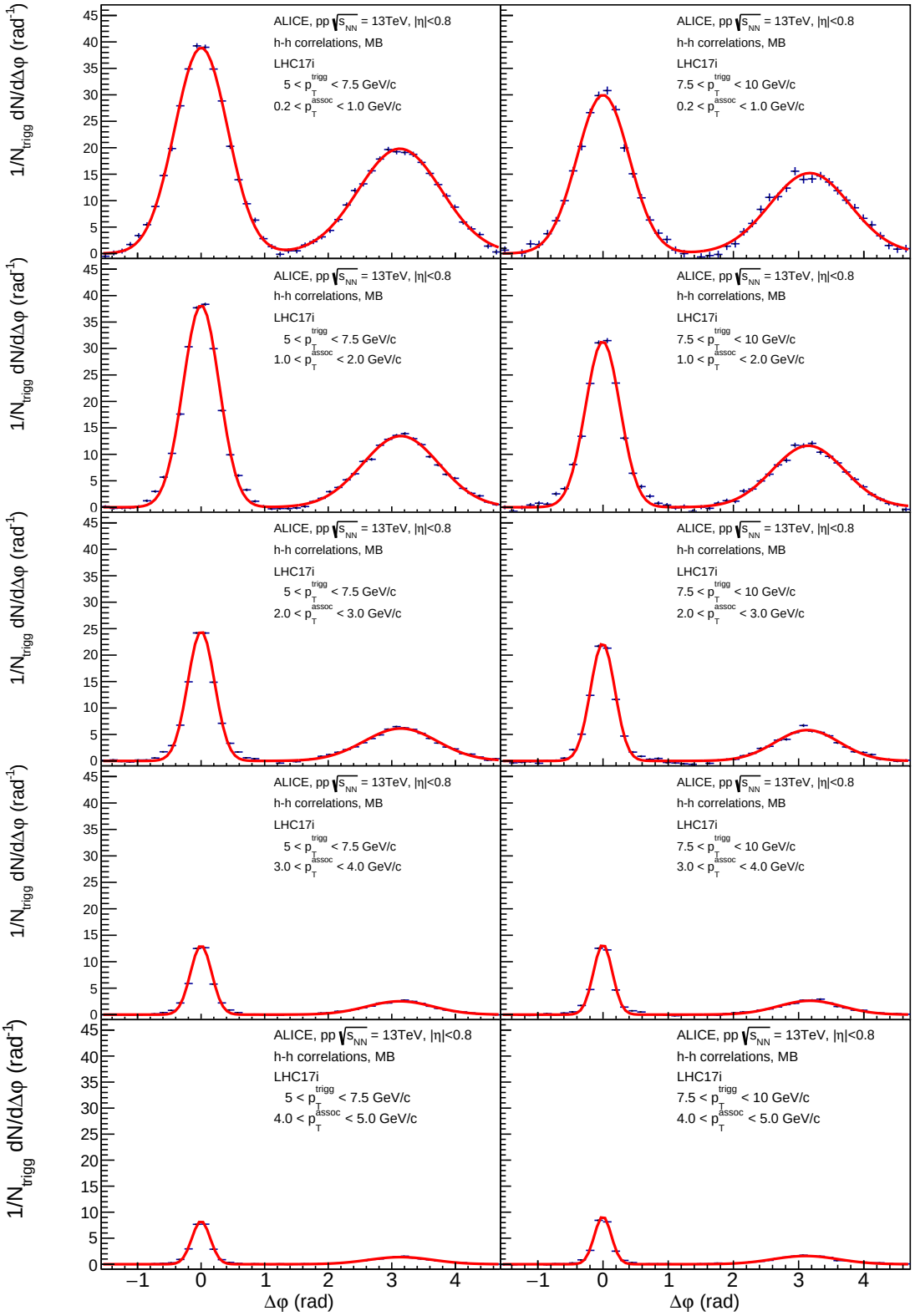

Figure 5.7: $\Delta\varphi$ projections of hadron-hadron correlation functions for different intervals for $p_{\mathrm{T}}^{\mathrm{trigg}}$ and $p_{\mathrm{T}}^{\mathrm{assoc}}$.

Hadron-Gamma in Data For hadron-gamma correlations, shown in Figure 5.8, the away-side peak is significantly smaller and broader. At the highest p_{T} interval in both the trigger and associated, it nearly vanishes. Also, for higher p_{T} intervals, the near-side peak becomes taller, resembling the results of the $\Delta\eta$ projections. The away-side peaks are visible in these $\Delta\varphi$ projections, but at the largest momentum interval, they become diminishingly small. A further study will therefore be undertaken later with the yields.

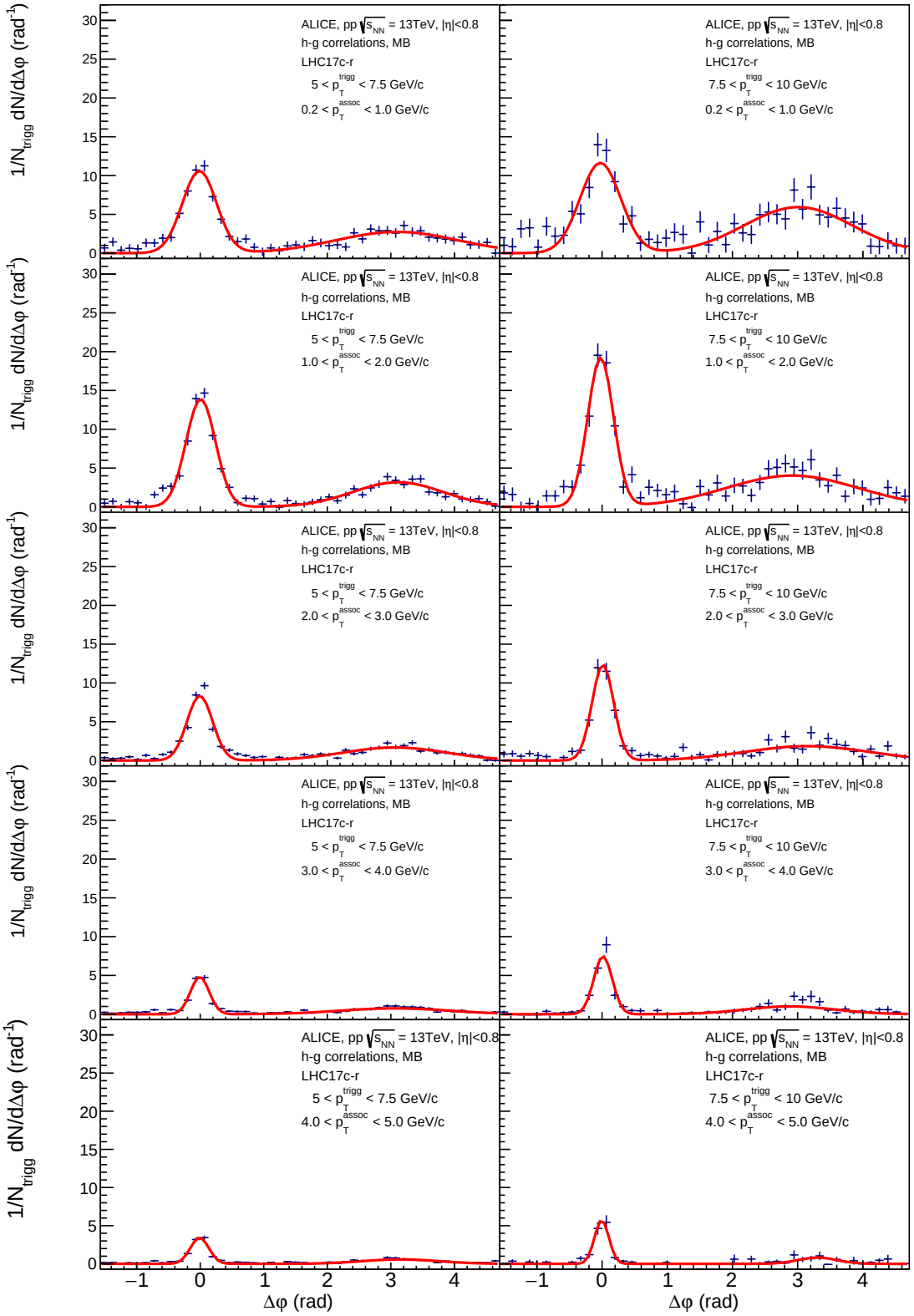

Figure 5.8: $\Delta\varphi$ projections of hadron-gamma correlation functions for different intervals for $p_{\mathrm{T}}^{\mathrm{trigg}}$ and $p_{\mathrm{T}}^{\mathrm{assoc}}$.

Hadron-Gamma in Monte Carlo Analogous to the results from the $\Delta\eta$ projections (Figure 5.9), the $\Delta\varphi$ projections from hadron-gamma correlation functions with all charged particles, π^0, and η as mothers for the photons have clear peaks. For the cases with all charged particle and pion, the near-side peak at $\varphi = 0$ is the most pronounced one, while the away-side peak is relatively small. For the η as mother, the near-side peak is only around 15 % higher, meaning the peaks are significantly closer in height to each other. In the other three cases with the γ-particle, Σ^0, and the e^-e^+ as mother particle, no correlations can be observed. This is most likely due to the low statistics.

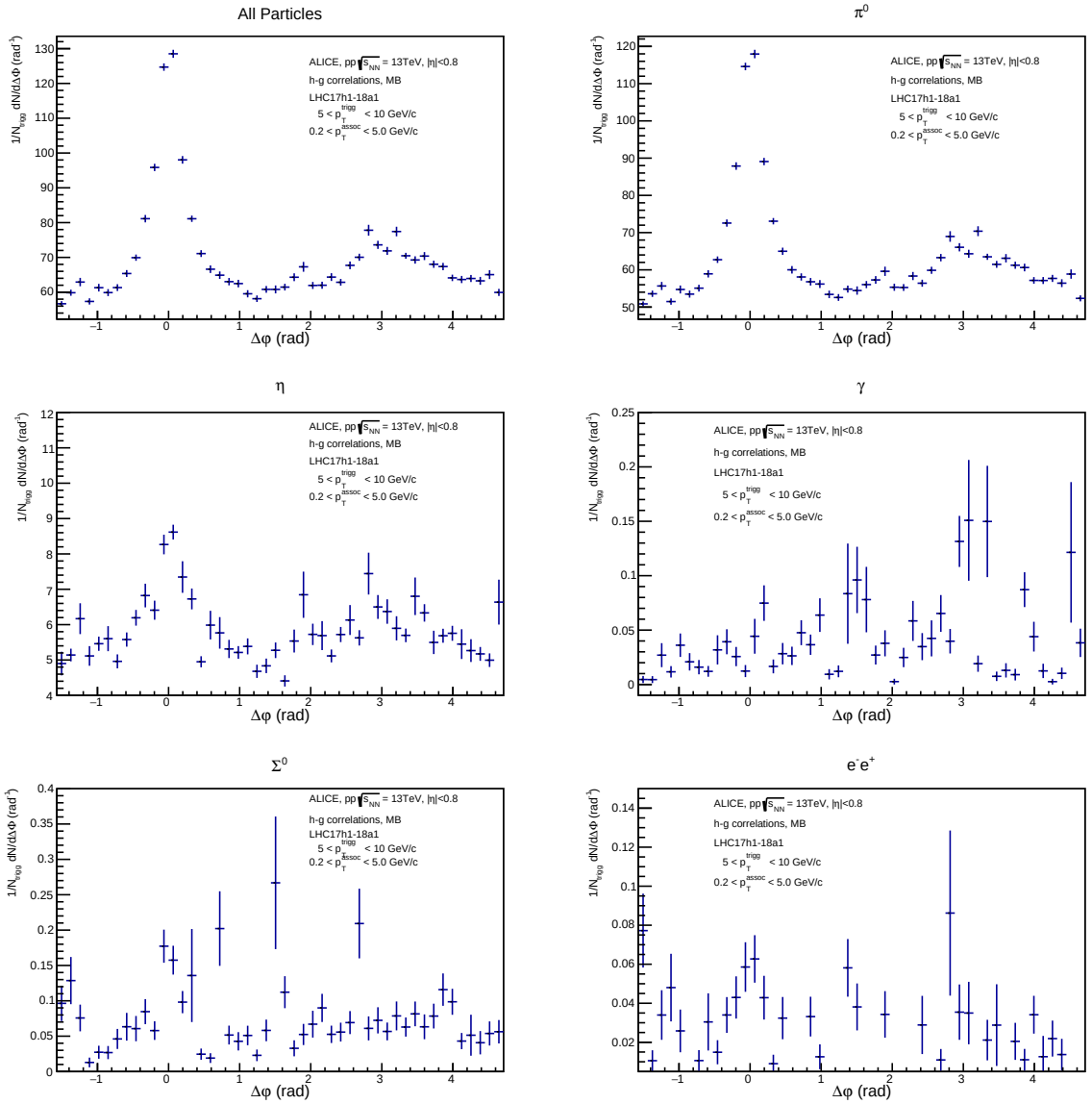

Figure 5.9: $\Delta\varphi$ projections of hadron-gamma from Monte Carlo correlation functions for different particles.

5.3.1 Analysis of FWHM

Hadron-Hadron in Data The Gauss fits, seen in Figure 5.10, show that the away-side peaks are broader than the near-side ones. They also get noticeably smaller as the $p_{\mathrm{T}}^{\mathrm{assoc}}$ increases. Additionally, the gap between the full width at half maximum (FWHM) between the $p_{\mathrm{T}}^{\mathrm{trigg}}$ increases up to a $p_{\mathrm{T}}^{\mathrm{assoc}}$ of 2.5 GeV/c and then decreases strongly. At the largest $p_{\mathrm{T}}^{\mathrm{assoc}}$ at 4.5 GeV/c, the two FWHM are very close to each other. Overall, the FWHM of the away-side peaks decreases for the $5 < p_{\mathrm{T}}^{\mathrm{trigg}} < 7.5$ GeV/c intervals (red), while for the $7.5 < p_{\mathrm{T}}^{\mathrm{trigg}} < 10$ GeV/c intervals (blue), they only decrease up to $p_{\mathrm{T}}^{\mathrm{assoc}}$ of 2.5 GeV/c. After that, they stagnate.

In contrast, the near-side becomes significantly narrower at high $p_{\mathrm{T}}^{\mathrm{assoc}}$, resulting in a smaller FWHM. The gap between the two $p_{\mathrm{T}}^{\mathrm{trigg}}$ intervals shows a similar trend of diverging up to 2.5 GeV/c and converging, but the difference is smaller.

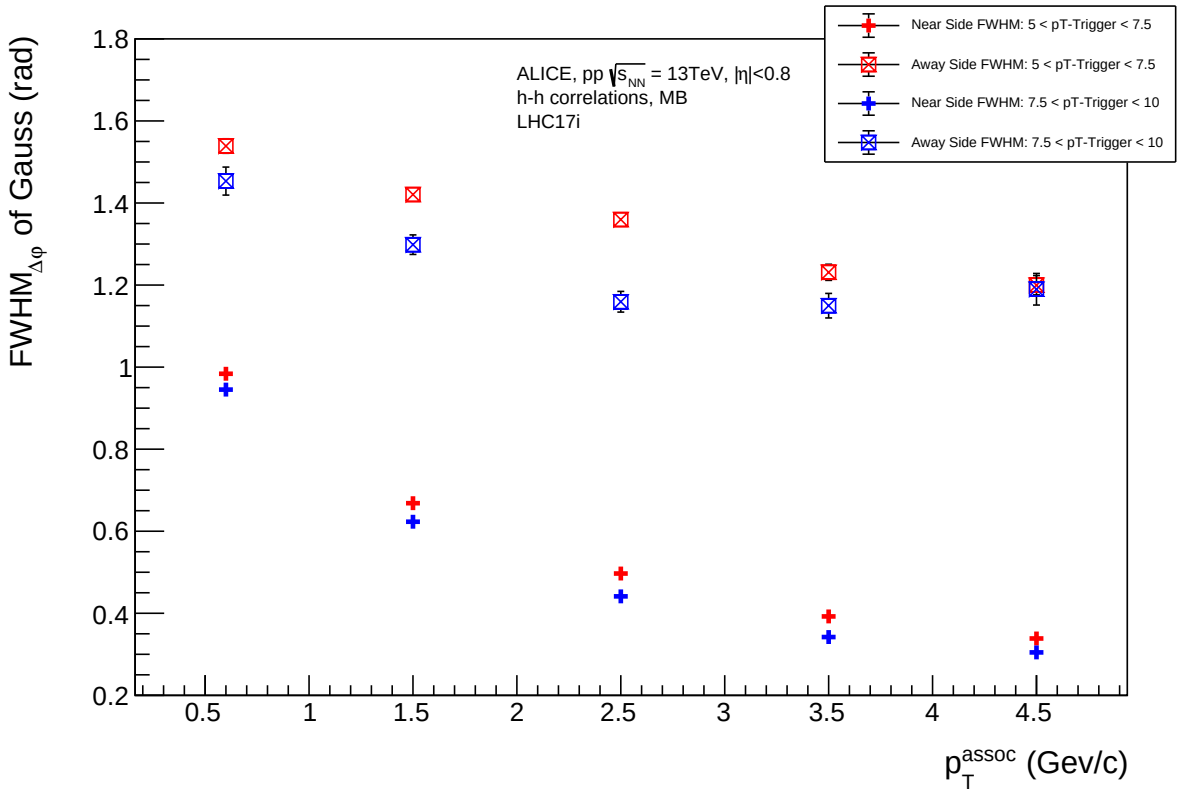

Figure 5.10: FWHMs of the double Gaussian fits for hadron-hadron $\Delta\varphi$ projections at different p_{T} for the trigger and associated particles.

Hadron-Gamma in Data For the hadron-gamma correlations (Figure 5.11), the $5 < p_{\mathrm{T}}^{\mathrm{trigg}} < 7.5\,\mathrm{GeV/c}$ (red) FWHMs of the away-side peaks have a cubic-like pattern over the $p_{\mathrm{T}}^{\mathrm{assoc}}$. First, the width of the peak decreases up to a $p_{\mathrm{T}}^{\mathrm{assoc}}$ value of $1.5\,\mathrm{GeV/c}$, then rises up to $3.5\,\mathrm{GeV/c}$ and then falls again. In contrast, for the $7.5 < p_{\mathrm{T}}^{\mathrm{trigg}} < 10\,\mathrm{GeV/c}$ interval (blue), the FWHMs increase, reaching a maximum at $1.5\,\mathrm{GeV/c}$ before falling. The large uncertainties should not be dismissed. However, these do not negate the observed cubic pattern of the FWHMs of the $5 < p_{\mathrm{T}}^{\mathrm{trigg}} < 7.5\,\mathrm{GeV/c}$ interval.
The FWHMs of the near-side peaks of both $p_{\mathrm{T}}^{\mathrm{trigg}}$ intervals decrease up until a $p_{\mathrm{T}}^{\mathrm{assoc}}$ of $1.5\,\mathrm{GeV/c}$ and then stagnate. It is to be noted that at the lowest $p_{\mathrm{T}}^{\mathrm{assoc}}$, the FWHMs of the $7.5 < p_{\mathrm{T}}^{\mathrm{trigg}} < 10\,\mathrm{GeV/c}$ is smaller than the $5 < p_{\mathrm{T}}^{\mathrm{trigg}} < 7.5\,\mathrm{GeV/c}$, but this invert at larger $p_{\mathrm{T}}^{\mathrm{assoc}}$.

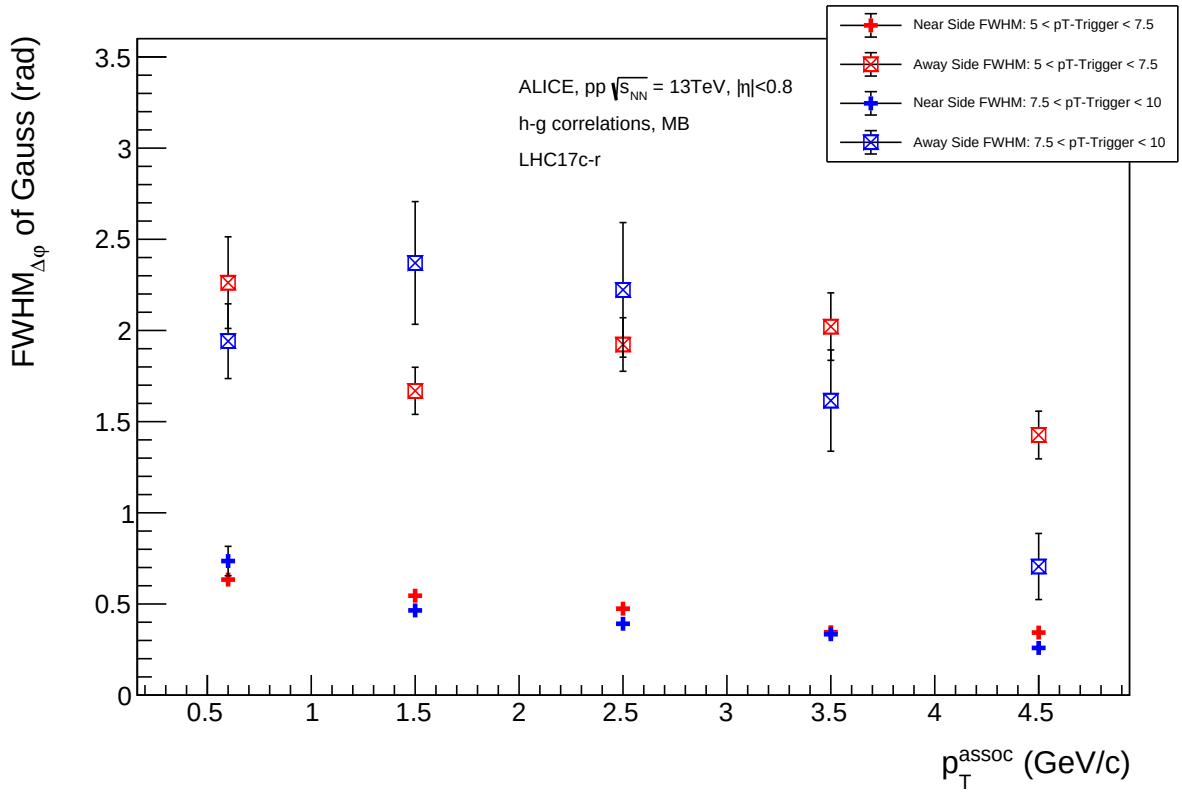

Figure 5.11: FWHMs of the double Gaussian fits for hadron-gamma $\Delta\varphi$ projections at different p_{T} for the trigger and associated particles.

Note that an FWHM from the away-side peak at $p_{\mathrm{T}}^{\mathrm{assoc}}$ of $4.5\,\mathrm{GeV/c}$ and $7.5 < p_{\mathrm{T}}^{\mathrm{trigg}} < 10\,\mathrm{GeV/c}$ cannot be extracted, due to missing statistic. Also, at $4.5\,\mathrm{GeV/c}$, the FWHM values of the near-side peaks overlap.

5.4 Per-Trigger Yields as a Function of p_T^{assoc} with Different p_T^{trigg}-Intervals

The per-trigger yields are characteristic measurements for the multiplicity of correlations. They are the integrated near-side and away-side peaks of the $\Delta\varphi$ and show how many associated particles are produced relative to the trigger particle. The yield of the underlying event, which is subtracted as mentioned in Section 5.3, is also analyzed.

Hadron-Hadron in Data In Figure 5.12, it is evident that the yields and underlying events decrease as p_T^{assoc} increases. Consequently, a large number of associated particles with low transverse momentum are found, particularly at the near-side peak. Interestingly, the differences between the yields for different p_T^{trigg} intervals (red for the lower momentum interval, blue for the higher interval) diminish as the p_T^{assoc} increases. At low p_T^{assoc}, the yields from the low p_T^{trigg} interval are approximately 33 % larger than those from the high p_T^{trigg} interval. This difference completely vanishes for higher p_T^{assoc}, resulting in yields from the near-side and away-side peaks of equal size. The underlying event of both p_T^{trigg} intervals decreases with increasing p_T^{assoc}. At p_T^{assoc} of 4.5 GeV/c, the underlying event of the larger p_T^{trigg} interval is around 30 % lower than at p_T^{assoc} of 0.5 GeV/c.

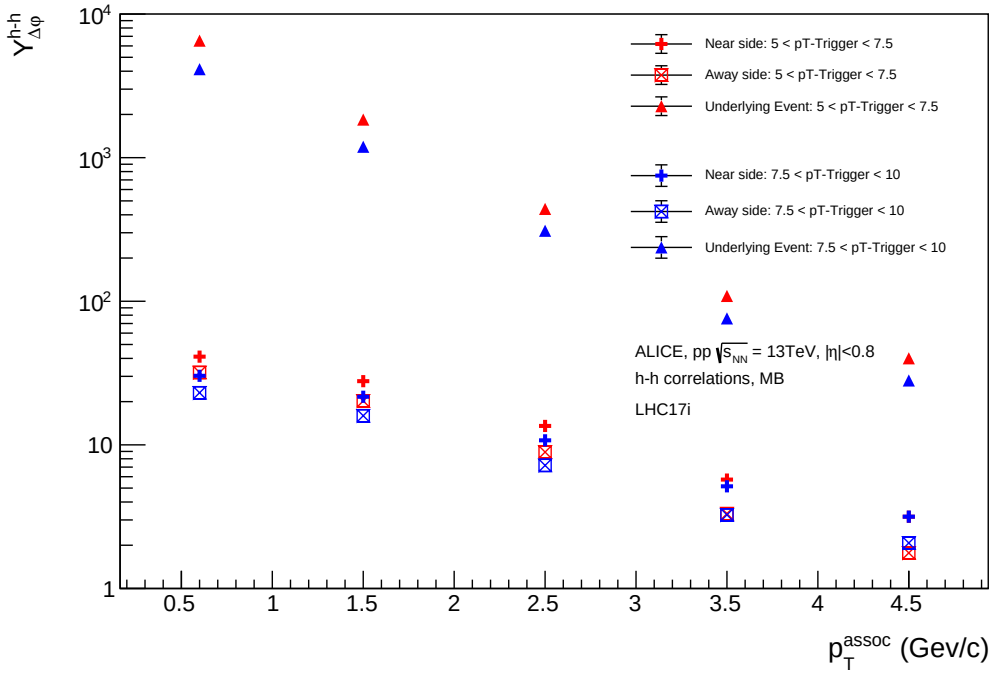

Figure 5.12: Yield for hadron-hadron as a function of p_T^{assoc} and p_T^{trigg}.

This emphasizes the fact that fewer high-p_T particles get produced. It is to note that at a p_T^{assoc} of 4.5 GeV/c, the yields from the near-side peaks from both p_T^{trigg} intervals overlap, and a similar overlap occurs for the away-side peaks at 3.5 GeV/c.

Hadron-Gamma in Data A similar trend is observed in the hadron-gamma correlations in Figure 5.13, with an exception at the lowest $p_{\mathrm{T}}^{\mathrm{assoc}}$ interval. In this case, the yields are lower and increase to the higher $p_{\mathrm{T}}^{\mathrm{assoc}}$ interval of 1.5 GeV/c. From here on, the yields decrease, as in the case of the hadron-hadron correlations. Overall, the production of particles in the hadron-gamma correlations is approximately three times lower compared to the hadron-hadron yields.

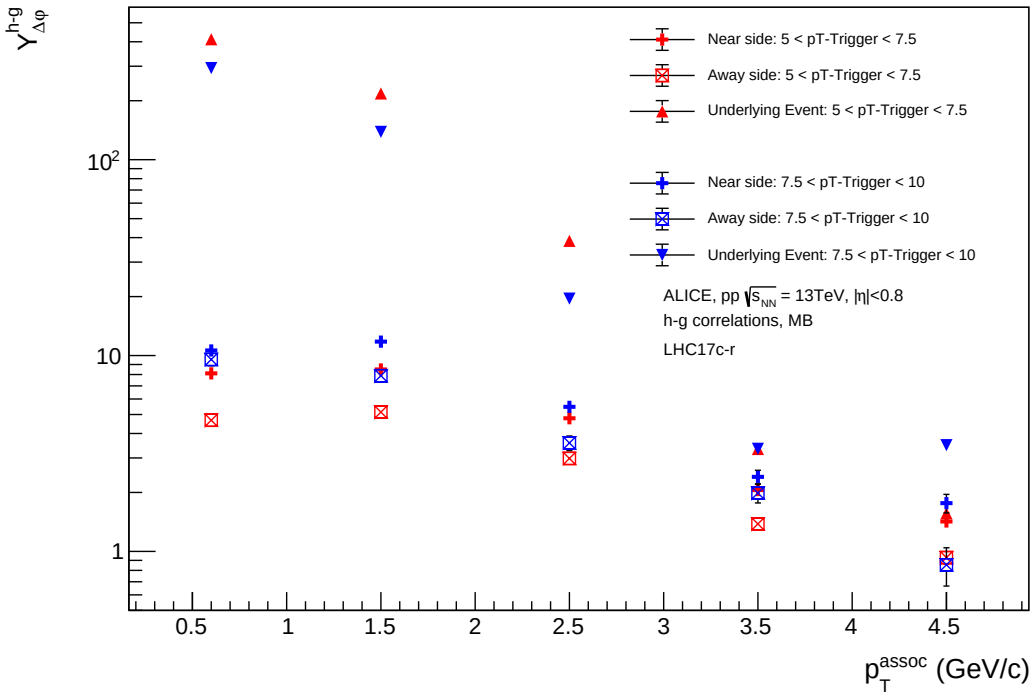

Figure 5.13: Yield for hadron-gamma as a function of $p_{\mathrm{T}}^{\mathrm{assoc}}$ and $p_{\mathrm{T}}^{\mathrm{trigg}}$.

5.5 Particle Origins of Hadrons and Photons

In the following section, Monte Carlo simulations are used to analyze the origins of hadrons and photons. The Monte Carlo data are configured to match the detector's properties (thus anchored) to the real datasets, which are used in this analysis. The MC truth, which represents ideal detection conditions, is utilized to trace the mother particles of the detected particles. For each detected particle, the PDG code of its mother tracks is examined, and if the desired mother is identified, the transversal momentum p_{T} of the daughter track is stored.

5.5.1 Origins of Hadrons

First, the mother PDG codes of all charged particles are analyzed. The results are shown in Figure 5.14. In this context, quarks can originate from fragmentation or directly from the initial collision. It should be noted that the figure shows the origins of charged particles rather than hadrons, as leptons and bosons are not filtered out as daughter tracks. However, only π^0 decays exclusively into non-hadrons, and the contribution of J/ψ decays into leptons is extremely low.

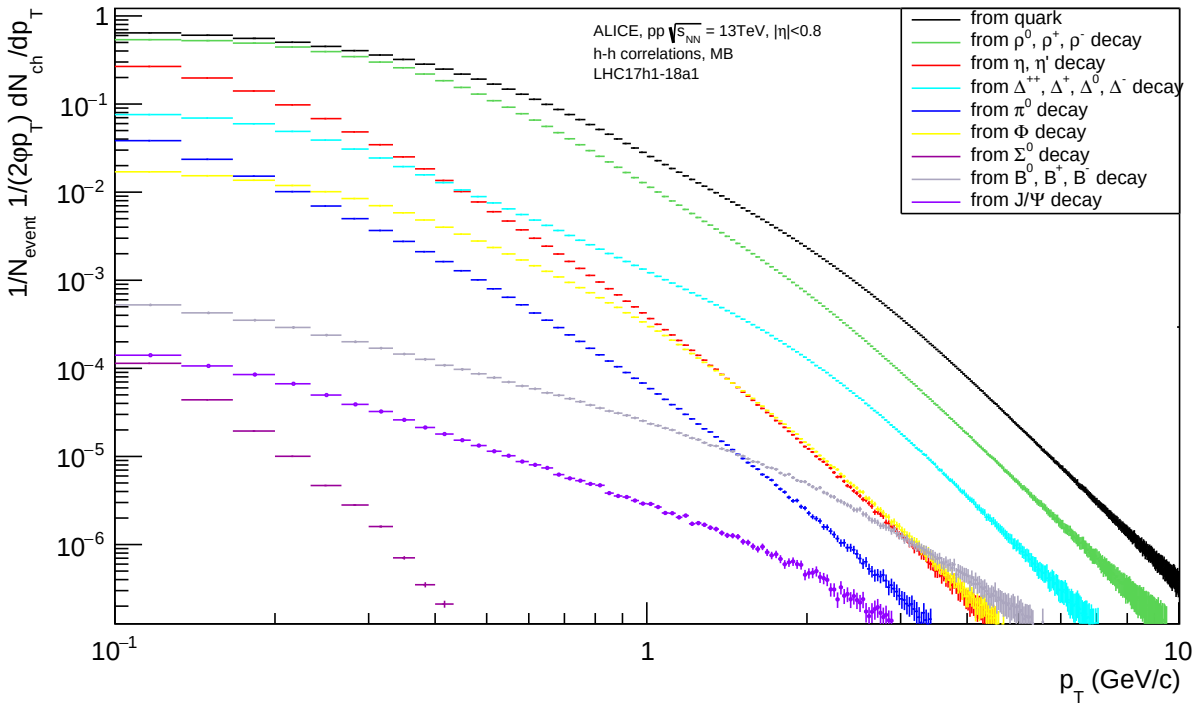

Figure 5.14: Origins of charged particles.

The analysis reveals that the majority of the charged particles originate from fragmentation and the initial collision, with significant contributions from ρ. Additionally, η and Δ also

play a considerable role in the production of charged particles. The large number of particles originating from fragmentation can be explained by the high collision energy of 13 TeV in this proton-proton collision, which provides significant potential for the creation of new particles. The observed ρ and η decay into pions, which are among the lightest hadrons. The Δ decays into protons (or neutrons) and pions. Although pions themselves can decay into leptons and photons, no additional hadrons are produced from them.

5.5.2 Origins of Photons

Monte Carlo truth data For the photons, the results are presented in Figure 5.15. The primary sources of the observed photons are π^0 and η. Other particle decays are less significant. The number of photons originating directly from quarks is extremely low. The photons, which originate from photons, could be explained by the way how Pythia8 handles particle collisions, as mentioned earlier. They can be counted as photons that changed their momentum due to scattering. Also, if their decay chain is traced further, it becomes evident that all of these photons originate from quarks or gluons.

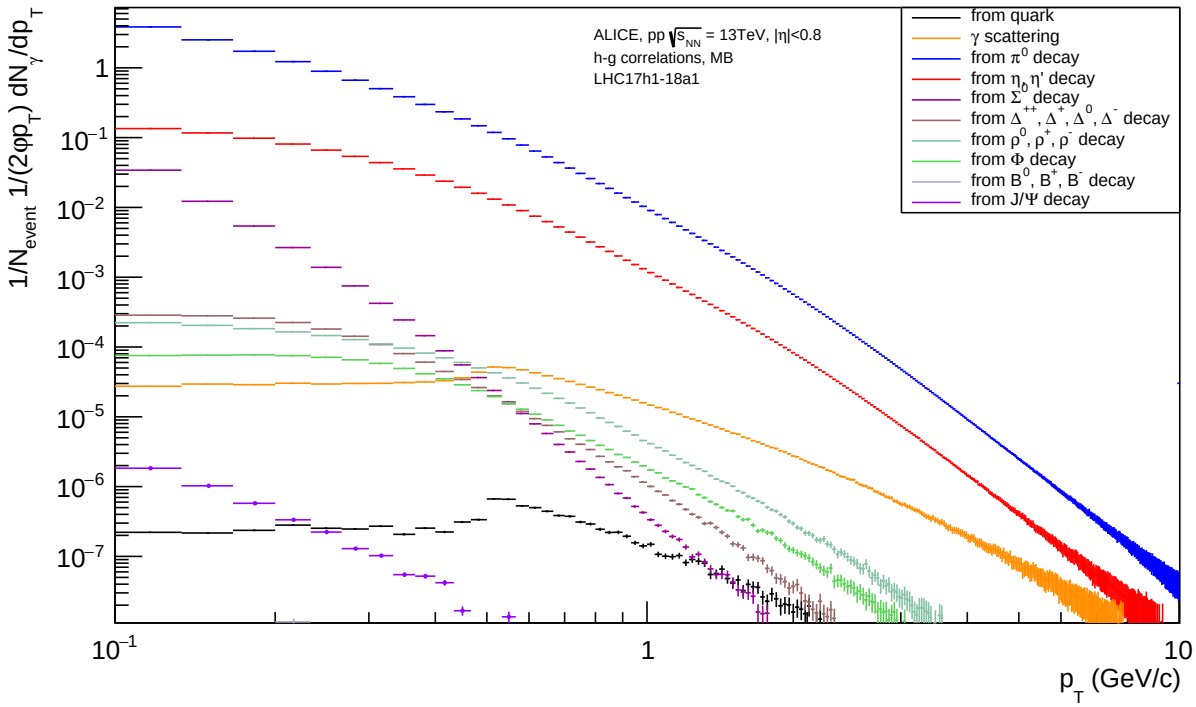

Figure 5.15: Origins of photons.

Due to the very low multiplicity of direct photons from quarks, a different dataset is taken, shown in Figure 5.16. This has a specific **PCMgoodkINT7** setting, which drastically increases the number of direct photons. However, it is to note that this dataset corresponds to a 8 TeV pp collision from 2015 (see Section 4.1.2), which differs from the other datasets used in this analysis.

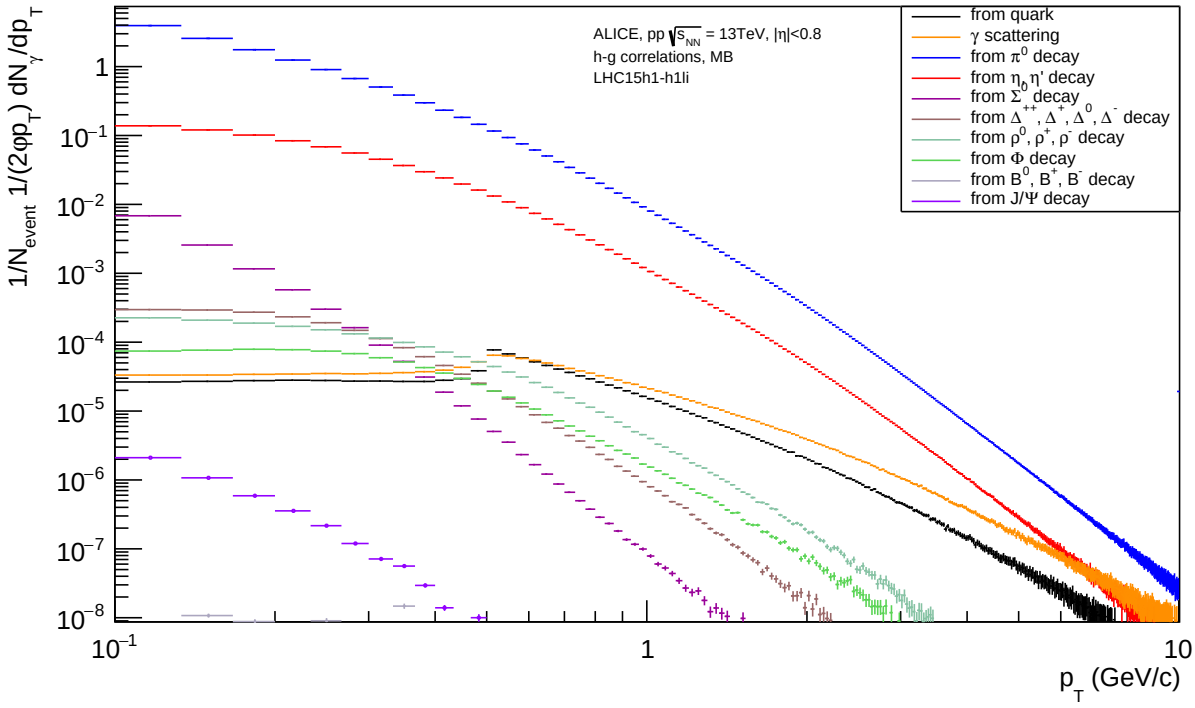

Figure 5.16: Origins of photons with an improved Photon Conversion Method (PCM).

With this dataset in Figure 5.16, the amount of photons originating from the initial collision is drastically increased, labeled as originating from quarks. The shape of the quark curve peaks closely at 0.51 GeV/c compared to the photon curve at 0.55 GeV/c, which is expected because the latter originated also from quarks. The height of these two peaks only differs around 13 %. But for large transverse momenta the discrepancy between these two curves increases noticeably, with more photons, having photons labeled as origin.

Monte Carlo reconstructed data Besides the truth data previously, reconstructed tracks are also analyzed. With this, the origins of photons are also examined, as shown in Figure 5.17. Here, the anchored dataset from 2017 is used.

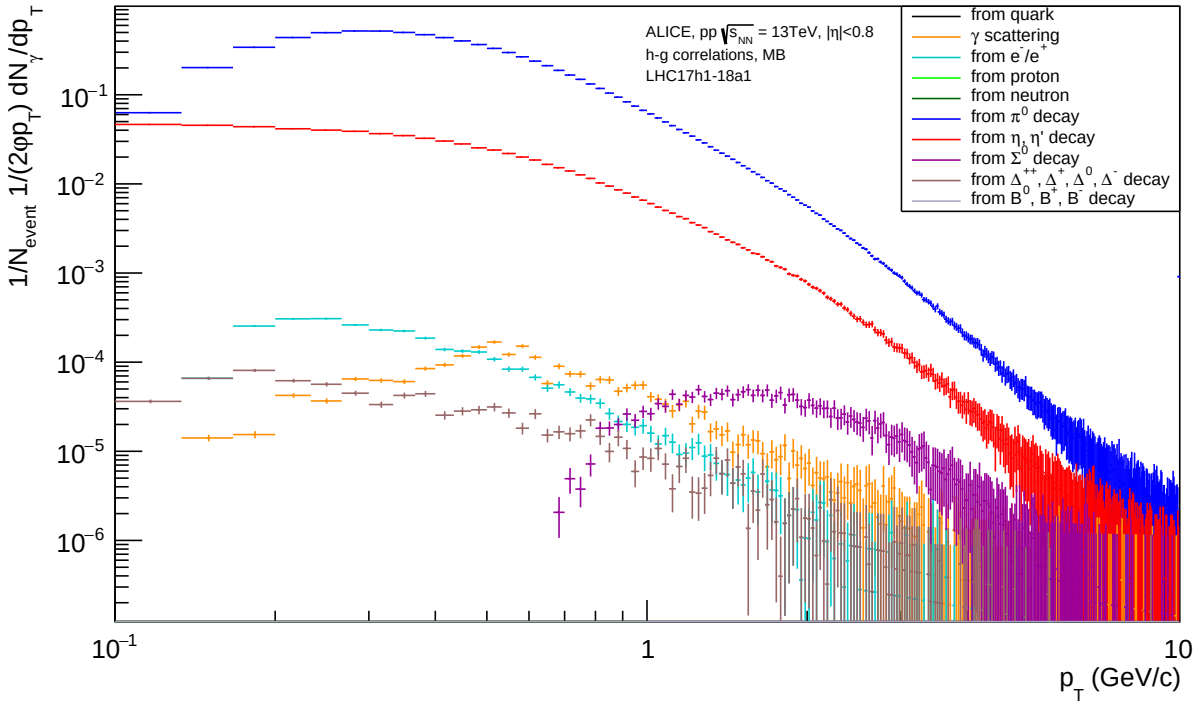

Figure 5.17: Origins of photons from the reconstructed tracks.

The decay of π^0 and η are again the biggest contributions to the photons. The other studied sources contribute less. e^-, e^+, photons and Σ^0 peak all at similar multiplicity heights, but at different transverse momenta. e^- and e^+ peak at around 0.3 GeV/c, while the photons peak at around 0.6 GeV/c. Σ^0 peak lasts at around 1.5 GeV/c. In contrast to the other particles, which have a steep increase in multiplicity up to their peak, the Σ^0 has a rather gradual increase. Compared to the data from the MC truth data, it is notable that the number of produced particles is significantly lower at transverse momentum below 1 GeV/c, particularly for the Σ^0 and, to a lesser extent, for the π^0.“

The protons are an interesting case. They are found at very low p_T and due to their extremely low multiplicity, it is unlikely that they are the mother particles of direct photons, and simulated proton decays are also not expected. It is highly likely that this can be traced back, to how Pythia8 handles particle decays, similar to the case where photons were labeled as mother particles. Due to their low statistics, an analysis would have a low value.

And again, due to the low number of photons, the **PCMgoodkINT7** dataset is taken, as seen in Figure 5.18.

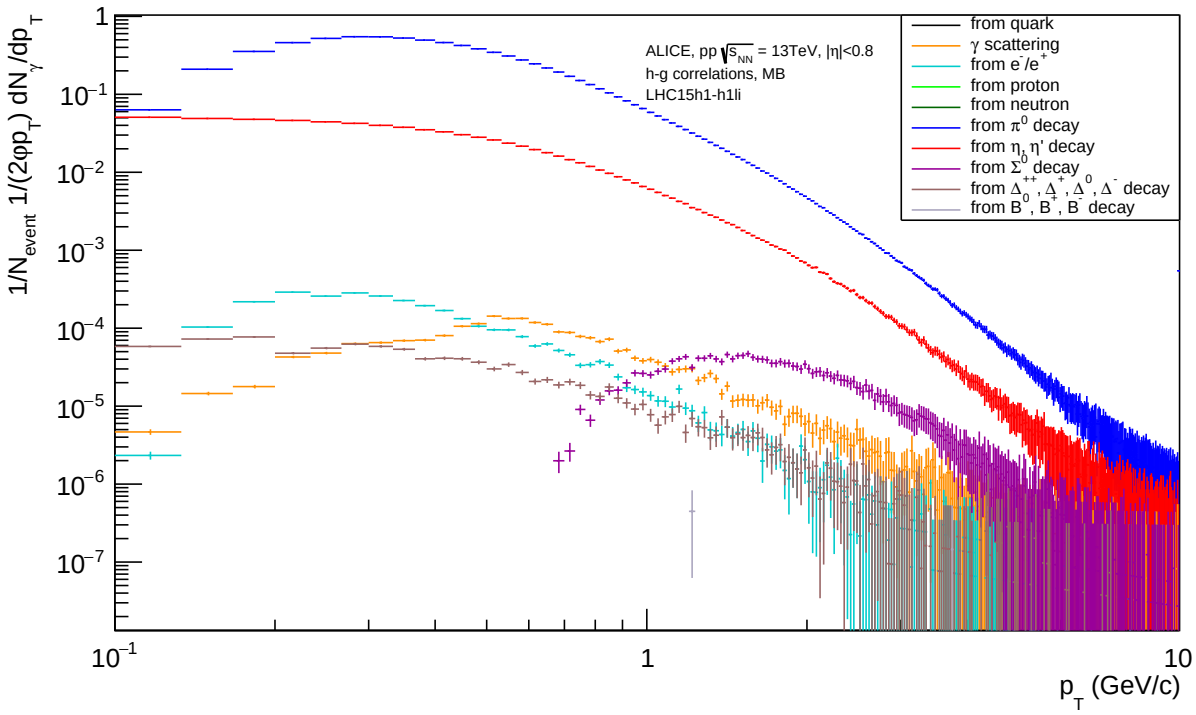

Figure 5.18: Origins of photons from the reconstructed tracks from the **PCMgoodkINT7** dataset.

Like above, π^0 provides the largest amount of photons, followed by η. The e^-, e^+, photons and Σ^0 also look similar. And while not visible in the figure, not only did the number of protons increase, but additionally, photons from neutrons could be found. Due to the low statistics, a further study would be inconclusive. Apart from these observations, no real differences can be noticed between the two datasets.

6 Summary

In this thesis, proton-proton collisions with a center-of-mass energy of $\sqrt{s} = 13\,\text{TeV}$ from the ALICE detector at CERN were analyzed to study di-hadron and hadron-gamma correlations. The focus was on correlation functions, extracting per-trigger yields and determining the origins of the particles.

To obtain reliable data, several selection criteria and cuts were applied to the raw data from Run 2 of the ALICE detector. A minimum bias filter was applied to ensure a comprehensive data selection. The tracks were reconstructed with tight cuts to ensure track quality and clear differentiation between secondary and primary vertices. This distinction was important for reliable correlation functions, to ensure that the correlated particles were indeed from the same vertex. The same applied to photons, which were required to originate from the primary vertex. Additional cuts were implemented to subtract unwanted particles and minimize the influence of secondary vertices, particularly for the V0 selection.

The Photon Conversion Method was used to reconstruct photons by detecting electron-positron pairs with the TPC and ITS detectors of ALICE. This method offered high momentum resolution, especially at low energies, and provided high positional accuracy.

Furthermore, single-particle efficiency corrections were made to account for particles that could not be detected. For that, Monte Carlo simulations using Pythia8 and GEANT3 were made, leading to an efficiency for charged hadrons of around 80–85% and for photons of around 8.6 %. At low p_T the efficiency was reduced due to the large curvature of low-momentum particles.

Correlation functions were created using trigger particles with $5 < p_\text{T}^\text{trigg} < 10\,\text{GeV/c}$ and associated particles with $0.2 \leq p_\text{T}^\text{assoc} \leq 5\,\text{GeV/c}$ for both hadron-hadron and hadron-gamma analyzes. Di-hadron correlation functions were used to analyze jets indirectly and were useful in pp collisions. Several observations were made from the correlations. At higher transverse momenta, the peaks became narrower and more collimated, which can be attributed to two factors: The Lorentz boost of the particles and the decrease in the strong couple constant α_s, resulting in less wide-angle gluon radiation and reduced particle splitting. In hadron-gamma correlations, the peaks were even narrower. Lastly, the Monte Carlo simulations showed correlation functions for different parents of the photons, except for the case where the photons were the parents. There were no correlations expected for secondary photons, which can explain this absence. However, low statistics were a limiting factor.

To quantify the observations, the near-side and away-side peaks of the correlation functions were analyzed with Gaussian fits, and per-trigger yields were extracted. The full width at half maximum (FWHM) of the hadron-hadron peaks decreased with increasing p_T, until approximately $3\,\text{GeV/c}$, where they stabilize. For hadron-gamma correlations, taking into

account the larger error bars, a similar pattern was observed, with a dip at 1.5 GeV/c at the away-side peak. The per-trigger yields for hadron-hadron correlations decreased as the associated particle p_{T} increased. The near-side yields were consistently larger than those from the away-side peak. Additionally, the underlying events, which had already been subtracted from the yields, were also considered. They decreased disproportionately across all p_{T} ranges, emphasizing that proportionally more high-p_{T} particles were produced. In hadron-gamma correlations, the yields increased up to an associated p_{T} of 1.5 GeV/c before decreasing. This indicates that at this transverse momentum of the associated particle, the most particles were created. The underlying events decreased even more disproportionately in this case.

Monte Carlo truth simulations were used to study the origins of the particles. The hadrons in hadron-hadron collisions mainly originated from fragmentation and the direct collision, while the decays of ρ, η and δ also contributed significantly. In the hadron-gamma case, a specific dataset with PCMgoodkINT7 enabled the study of direct photos, which peaked at a p_{T} of around 600 MeV. However, most photons still came from the decay of π^0 and η mesons. The origins of photons in the Monte Carlo reconstructed simulations were similar to the Monte Carlo truth, except for the direct photons, which did not appear in the reconstructed data. This indicates that the reconstruction efficiency of the photons was independent of their origin. An interesting observation of photons originating from photons was made, but this may result from how Pythia8 calculates particle scattering.

Overall, this thesis analyzed hadron-hadron and hadron-gamma correlations in proton-proton collisions. This provided a reference for the correlations of heavy-ion collisions, which are the primary tool to study the strong interaction and the quark-gluon plasma.
A future analysis with data from Run 3 could be made, if the data allows for good PCM.

A Appendix

A.1 Additional one dimensional correlation plots

The analysis shows the pseudorapidity and azimuthal angle differences, $\Delta\eta$ and $\Delta\varphi$, for hadron-hadron and hadron-gamma correlations. For that, the event mixing method was applied. The differences between the mixing functions and the uncorrected functions are presented here.

Hadron-hadron same event $\Delta\eta$ and $\Delta\varphi$ The differences in the uncorrected hadron-hadron correlation are seen in Figure A.5 and A.6.

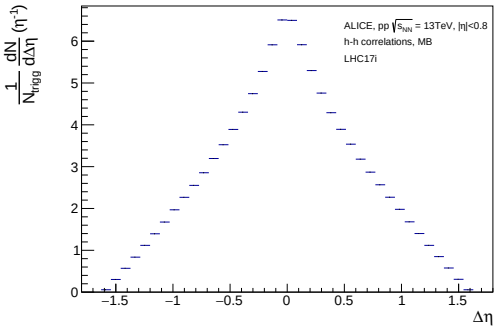

Figure A.1: Difference between the pseudorapidities $\Delta\eta$ of the trigger and the associated particles in hadron-hadron correlations in the same events.

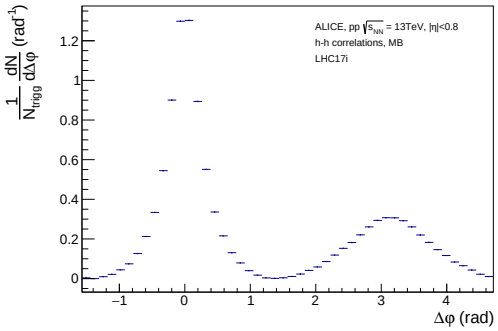

Figure A.2: Difference between the azimuthal angle $\Delta\varphi$ of the trigger and the associated particles in the same hadron-hadron events.

Hadron-hadron mixing function $\Delta\eta$ and $\Delta\varphi$ The two Figures A.3 and A.4 show the differences of the pseudorapidity and azimuthal angle difference of the mixing function that is used to correct the correlation function of the hadron-hadron event.

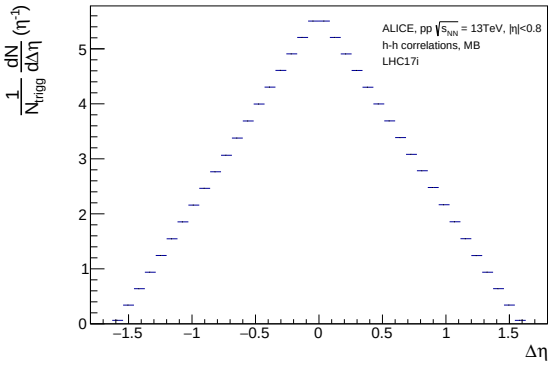

Figure A.3: Difference between the pseudorapidities $\Delta\eta$ of the trigger and the associated particles in hadron-hadron mixing.

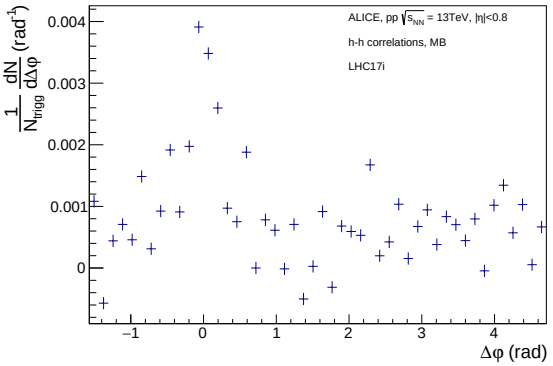

Figure A.4: Difference between the azimuthal angle $\Delta\varphi$ of the trigger and the associated particles in hadron-hadron mixing. A small correlation is visible but irrelevantly small.

Hadron-gamma same event $\Delta\eta$ and $\Delta\varphi$ The differences of the uncorrected hadron-gamma correlation are seen in Figure A.5 and A.6.

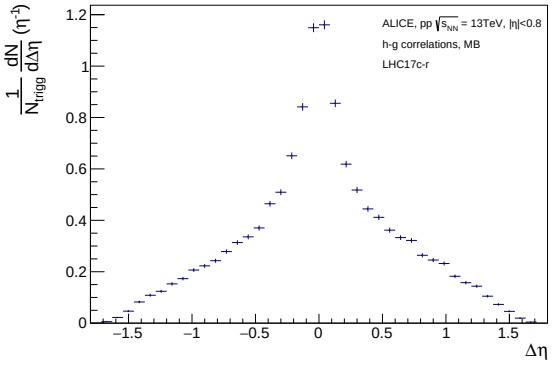

Figure A.5: Difference between the pseudorapidities $\Delta\eta$ of the trigger and the associated particles in hadron-gamma correlations in the same events.

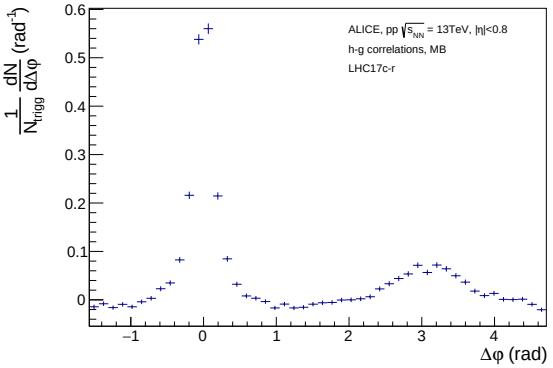

Figure A.6: Difference between the azimuthal angle $\Delta\varphi$ of the trigger and the associated particles in the same hadron-gamma events.

Hadron-gamma mixing function $\Delta\eta$ and $\Delta\varphi$ The differences of the hadron-gamma mixing function can be seen in A.7 and A.8.

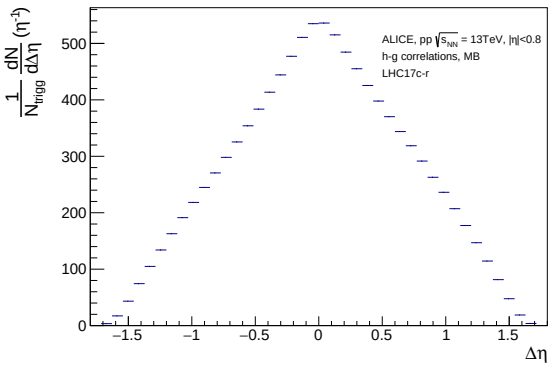

Figure A.7: Difference between the pseudorapidities $\Delta\eta$ of the trigger and the associated particles in hadron-gamma mixing.

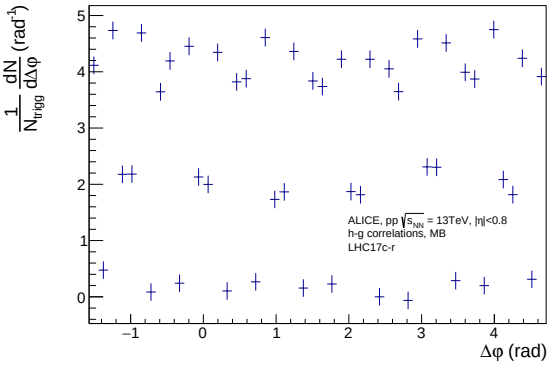

Figure A.8: Difference between the azimuthal angle $\Delta\varphi$ of the trigger and the associated particles in hadron-gamma mixing. No correlation is visible, as expected.

In Figure A.8 a pattern for the mixing event is visible.

List of Figures

List of Tables

Bibliography

[1] Cush. *Standard Model of Elementary Particles*. https://en.wikipedia.org/wiki/File:Standard_Model_of_Elementary_Particles.svg. 2019.

[2] Griffiths and David. *Introduction to Elementary Paricles*. 2nd edition. Wiley-VCH Verlag GmbH & Co. KGaA, 2008.

[3] A. John-Herpin. *Feynman diagrams for the fundamental couplings of the strong interaction*. https://en.m.wikipedia.org/wiki/File:Gluon_coupling.svg. Mar. 2014.

[4] Guenakh Mitselmakher. *Notes Particle Physics 2*. http://www.phys.ufl.edu/~mitselmakher/teaching/ParticlePhysics2/Note_10_Ch7-2.pdf. 2020.

[5] M. Tanabashi et al. (Particle Data Group). 'REVIEW OF PARTICLE PHYSICS'. In: *Phys. Rev. D.* 98 (Aug. 2018), p. 030001. DOI: 10.1103/PhysRevD.98.030001.

[6] Kenneth G. Wilson. 'Confinement of quarks'. In: *Phys. Rev. D.* 10 (8 Oct. 1974), pp. 2445–2459. DOI: 10.1103/PhysRevD.10.2445. URL: https://link.aps.org/doi/10.1103/PhysRevD.10.2445.

[7] Nora Brambilla and Antonio Vairo. *Quark Confinement and the Hadron Spectrum*. 1999. arXiv: hep-ph/9904330 [hep-ph]. URL: https://arxiv.org/abs/hep-ph/9904330.

[8] FAPESP. *New model deepens understanding of the dynamics of quark-gluon plasmas*. https://phys.org/news/2017-06-deepens-dynamics-quark-gluon-plasmas.html. 2017.

[9] C. Klein-Bösing. *Study of the Quark-Gluon Plasma with Hard and Electromagnetic Probes*. Habilitation, University of Muenster. 2013.

[10] Anton Andronic et al. 'Decoding the phase structure of QCD via particle production at high energy'. In: *Nature* 561.7723 (Sept. 2018), pp. 321–330. ISSN: 1476-4687. DOI: 10.1038/s41586-018-0491-6. URL: http://dx.doi.org/10.1038/s41586-018-0491-6.

[11] D Rischke. 'The quark–gluon plasma in equilibrium'. In: *Progress in Particle and Nuclear Physics* 52.1 (Mar. 2004), pp. 197–296. ISSN: 0146-6410. DOI: 10.1016/j.ppnp.2003.09.002. URL: http://dx.doi.org/10.1016/j.ppnp.2003.09.002.

[12] ALICE Collaboration. 'Transverse momentum spectra and nuclear modification factors of charged particles in pp, p-Pb and Pb-Pb collisions at the LHC'. In: *Journal of High Energy Physics* 2018.11 (Nov. 2018). ISSN: 1029-8479. DOI: 10.1007/jhep11(2018)013. URL: http://dx.doi.org/10.1007/JHEP11(2018)013.

[13] Sukanya Mitra et al. *Characterizing quark gluon plasma by thermal photons and lepton pairs*. 2013. arXiv: 1303.0675 [nucl-th]. URL: https://arxiv.org/abs/1303.0675.

[14] ALICE Collaboration. 'Direct photon production in Pb–Pb collisions at $\sqrt{s_{NN}} = 2.76$'. In: *Physics Letters B* 754 (Mar. 2016), pp. 235–248. ISSN: 0370-2693. DOI: 10.1016/j.physletb.2016.01.020. URL: http://dx.doi.org/10.1016/j.physletb.2016.01.020.

[15] C. Klein-Bösing. 'Production of Neutral Pions and Direct Photons in Ultra-Relativistic Au + Au Collisions'. PhD thesis. University of Muenster, 2004.

[16] B. Povh et al. *Teile und Kerne*. Sixth Edition. Springer-Verlag GmbH, 2004.

[17] B. Sahoo. 'Measurment of $R_2(\Delta\eta, \Delta\varphi)$ and $P_2(\Delta\eta, \Delta\varphi)$ correlation functions in pp collisions at $\sqrt{s} = 13$ TeV with ALICE at the LHC'. PhD thesis. Indian Institute of Technology Bombay, Aug. 2022.

[18] JabberWok. *A graphic showing the relationship between angle and pseudorapidity*. https://commons.wikimedia.org/wiki/File:Pseudorapidity2.png. May 2007.

[19] E. Mobs. *The CERN accelerator complex in 2019 Complexe des accélérateurs du CERN en 2019*. https://cds.cern.ch/record/2684277?ln=de. 2019.

[20] CERN. *LHC Season 2 facts & figures*. https://home.cern/sites/default/files/2018-07/factsandfigures-en_0.pdf. 2018.

[21] L. Evans and Philip Bryant. 'LHC Machine'. In: *Journal of Instrumentation* 3 (Aug. 2008), S08001. DOI: 10.1088/1748-0221/3/08/S08001.

[22] M. Benedikt et al. *LHC Design Report*. https://cds.cern.ch/record/823808. 2004.

[23] ATLAS Collaboration). 'The ATLAS Experiment at the CERN Large Hadron Collider'. In: *JINST* (2018), S08003. DOI: 10.1088/1748-0221/3/08/S08003.

[24] CMS Collaboration). 'The CMS experiment at the CERN LHC. The Compact Muon Solenoid experiment'. In: *JINST* (2018), S08004. DOI: 10.1088/1748-0221/3/08/S08004.

[25] LHCb Collaboration). 'The LHCb Detector at the LHC'. In: *JINST* (2018), S08005. DOI: 10.1088/1748-0221/3/08/S08005.

[26] Elena Botta. 'Particle identification performance at ALICE'. In: *International Journal of Modern Physics A* (2017). arXiv: 1709.00288 [nucl-ex]. URL: https://cds.cern.ch/record/2282027.

[27] The ALICE Collaboration et al. 'The ALICE experiment at the CERN LHC'. In: *Journal of Instrumentation* 3 (Aug. 2008), S08002. DOI: 10.1088/1748-0221/3/08/S08002.

[28] The ALICE Collaboration et al. 'Performance of the ALICE VZERO system'. In: *Journal of Instrumentation* 8 (2013), P10016. DOI: 10.1088/1748-0221/8/10/p10016. arXiv: 1306.3130 [nucl-ex].

[29] J. Alme et al. 'The ALICE TPC, a large 3-dimensional tracking device with fast readout for ultra-high multiplicity events'. In: *Nuclear Instruments and Methods in Physics Research Section A: Accelerators, Spectrometers, Detectors and Associated Equipment* 622 (Aug. 2010), pp. 316–367. DOI: 10.1016/j.nima.2010.04.042.

[30] E. Masson (for the ALICE Collaboration). 'Direct Photon Measurements with the ALICE Experiment at the LHC'. In: *Nucl.Instrum.Meth.A622:316-367,2010* (Nov. 2018), p. 4. DOI: 10.48550/arXiv.1811.02220.

[31] ALICE collaboration. *Alice offline - aliroot documentation*. https://alice-offline.web.cern.ch/AliRoot/Manual.html.

[32] ALICE collaboration. *ALICE Analysis Repository*. https://github.com/alisw/AliPhysics.

[33] M. Van Leeuwen. *TrackParametersMCTruth*. https://twiki.cern.ch/twiki/bin/view/ALICE/TrackParametersMCTruth. Accessed: 2024-07. 2017.

[34] ALICE Data Preparation Group. *ALICE data flow, Analysis Tutorial*. https://indico.cern.ch/event/666222/contributions/2768780/attachments/1551303/2437229/DPG_AnalysisTutorial_20171102.pdf. DPG. Nov. 2017.

[35] N. Schmidt. 'Neutral meson and direct photon measurements with conversions in ALICE in proton-proton collisions at $\sqrt{s} = 0.9, 7$ and 8 TeV'. MA thesis. University of Heidelberg, Mar. 2017.

[36] ALICE Collaboration et al. 'ALICE: Physics performance report, volume II'. In: *Journal of Physics G: Nuclear and Particle Physics* 32 (Sept. 2006), pp. 1295–2040. DOI: 10.1088/0954-3899/32/10/001.

[37] J. Podolanski and R. Armenteros. 'III. Analysis of V-events'. In: *The London, Edinburgh, and Dublin Philosophical Magazine and Journal of Science*. 7th ser. 45 (360 Aug. 1954), pp. 13–30. DOI: 10.1080/14786440108520416.

[38] ALICE Collaboration et al. 'Neutral pion production at midrapidity in pp and Pb-Pb collisions at $\sqrt{s_{NN}} = 2.76$ TeV'. In: *The European Physical Journal C*. 74 (Oct. 2014), p. 31. DOI: 10.1140/epjc/s10052-014-3108-8. arXiv: 1405.3794 [nucl-ex].

[39] N. Schmidt et al. 'Analysis Note: Direct photon measurement with ALICE in pp collision at $\sqrt{s_{NN}} = 8$ TeV using the PCM, EMC and PCM-EMC reconstruction techniques'. In: Nov. 2018, p. 55.

[40] F. Bock et al. 'Analysis Note: Measurement of Direct Photons in p–Pb Collision at $\sqrt{s_{NN}} = 5.02$ TeV using the PCM, EMC and PCM-EMC Reconstruction Techniques'. In: Sept. 2018, p. 125.

[41] T. Dahms. 'Measurement of photons via conversion pair with the PHENIX experiment at RHIC'. MA thesis. Stony Brook University, May 2005.

[42] Prof. Dr. K. Reygers. *Quark-Gluon Plasma Physics 2. Kinematic Variables*. https://www.physi.uni-heidelberg.de/~reygers/lectures/2017/qgp/qgp_ss17_02_kinematics.pdf. 2017.

Declaration of Academic Integrity

I, *Alexander Terbeck*, hereby confirm that i have written this thesis, entitled "Analysis of Hadron-Photon and Di-Hadron Correlations in pp Collisions at $\sqrt{s} = 13\,\text{TeV}$ with ALICE" independently and have not used any sources or aids other than those stated. I have substantiated or identified anything taken over in terms of ideas, content or wording by stating the origin and text or annotation. This also applies to images, tables, drawings, sketches and electronic media that were not created by me.

I am aware that plagiarism is considered an act of deception which can result in sanction in accordance with the examination regulations.

I consent to having my thesis cross-checked with other texts to identify possible similarities and to having it stored in a database for this propose.

I confirm that I have not submitted the following thesis in part or whole as an examination paper before.

Münster, 10th of October 2024

Alexander Terbeck

Acknowledgement

First and foremost, I would like to express my thanks to Prof. Dr. Christian Klein-Bösing for providing me the opportunity to write this thesis, his support and the numerous discussions we had. I also wish to thank Prof. Dr. Anton Andronic for agreeing to review this thesis.
Special thanks go to Dr. Lucia Anna Tarasovičová and Peter Stratman for their supervision, helpful advice, and valuable discussions and explanations throughout the progress of my thesis.
I would also like to thank my office colleagues for the useful discussions, conversations and pleasant atmosphere. Additionally, I am grateful to all the members of the working group for their advice and supportive attitude.
Last but not least, I am deeply thankful to my family and friends for their constant support during the time I worked on this thesis.